Single-molecule sensing with nanopores and nanoslits

Yang, W.W.W.

Important note
To cite this publication, please use the final published version (if applicable).
Please check the document version above.

SINGLE-MOLECULE SENSING WITH NANOPORES AND NANOSLITS

Single-Molecule Sensing with Nanopores and Nanoslits

Dissertation

for the purpose of obtaining the degree of doctor
at Delft University of Technology
by the authority of the Rector Magnificus Prof.dr.ir. T.H.J.J van der Hagen,
chair of the Board for Doctorates to be defended publicly on
Wednesday 3rd Feb 2021 at 10:00 o'clock

by

Wayne Wen Wei YANG

Master of Science, Physics
McGill University, Montreal, Canada,
born in Singapore.

This dissertation has been approved by the promotor:

promotor: Prof. dr. C. Dekker

Composition of the doctoral committee:

Rector Magnificus,	chairperson
Prof. dr. C. Dekker,	Delft University of Technology

Independent members:

Prof. dr. A. Radenovic,	École polytechnique fédérale de Lausanne
Dr. S. Garaj,	National University of Singapore
Dr. C. Joo,	Delft University of Technology
Dr. S. Caneva,	Delft University of Technology
Prof. dr. P.G. Steeneken,	Delft University of Technology
Prof. dr. M. Dogterom,	Delft University of Technology, reserve member

Other members:

Prof. dr. B. Radha,	University of Manchester

To my dear Ma and Pa,
for all the love and sacrifices,
this thesis is dedicated to you.

CONTENTS

1

GENERAL INTRODUCTION

Here, I motivate the importance of single molecule sensing with nanopores and nanoapertures. Though DNA sequencing has been successfully realised using biological nanopores, solid state nanopores remain highly useful for a wide variety of application. Furthermore, the chapters in the thesis are outlined.

1

1.1. INTRODUCTION - THE POLYMERS OF LIFE

Already more than a millennia ago, it was apparent to the ancients that hereditary information is passed down through the generations as one observes a certain likeness between related members of a family [1, 2]. Various philosophers such as Hippocrates and Aristotle speculated about the possible manner through which this information was transmitted [3]. Notably, Aristotle proposed that this information was physically transmitted through the mixing of sperm and blood, a marked shift from the non-physical mechanisms proposed by the philosophers before him. Over the years, different candidates were proposed to be the carrier for hereditary information [4]. As recent as the 1940s, many scientists thought that proteins were the main carrier of this information, as its abundance and importance to many celluar function was thought to explain the wide diversity in life.

This theory was dispelled by the Hershey-Chase experiment where the backbone of DNA and the protein coating of bacteriophages were labelled with different isotopes (phosphorous P-32 in the case for DNA and sulphur S-35 for the protein)[5]. These labelled bacteriophages (bacteria viruses) were used to infect healthy cells. Hershey and Chase reasoned that the medium carrying the genetic information would be found within the cells when the cells were lysed, whereas nongenetic material would remain outside the cell, since the bacteriophages had to introduce genetic information for its replication within the cell. After infection and cell lysis process, a high concentration of P-32 was found in the cells but almost no presence of S-35 (See Fig. 1.1)[6]. This results strongly suggested that it was DNA that entered the cell and hence carried the genetic information (Fig 1.1). Exactly how the genetic information was encoded physically was not known. It was until the work of James Watson, Francis Crick and Rosalind Franklin that the structure of DNA was elucidated through x-ray crystallography [7–9]. From the structure, they were able to hypothesize the physical manner that genetic information was actually encoded in the molecule (Fig 1.2a).

1.2. DNA, RNA AND PROTEINS

Genetic information is stored in a long polymer chain made from 4 different nucleotides, or 'DNA bases'. Figure 1.2b shows a schematic representation of DNA [10, 11]. Each base consists of 4 nucleobases (adenine (A), thymine (T), cytosine (C) and guanine (G)) that are linked to a sugar (deoxyribose) and a phosphate group. Each base is linked, via a covalent bond between the sugar and phosphate groups, to neighboring bases which leads to a long sugar-phosphate backbone forming a strand of DNA. The single DNA strand can be linked to another strand of DNA, through hydrogen bonds, to the respective complimentary bases - A to T and C to G. It is the order of the bases in this chain that constitutes the DNA sequence which codes the genetic information that determine everything from eye colour to susceptibility to certain diseases [12–14].
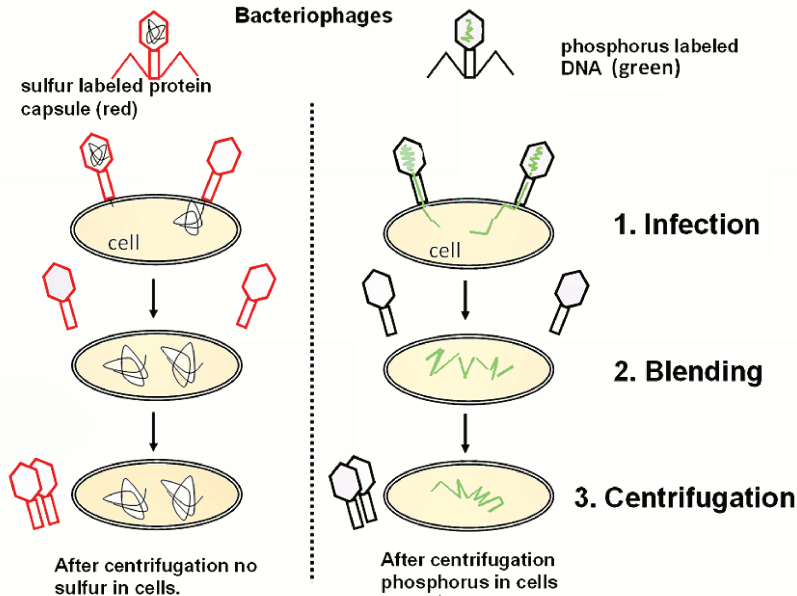
Figure 1.1: **Schematic of Hershey-Chase experiment** DNA and protein of bacteriophages were labelled with sulfur and phosphorous isotopes. Cells were infected and collected after a blending and centrifugation step that removed materials that were outside of the cells. The cells were subsequently lysed and checked for the presence of either sulfur or phosphorus in the cell. Only phosphorus remained, indicating that DNA was the material that was injected into the cell and carried the genetic information that was used for the expression of bacteriophages. Reproduced from Ref [15].
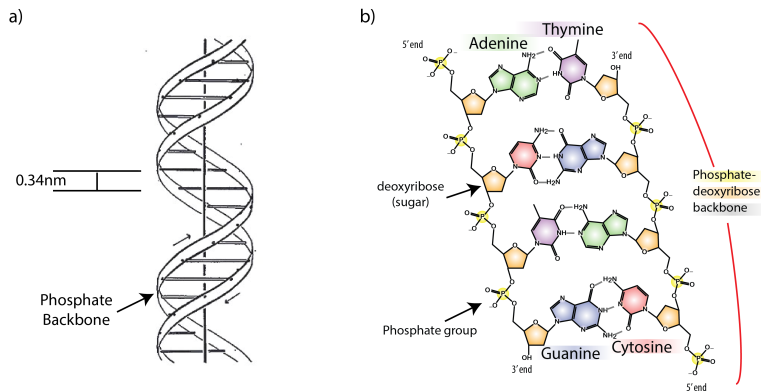
Figure 1.2: **Schematic of DNA structure**. a) DNA structure as reported by Watson and Crick in their 1953 paper. DNA is a right-handed double helix with a phosphate backbone. The bases of the DNA are separated by 0.34nm. Reproduced from Ref.[7]. b) Chemical make-up of DNA. DNA consist of 4 different nucleobases adenine (A), thymine (T), cytosine (C) and guanine (G) that are linked to a sugar (deoxyribose) and a phosphate group. Reproduced from Ref[16].

1
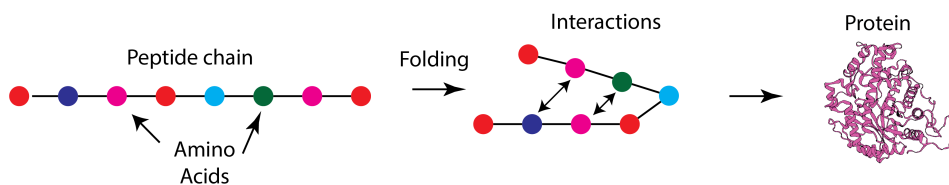
Figure 1.3: **Schematic of amino acids forming proteins.** There are over 20 amino acids. They can be arranged in different sequences to form a linear peptide chain and here are represented as coloured spheres. Amino acids have different interactions with others, which leads to a variety of structures and properties when folded. The different combinations and structures of the peptide chains give rise to many different proteins with different physical shapes and function. Protein rendered from "The Protein Imager", Ref [20].

Particular segments of DNA sequences, known as genes, code for RNA (through a process called 'transcription'), and these RNA molecules can subsequently be translated into proteins within the cell [17]. There are 20 different amino acids that are encoded by the DNA/RNA. Moving up the heirarchy, these amino acids can link to form a chain. A polymer chain of amino acids in a specific sequence forms a polypeptide chain which typically folds into a particular shape to form a protein (Illustrated in Fig 1.3). Proteins are the workhorses of the cell through which functions are accomplished [18]. Proper folding and maintenance of protein shape is paramount to proper functioning of the cell. Misfolded proteins can lose their function and are at the heart of many diseases [19].

Given this importance of the sequentially stored information in DNA and proteins, there has been a longstanding drive for quick and cheap sequencing methods to readout this information for diagnostics applications[21]. New and subsequent generations of sequencing technologies have drastically brought down the speed and cost of sequencing. One can now sequence the entire human genome for less than $1000 [22, 23]. Remarkably, it cost less to sequence your genome than to take a chest X-ray or MRI scan! The newest sequencing technologies, known as next-gen sequencing, which are largely based around nanopores, are expected to bring this cost down further, and to make sequencing more routine beyond the traditional healthcare setting [24–26].

1.3. READING THE CODE OF LIFE - NANOPORES

Nanopores operate on a simple principle of sensing, through sensing of the ionic conductance. We describe the procedure briefly as more details of this sensing principle can be found in **Chapter 2** of this thesis. Two different aqueous reservoirs are separated by a thin membrane [27, 28]. A tiny hole is etched in the membrane and an ionic current can be measured by applying a voltage difference between the two reservoirs to drive ions in the solution through this hole and by monitoring the resulting current. An analyte of interest (such as a DNA sample) is introduced in one reservoir and the passage of the analyte through this tiny hole can then be detected from the disruption of the ionic current [29, 30]. There are two main categories of nanopores, biological nanopores which insert pore-forming proteins called porins into a lipid membrane, and solid state nanopores where the pores are produced in a solid-state membrane by nanofabrication techniques [31].
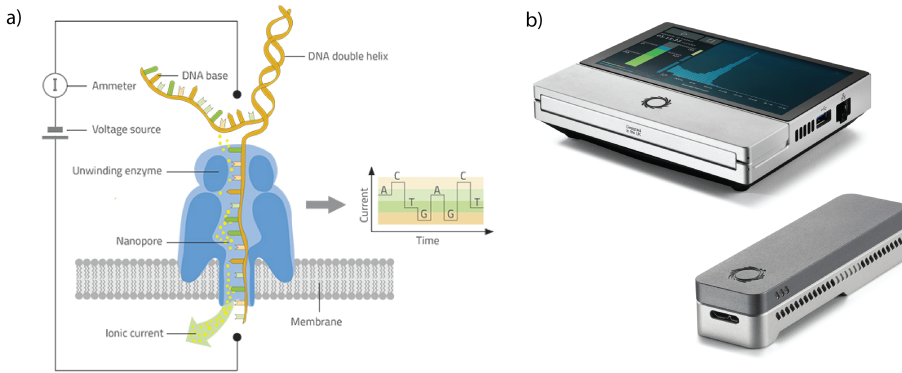
Figure 1.4: **Nanopore sequencing devices** Figures adapted from Ref [39]. a) Schematic of nanopore sequencing device with a biological nanopore. An enzyme is used to unwind and ratched single strand DNA through (ssDNA). The ionic current throught the nanopore is measured. Different DNA bases gives rise to different current blockades and can then be identified. b) Examples of Oxford Nanopore MinION sequencers. The devices are no larger than an external hard drive thus enabling in-field sequencing.

Through this simple sensing principle, the sequencing of DNA has been demonstrated, most notably by the labs of Gundlach and subsequently commercialized by a number of sequencing companies, most notably Oxford Nanopore Technologies [32–34]. At the heart of their technology is the use of biological pores such as (MspA and Csg) that naturally form tiny nanopores of about 1-2 nm in diameter in lipid membranes. It is through this that DNA is ratchet through by a molecular motor and detected. To highlight one such device, the MinION sequencer is a compact device smaller than a typical hard drive and enables in-field sequencing (Fig 1.4) [35, 36]. The portability and robustness of such sequencers were proven when they were launched into the international space station for sequencing experiments in microgravity environments [37, 38].

Given the success of the nanopore-based sequencers, we project that in 5-10 years, nanopores will be ubiquitous, found in every doctor's office and used for everything from clinical diagnostics for personalized medicine to quality control purposes and monitoring in food and crop production [40]. The global sequencing market has been projected to go from 7 billion in 2020 to more than 25 billion in 10 years[41].

1.4. WHY NOT SEQUENCE?

In view of the impressive success of biological nanopore-based and other sequencing technologies, one may wonder if everything useful been done with solid state nanopores? Afterall, sensing at the base pair resolution of DNA (a mere distance of 0.34nm between neighbor base pair) seems to be the ultimate limit in biosensing. As described at the start of the thesis, all genetic information is encoded in DNA, and hence, the key information can in principle be deduced from simply sequencing the DNA. For example, the presence of viral and disease-causing DNA mutations that produce protein misfolding can be directly detected or worked back from the sequencing data. The question "Why not simply sequence instead of developing a DNA sensor?" was a recurrent critique behind

every project proposal during my PhD.

This thesis is a culmination of work that I hope proves that the answer to this question is a resounding **NO**. There is a lot to be done both in terms of developing solid state nanopores as sensors as well as in the application of nanopores to biosensing in order to answer key questions to biology [27]. For example, the prevalence of post-translational modification to proteins after their synthesis indicates the need for direct protein-sensing tools that can probe protein shape and sequence and opens up demands for new sensors – an area where solid-state nanopores may play a future role [42]. New sensors can combine the lessons and principles of nanopore sensing with optical readout methods. Indeed, I am confident that sensing with solid-state nanopores will remain highly relevant for the coming decade.

1.5. OUTLINE OF THIS THESIS

We begin this thesis by giving an overview to single molecule sensing in nanoapertures in **Chapter 2**. We introduce two main ways, ionic conductance sensing as well as optical sensing. We compare the features of both these sensing methods and highlight some of the recent work to integrate both of these approaches for biosensing.

From the technical point of view, solid-state nanopores are still hindered by a lack of a fabrication method that is reliable and compatible with mass production. In **Chapter 3**, we tackle this problem as we show a fabrication method for the production of both nanopore arrays and single nanopores using single-shot electron-beam lithography and an etching step. Our method produces consistent nanopores down to the 15 nm size on both free-standing silicon nitride, and remarkably, also on graphene membranes which are only an atomic layer thick. The nanopores thus created can be used for DNA sensing purposes and perform on par with TEM-milled nanopores.

Solid state pores are typically too large for single-base pair resolution and direct DNA sequencing. However, we demonstrate their application in both applied and fundamental research questions by sensing protein-bound DNA complexes in a novel detection scheme for diagnostics, as well as DNA-structure modulation induced by protein complexes to answer questions on DNA organization. First, in **Chapter 4**, we demonstrate a CRISPR-dCas9 based DNA detection method for fingerprinting of DNA down to the single nucleotide level. The dCas9 proteins remain stably bound in high salt and the location of the targeted sequence can be detected. The binding of the Cas9 protein was sensitive to single mutations in the gRNA, demonstrating basepair accuracy. We anticipate future nanopore-based CRISPR-Cas detection schemes for DNA typing. Second, we explored DNA sequence-directed cooperation of nucleoid-associated proteins in **Chapter 5**. We find that the sequential arrangement of the genes mattered in determining DNA organisation on top of just the presence of the sequence. Two plasmids with the same DNA sequence but arranged in a different order gave a different level of DNA compaction with the same concentrations of nucleoid associated proteins as detected in a nanopore. These two examples illustrate the relevance of solid state nanopores to tackle relevant questions in both applied research and fundamental biology.

In the final two chapters of the thesis, we explored 2 new types of solid state sensors. In **Chapter 6**, we use 2D nanoslits, fabricated from ultra-smooth 2D materials to probe fundamental polymer transport and physics. The height of the slits can be very

precisely (0.3 nm) controlled. We observe DNA sliding through the length of the slit in a near-frictionless manner with weak and transient interactions with the channels. We anticipate a new class of precise amenable sensors to probe polymer transport in confinement and advance the understanding of polymer physics of DNA. Finally, in **Chapter 7**, we develop a direct milling method with focused ion beam (FIB) to fabricate huge arrays of plasmonics gold nanoapertures. We demonstrate that these apertures are able to both optically tweeze and detect nanosized objects such as polystyrene beads and single proteins in a label-free manner. Proteins can be captured and tweezed for minutes. We see hints of protein conformational changes and propose a future set of experiment to observe conformational changes in individual Heat Shock Protein 90 (hsp90) proteins, for which the kinetic can be by modulated with AMP-PNP.

1

REFERENCES

[1] M. Cobb, *Nature Reviews Genetics*, Vol. 7 (Nature Publishing Group, 2006) pp. 953–958.

[2] R. Falk, *Genetic analysis: a history of genetic thinking*, Vol. 47 (American Library Association, 2010) pp. 47–2549–47–2549.

[3] D. Henry, *Aristotle on the Mechanism of Inheritance,* 10.1007/s10739-005-3058-y.

[4] Siddhartha Mukherjee, *The Gene: An Intimate History* (Scribner's, 2016).

[5] A. Hershey and M. Chase, *Independent functions of viral protein and nucleic acid in growth of bacteriophage.* The Journal of general physiology **36**, 39 (1952).

[6] F. Rohwer and A. M. Segall, *In retrospect: A century of phage lessons,* Nature **528**, 46 (2015).

[7] J. D. Watson and F. H. Crick, *Molecular structure of nucleic acids: A structure for deoxyribose nucleic acid,* Nature **171**, 737 (1953).

[8] L. Pauling and R. B. Corey, *Structure of the Nucleic Acids,* Nature **171**, 346 (1953).

[9] A. Klug, *Rosalind Franklin and the discovery of the structure of DNA,* Nature **219**, 808 (1968).

[10] F. Crick, *Central dogma of molecular biology,* Nature **227**, 561 (1970).

[11] S. Minchin and J. Lodge, *Understanding biochemistry: Structure and function of nucleic acids,* (2019).

[12] D. White and M. Rabago-Smith, *Genotype-phenotype associations and human eye color,* Journal of Human Genetics **56**, 5 (2011).

[13] P. Sulem, D. F. Gudbjartsson, S. N. Stacey, A. Helgason, T. Rafnar, K. P. Magnusson, A. Manolescu, A. Karason, A. Palsson, G. Thorleifsson, M. Jakobsdottir, S. Steinberg, S. Pálsson, F. Jonasson, B. Sigurgeirsson, K. Thorisdottir, R. Ragnarsson, K. R. Benediktsdottir, K. K. Aben, L. A. Kiemeney, J. H. Olafsson, J. Gulcher, A. Kong, U. Thorsteinsdottir, and K. Stefansson, *Genetic determinants of hair, eye and skin pigmentation in Europeans,* Nature Genetics **39**, 1443 (2007).

[14] A. V. Hill, *The genomics and genetics of human infectious disease susceptibility,* Annual Review of Genomics and Human Genetics **2**, 373 (2001).

[15] T. Sione, *Hershey Chase Experiment* (Wikimedia Commons, 2010).

[16] M. P. Ball, *Chemical structure of dna,* (2009).

[17] F. H. Crick, *The origin of the genetic code,* Journal of Molecular Biology **38**, 367 (1968).

[18] J. A. Marsh and S. A. Teichmann, *Structure, dynamics, assembly, and evolution of protein complexes,* Annual Review of Biochemistry **84**, 551 (2015).

[19] I. Moreno-Gonzalez and C. Soto, *Misfolded protein aggregates: Mechanisms, structures and potential for disease transmission, Seminars in Cell and Developmental Biology,* **22**, 482 (2011).

[20] G. Tomasello, I. Armenia, and G. Molla, *The Protein Imager: A full-featured online molecular viewer interface with server-side HQ-rendering capabilities,* Bioinformatics **36**, 2909 (2020).

[21] M. L. Metzker, *Sequencing technologies the next generation,* Nature Reviews Genetics **11**, 31 (2010).

[22] E. R. Mardis, *Next-Generation DNA Sequencing Methods,* Annual Review of Genomics and Human Genetics **9**, 387 (2008).

[23] J. A. Schloss, R. A. Gibbs, V. B. Makhijani, and A. Marziali, *Cultivating DNA Sequencing Technology After the Human Genome Project,* Annual review of genomics and human genetics **21**, 117 (2020).

[24] J. A. Shendure, G. J. Porreca, G. M. Church, A. F. Gardner, C. L. Hendrickson, J. Kieleczawa, and B. E. Slatko, *Overview of DNA Sequencing Strategies,* Current Protocols in Molecular Biology **96**, 7.1.1 (2011).

[25] E. R. Mardis, *DNA sequencing technologies: 2006-2016,* Nature Protocols **12**, 213 (2017).

[26] L. Restrepo-Pérez, C. Joo, and C. Dekker, *Paving the way to single-molecule protein sequencing,* Nature Nanotechnology **13**, 786 (2018).

[27] L. Xue, H. Yamazaki, R. Ren, M. Wanunu, A. P. Ivanov, and J. B. Edel, *Solid-state nanopore sensors,* Nature Reviews Materials **5**, 931 (2020).

[28] C. Dekker, *Solid-state nanopores,* Nature Nanotechnology **2**, 209 (2007).

[29] A. Meller, L. Nivon, and D. Branton, *Voltage-driven DNA translocations through a nanopore,* Physical Review Letters **86**, 3435 (2001).

[30] S. Lindsay, *The promises and challenges of solid-state sequencing,* Nature nanotechnology **11**, 109 (2016).

[31] F. Haque, J. Li, H.-C. Wu, X.-J. Liang, and P. Guo, *Solid-state and biological nanopore for real-time sensing of single chemical and sequencing of DNA,* Nano Today **8**, 56 (2013).

[32] M. Jain, S. Koren, K. H. Miga, J. Quick, A. C. Rand, T. A. Sasani, J. R. Tyson, A. D. Beggs, A. T. Dilthey, I. T. Fiddes, S. Malla, H. Marriott, T. Nieto, J. O'Grady, H. E. Olsen, B. S. Pedersen, A. Rhie, H. Richardson, A. R. Quinlan, T. P. Snutch, L. Tee, B. Paten, A. M. Phillippy, J. T. Simpson, N. J. Loman, and M. Loose, *Nanopore sequencing and assembly of a human genome with ultra-long reads,* Nature Biotechnology **36**, 338 (2018).

1

[33] M. Jain, H. E. Olsen, B. Paten, and M. Akeson, *The Oxford Nanopore MinION: delivery of nanopore sequencing to the genomics community,* Genome Biology **17**, 1 (2016).

[34] I. M. Derrington, T. Z. Butler, M. D. Collins, E. Manrao, M. Pavlenok, M. Niederweis, and J. H. Gundlach, *Nanopore DNA sequencing with MspA,* Proceedings of the National Academy of Sciences of the United States of America **107**, 16060 (2010).

[35] S. S. Johnson, E. Zaikova, D. S. Goerlitz, Y. Bai, and S. W. Tighe, *Real-time DNA sequencing in the antarctic dry valleys using the Oxford nanopore sequencer,* Journal of Biomolecular Techniques **28**, 2 (2017).

[36] T. Hoenen, A. Groseth, K. Rosenke, R. J. Fischer, A. Hoenen, S. D. Judson, C. Martellaro, D. Falzarano, A. Marzi, R. B. Squires, K. R. Wollenberg, E. De Wit, J. Prescott, D. Safronetz, N. Van Doremalen, T. Bushmaker, F. Feldmann, K. McNally, F. K. Bolay, B. Fields, T. Sealy, M. Rayfield, S. T. Nichol, K. C. Zoon, M. Massaquoi, V. J. Munster, and H. Feldmann, *Nanopore sequencing as a rapidly deployable Ebola outbreak tool,* Emerging Infectious Diseases **22**, 331 (2016).

[37] S. L. Castro-Wallace, C. Y. Chiu, K. K. John, S. E. Stahl, K. H. Rubins, A. B. McIntyre, J. P. Dworkin, M. L. Lupisella, D. J. Smith, D. J. Botkin, T. A. Stephenson, S. Juul, D. J. Turner, F. Izquierdo, S. Federman, D. Stryke, S. Somasekar, N. Alexander, G. Yu, C. E. Mason, and A. S. Burton, *Nanopore DNA Sequencing and Genome Assembly on the International Space Station,* Scientific Reports **7**, 1 (2017).

[38] A. B. McIntyre, L. Rizzardi, A. M. Yu, N. Alexander, G. L. Rosen, D. J. Botkin, S. E. Stahl, K. K. John, S. L. Castro-Wallace, K. McGrath, A. S. Burton, A. P. Feinberg, and C. E. Mason, *Nanopore sequencing in microgravity,* npj Microgravity **2**, 1 (2016).

[39] *Media resources-oxford nanopore technologies,* `https://nanoporetech.com/about-us/for-the-media` (2020).

[40] *Next generation sequencing market size | industry report, 2027,* (2019).

[41] *Next generation sequencing (ngs) market size, trends| forecast 2026,* (2019).

[42] L. Restrepo-Pérez, C. H. Wong, G. Maglia, C. Dekker, and C. Joo, *Label-Free Detection of Post-translational Modifications with a Nanopore,* Nano Letters **19**, 7957 (2019).

2

SINGLE-MOLECULE IONIC AND OPTICAL SENSING WITH NANOAPERTURES

Solid-state nanoapertures (nanometer sized holes within a membrane) allow for the interrogation of single molecules by probing them within their nanoscale volume through which molecules pass in a single-file manner. Molecules are probed using two main techniques: ionic sensing where a salt solution and applied voltage is used to produce an ionic current through the nanopore, and optical sensing through a shift in the resonance wavelength of the plasmonic nanoaperture. Here, we briefly review the basic principles, applications, and challenges in sensing with solid-state nanoapertures, as well as some strategies for further improvements. We compare the complimentary features of the two approaches and highlight recent attempts to combine them into new sensing platforms.

2.1. INTRODUCTION

All biosensors can be categorized by the size of their sensing region which is important for their detection sensitivity. By constraining a sensor to a small enough volume and by tuning the concentration of the analyte to low values, even single molecules can be sensed and studied [1–3]. Properties on the single-molecule level often differ from ensemble studies [4–6]. For example, transient intermittent conformational states of proteins, which are important for an understanding of their function, are often lost with ensemble techniques such as crystallography [7–9]. Similarly, detection of single-base mutations in the DNA sequence (known as single nucleotide polymorphisms) which are only present on some DNA strands, are quickly lost in the background signal when an ensemble of DNA molecules is sequenced [10, 11]. Indeed, the ability for sensing on the single-molecule level is important for both the understanding of biological processes as well as in applications for diagnostics [12–15].

Solid-state nanopores are a common way of building such single-molecule sensors. Here one etches a tiny hole (aperture) into a solid-state membrane which allows single molecules to physically pass by, as they are small enough to fit, similar to a molecular tunnel [16]. The apertures need to be reliably fabricated on the nanometer scale the size scale of single biomolecules —in order to physically restrict the passage of molecules to a single-file manner. During the passage of the molecule, its properties can be probed. Interestingly, in cells, such pores are formed naturally within the membranes of cells where they serve to control the passage of molecules like DNA, RNA, and proteins. However, such biological pores are hard to integrate into solid-state platforms as the fabrication of such systems requires a wide range of material science, engineering, and nanofabrication techniques [1, 17, 18]. Fortunately, the rapid development and the increasing availability of nanolitho graphy techniques in the last few decades have enabled the top-down fabrication of similar solid-state nanoapertures [19]. Apertures, of various shapes on the scale of one to many tens of nanometers, can be reliably formed in a variety of different solid-state membranes such as silicon nitride. The use of novel 2D materials has pushed the membrane thickness and therefore volume of the sensing region even down to the ultimate thickness of a single atomic layer [20].

We define a nanoaperture to be a nanometer-sized hole (of varying shape and with lateral dimensions of 1-100nm) that is fabricated within a free-standing membrane that is of a similar thickness. In this chapter, we cover two common ways to probe the passage of the molecules of interest through such nanoapertures. First, ionic sensing which involves the detection of a temporary blockade in the ionic current when molecules translocates through the nanopore [21]. Second, optical sensing where a change is detected in the light transmission or reflection upon the passage of the molecule, due to a change in the optical resonance of the nanoaperture (which will be further explained below) [22]. Notably, both of these methods do not require the biomolecule of interest to be labelled. Such label-free techniques are to be preferred over other single-molecule techniques such as electron microscopy, fluorescence microscopy, or force techniques such as AFM or optical/magnetic tweezers, that all require the use of labels such as heavy-atom stains in electron microscopy, fluorophores in fluorescence techniques, and attachment groups for force spectroscopy, which might alter the native behavior of the molecule of interest [23–25]. Below, we introduce the ionic and optical sensing tech-

niques, describe a few applications, and lay out the limitations and challenges facing each approach.

2.2. PRINCIPLE OF IONIC CURRENT SENSING WITH NANOPORES

A long-standing idea in biosensing has been to monitor blockades in the in order to detect single particles. This idea was first proposed by Wallace Coulter in the 1940s for the screening and counting of blood cells [26]. In so-called 'Coulter counters', a blood sample is diluted in an ionic solution such as NaCl, and an electric field is applied through a voltage difference between both reservoirs, driving ions through an aperture (which here was ~10 μm diameter). This narrow constriction provides a resistance in the ionic current because it constricts the flow of ions. When the particle of interest, here a blood cell, passes through the constriction, the flow of ions is temporarily disrupted, causing a measurable change in the ionic current. This sensing principle was later extended to single-molecule detection with nano-constrictions such as nanopores (~1-50nm), where the passage of a single DNA causes a measurable change in the ionic current [1, 27–29] (Fig.2.1a).

The current through such a nanopore is, to first approximation, given by equation 2.1 [33]:

$$i_{\text{open pore current}(d)} = n(\mu_{\text{cation}} + \mu_{\text{anion}})eV * \frac{1}{R} \qquad (2.1)$$

where n is the number density of charge carriers in solution, μ_{cation} and μ_{anion} are the electrophoretic mobility of the cation and anions, respectively, V is the applied voltage, and R is the geometric resistance of the nanoconstriction which is given by equation 2.2 [34]:

$$R(d) = n(\mu_{\text{cation}} + \mu_{\text{anion}})eV * \frac{1}{R} \qquad (2.2)$$

where L is the approximate thickness of the membrane and d is the diameter of the nanopore. In most literature, the conductance rather than the current is reported, which is given by G=i$_{\text{open pore current}}$ /V.

When an analyte passes through the constriction, it disrupts the flow of ions by way of the excluded volume, thereby inducing a lower pore conductance. This change in conductance is given by equation 2.3:

$$\Delta G = G_{\text{open pore current}} - G_{\text{analyte}} = G(d) - G(d_{\text{reduced}}) \qquad (2.3)$$

where G$_{\text{analyte}}$ is the reduced ionic conductance of the nanopore when the analyte resides in the pore. For an extended object that spans the entire thickness of the pore (such as a long DNA molecule), this d$_{\text{reduced}}$ is equal to the new effective diameter from the reduction of the open pore volume that is now occupied by the analyte equation 2.4 :

$$d_{\text{reduced}} = \sqrt{d^2 - d_{\text{analyte}}^2} \qquad (2.4)$$

2
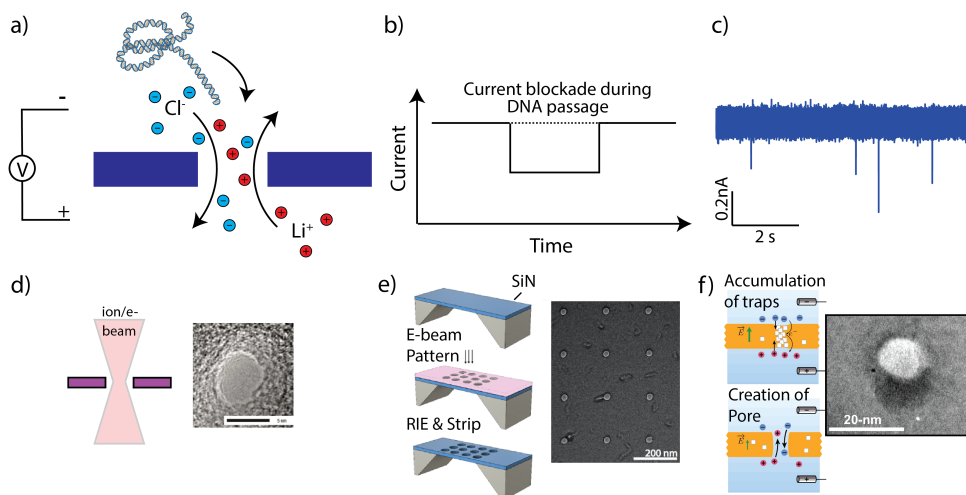
Figure 2.1: **Overview of ionic sensing and fabrication of nanopores** a) Schematic overview of ionic sensing. A nanoaperture is immersed in an ionic solution (pictured here with LiCl) and a voltage difference is applied. Ions in the solution are electrophoretically driven to the respective electrodes. Charged biomolecules such as DNA can also be driven through this nanoaperture. b) Illustration of the current blockade during the DNA passage of the nanopore. When a molecule such as DNA enters the nanopore, it temporarily blocks the flow of ions leading to a measurable decrease in the current during the time of passage. c) Example trace of the ionic current (100mV, 1M LiCl) through an 15 nm nanopore, showing clear dips in the current each time a DNA molecule translocates (20kbp, 1ng/μl). d) Illustration of ion/electron beam milling of SiN membranes for nanopores. Typically, the electron beam needs to be ~200 keV to be able to mill away the Silicon Nitride membrane. Nanopore image on the right is from the first application of a TEM drilling of nanopores, reproduced from [30]. e) An array of nanopores produced with e-beam lithography and reactive ion etching. Reproduced from [31]. f) Illustration of nanopores produced by dielectric breakdown of SiN membranes. A voltage is applied across an insulating membrane which causes charges to accumulate at a defect site. This leads the membrane to locally collapse and produce a nanopore. Reproduced from [32].

where $d_{analyte}$ is the diameter of the rod that approximates the analyte (2.2 nm for the case of DNA), see Fig.2.1b. Fig. 2.1c shows an example of ionic current trace for a buffer of 2M LiCl containing DNA. Clear dips can be seen which are caused by the passage of individual DNA molecules. Equation 2.3 highlight a few parameters that are crucial for ionic sensing: the salt concentration, the applied voltage which supplies the driving force to force the molecule through the constriction, and the size of the constriction that defines the geometric resistance [35, 36].

The nanoscale apertures for ionic sensing are usually fabricated in a thin membrane (such as 5-20nm thick SiN membrane) through direct-milling techniques with an electron beam in a Transmission Electron Microscope (TEM), typically with electron energies over 200KeV or with a Focused Ion Beam (FIB) [30, 37, 38] (Fig.2.1d). In recent years, more accessible pore-fabrication techniques have been developed such as nanolithography combined with a dry etching (Fig.2.1e) or dielectric breakdown of the membrane by applying a large voltage across the membrane (Fig.2.1f) [31, 32, 39–41]. There has also been a drive to control the fabrication of such pores down to the precision of a single atom with crystalline 2D materials and advanced milling techniques [42, 43].
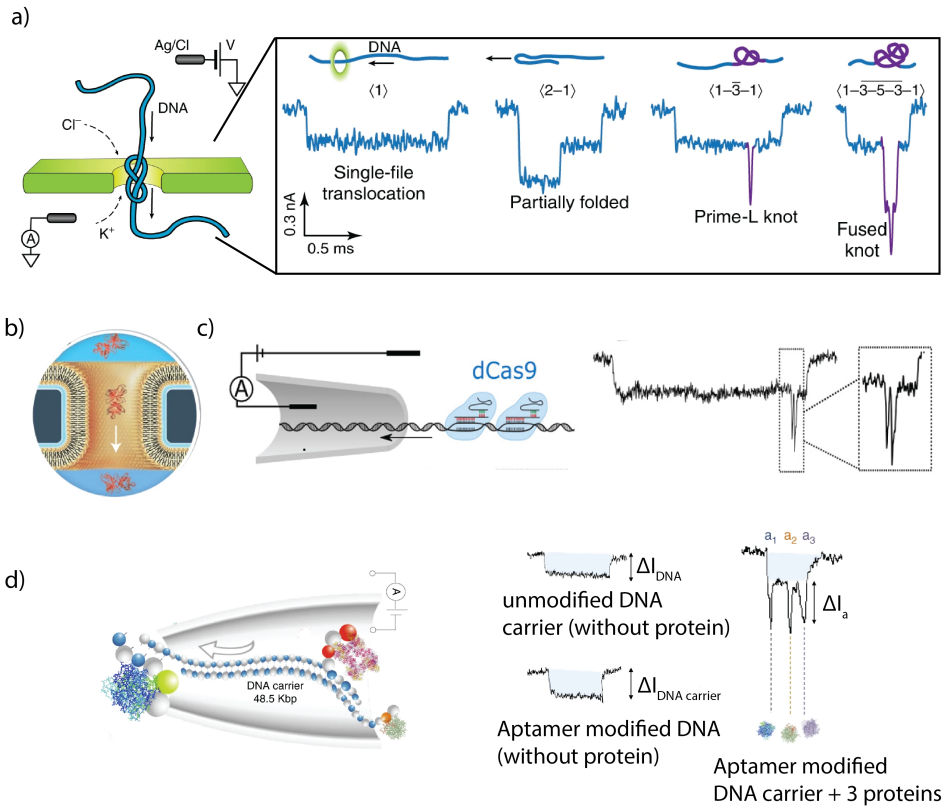
Figure 2.2: **Ionic-sensing application of nanopores** a) Sensing of DNA folds and knots in solid-state nanopore, which show up as distinct shapes in the ionic current blockades. The depth of the blockade is quantized according to the number of strands of the DNA that simultaneously resides in the pore. Reproduced from [44]. b) Detection of proteins in a lipid-coated solid-state nanopore to discriminate between the size, shape, and charge of the proteins. Reproduced from [45]. c) Detection of CRISPR/dCas9 bound on DNA. Due to their larger physical size, the CRISPR/dCas9 complex show up as additional blockade on top of the DNA blockade current. Since the proteins are programmable to bind any target sequence, specific sequences along the DNA can be targeted for detection and fingerprinting of the DNA. Reproduced from [46]. d) Sensing of proteins with DNA aptamers. Specific DNA sequences allows for binding of certain proteins, thereby facilitating their detection and identification. Reproduced from [47].

2.3. APPLICATION OF IONIC SENSING IN NANOPORE EXPERIMENTS

Ionic sensing has been successfully applied to the sensing of single DNA molecules. Most applications with solid-state nanopores focus on a fundamental biophysical understanding of the polymer physics of the translocating DNA. Different polymer configurations are adopted by DNA as it translocates through the nanopore, as already observed in the earliest work on solid-state nanopores [48–50]. This spawn interest in using nanopores as a tool to probe DNA polymer physics on the nanoscopic scale, an order of
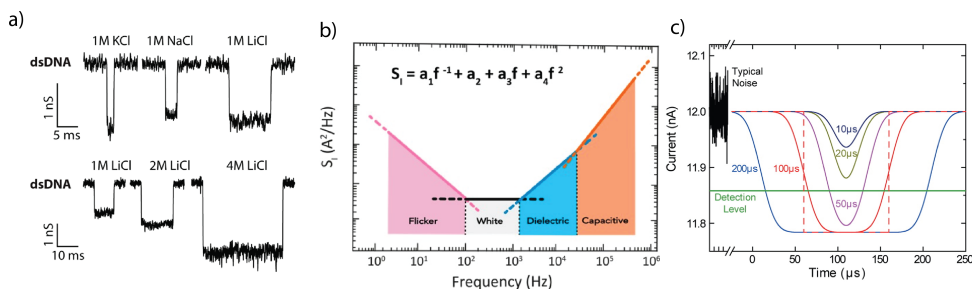
Figure 2.3: **Signals and noise in solid-state nanopores** a) DNA blockade signals in buffers with different concentrations and types of salt. Reproduced from [56]. b) Power spectrum density of the nanopore ionic current, with the main noise regions indicated. Reproduced from [57]. c) Depth of ionic blockade with different low-pass frequency filters. For the same input signal, the resultant signal is plotted after the different low pass filter is applied. The low pass filter distorts the maximum depth of the current blockade due to the different temporal resolution of the low pass filter. If a detection level is set (green line), the signal passed through the 10, 20 μs (100, 50 KHz) will not pass this cut off. Reproduced from [58].

magnitude smaller than the typical sub-micrometer resolution of fluorescence-based techniques. More recently, the groups of Dekker and Garaj (Fig.2.2a) used solid-state nanopores to study DNA folds and knots [44, 51] where they interrogated thousands of DNA at the single-molecule level to elucidate the behavior of DNA knots. Nanopores have also been used to detect and identify single proteins [52], for example, in work by Mayer et al who used lipid-coated solid-state nanopores to determine the size, shape, and charge of single proteins based on differences in the ionic current [45] (Fig.2.2b).

The success of solid-state nanopores to interrogate molecules has inspired nanopore-based diagnostic applications. As the nanopore sensing principle revolves around the sensitivity of the ionic current to the size of the object, people have started using locally bound proteins to fingerprint DNA, as the proteins yield measurable spikes above the DNA-only blockade level (such as in RecA-coated DNA or streptavidin-biotin-tagged DNA [53, 54]). Recent work has focused on CRISPR/dCas9 proteins that bind particular DNA sequences. Weckman et al and Yang et al. showed that differences as small as a single base mutation can lead to detectable changes in the protein-binding rate to DNA, opening up applications in screening for single-nucleotide polymorphism [46, 55] (Fig.2.2c). Alternatively, Edel et al. explored the use of aptamers, DNA sequences that are specially designed to bind specific proteins, to screen for the presence of certain proteins in human serum [47] (Figure 2.2d). These efforts illustrate the application of nanopores to real world diagnostics applications beyond just biophysics experiments in a research setting.

2.4. LIMITATIONS AND CHALLENGES OF IONIC SENSING

Though successful in such applications, the ionic-sensing approach suffers from several limitations. First, it requires the use of an ionic liquid as the signal scales with concentration of salt dissolved (typically 0.3-4 M) [56]. The higher the salt concentration, the higher the conductivity of the liquid and therefore the higher the current obtained (Fig2.3a). However, high-salt solutions are usually detrimental for many biomolecules

which require physiological conditions (0.1-0.25M) as high salt interferes with the proper binding and functioning of proteins which are often mediated by electrostatic interactions [59]. Second, ionic current sensing with nanopores comes with a fair amount of noise. A wide range of electrical noise sources contributes across the frequency spectrum, as illustrated in Figure2.3b. For an in depth look at each of the noise sources, we refer to the recent review by Fragasso et al. [57]. In brief, it is challenging to eliminate or control all these sources of noise, for example, those that arise from chemical processes happening on the membrane surface (e.g., transient binding and unbinding of ions to defect sites) which are very hard to prevent [57, 60–62]. Third, there is a limit to the temporal resolution that can be achieved in ionic sensing. Molecules, driven by the electrophoretic force from the applied electric field, typically transverse very quickly across the nanosized apertures (< 5 μs for proteins and < 0.5 μs for each bp in a 10kbp long DNA) [58, 63]. Many commercial amplifier have a bandwidth limitation of ~50KHz (20μs), making it impossible to resolve the full blockade of relevant analytes. Furthermore, low-pass filters are typically applied to eliminate high-frequency electrical noise, which further exacerbates the problem as it reduces the signal from the translocation event by clipping the full depth of the nanopore event (See Fig.2.3c).

Various solutions have been proposed to address these problems. Newly developed amplifiers and the miniaturization and integration of on-chip CMOS preamplifiers with solid-state nanopores have pushed the temporal resolution to the 10 MHz range (0.1 μs) [64]. Effective operation with such amplifiers, however, still need low-noise nanopores. New nanopore chips are being developed with glass support or additional insulating layers that lower the capacitance and hence lower the electrical noise [65, 66]. Furthermore, with the advent of 2D materials, membranes fabricated from a single or few layer graphene or hexagonal boron nitride have been explored [42, 67]. These membranes can be as thin as a single atomic layer which is the ultimate limit in terms of the sensing volume that a membrane can define. An added bonus feature is that many 2D materials have remarkable electronic transport properties which can be used to sense biomolecules in complementary ways to conventional ionic sensing schemes such as through sensing of tunneling and gating currents in the 2D membrane [68–70].

2.5. Optical sensing in plasmonic apertures

We now turn to a complimentary sensing technique, the monitoring of optical transmission through the nanoaperture. Classically, it was thought that nanoapertures with subwavelength dimensions (~100nm) were too small for significant light transmission and hence for optical readout methods to be employed [75]. However, the report of extraordinary transmission through nanoapertures [76], where the magnitude of transmission was measured to be orders of magnitude higher than classically predicted, overturned this idea and reinvigorated the exploration of optical readout methods to probe the nanoscale volumes confined by a small aperture.

Central to the phenomenon of extraordinary transmission of light is the role of surface plasmons that are excited in plasmonic materials such as gold or silver films. These plasmonic oscillations of electrons in the metal can focus the incident electromagnetic (EM) field to the aperture, which gives rise to the enhancement of scattered and transmitted light [77]. Transmission of light though these apertures strongly depends on the

2
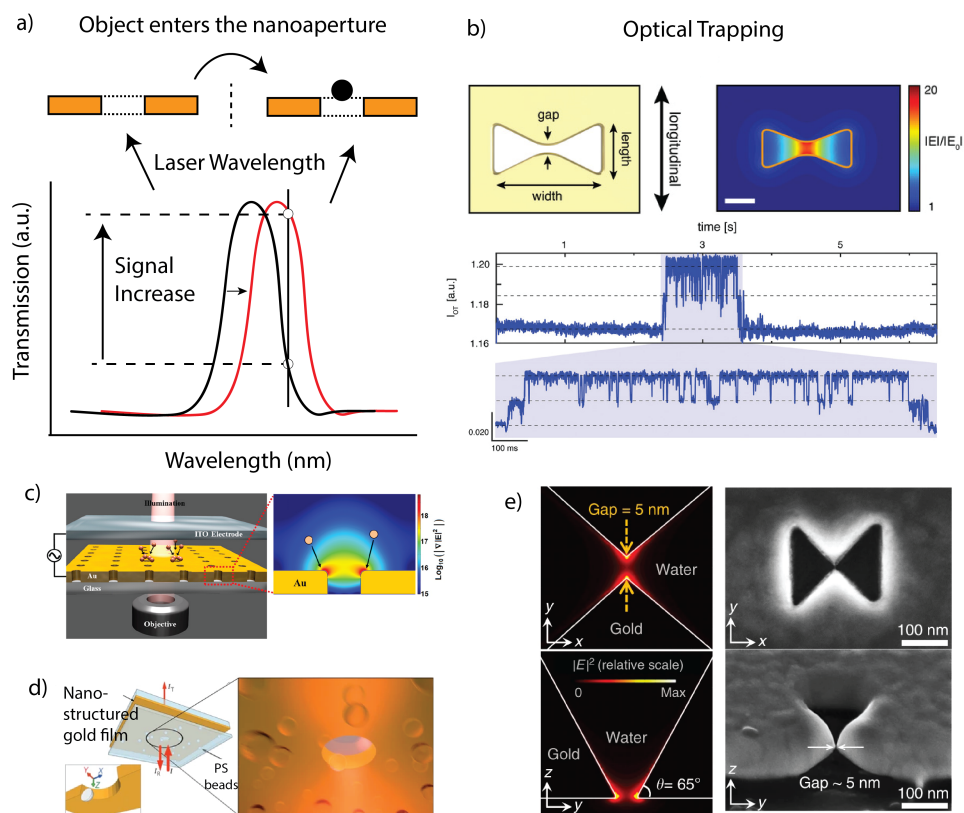
Figure 2.4: **Optical detection and trapping with nanoapertures** a) Illustration of the sensing principle. A nanoaperture has a peak wavelength where the transmission through the aperture is the highest (black curve). A laser is parked at a wavelength slightly detuned from the resonant wavelength peak. When an object of a higher refractive enters the aperture, the resonant wavelength is redshifted (red curve). This increases the transmission through the nanoaperture. b) Optical trapping in a nanoaperture. A gold nanoaperture focuses the incident E-field to the center of the bowtie. The accompanying field gradient gives rise to an optical trapping force similar to optical tweezers. Small objects such as proteins can be trapped in the nanoaperture. Shown here is the trapping signal from a beta-amylase protein. Reproduced from [71]. c-e) Examples of various nanoapertures that produces an E-field gradient and trapping force. Shapes vary from round holes of 100nm to inverted bowtie structures with features <5 nm in scale. Reproduced from [72–74].

wavelength of the incident light and the size/geometry of the aperture, typically showing a resonance peak at a particular wavelength. As the resonant wavelength, where transmission is maximum, is very sensitive to the surrounding refractive index enclosing the nanoaperture, small modulations, such as a protein or molecule occupying the nanoaperture volume, can lead to a measurable redshift in the wavelength of the resonance peak. Figure 2.4a illustrates this principle of optical detection. Notably, this can lead to a decrease or an increase of the measured transmission signal: if the incident wavelength was lower than the resonant peak wavelength (i.e., on the left of the peak of the back curve in Figure 4a), there will be a decrease in the transmission when the peak

is redshifted, while there will be an increase in the transmission if the laser wavelength was higher than the resonant wavelength (right of the peak as drawn in Fig.2.4a). The change in the transmitted light can be detected with a fast photodetector, typically an avalanche photodiode (APD). This has inspired a new class of sensors with optical read-out methods that are based on detecting this resonance-wavelength shift in either the transmitted or reflected light.

Additionally, the tight focusing of the incident optical light produces strong optical gradients within the nanoaperture, yielding a trapping force on the particle in the aperture, similar to that of an optical tweezer. This can be employed as nanotweezers to hold the molecule in place for sensing [72, 78, 79]. Finite-difference time-domain method (FDTD) simulations of the EM field in the structures estimate these EM gradients for a variety of different structures (Fig2.4b-c). They produce a gradient force given by Eqn 2.5 :

$$F = \frac{1}{2}\alpha \triangledown E^2 \tag{2.5}$$

where α is the polarizability of the particle and $\triangledown E^2$ is the magnitude of the gradient of the EM field E. Figure2.4b shows an example of such a structure that exhibits a strong gradient within the gap of the inverted bowtie.

For optical detection, nanoapertures are typically fabricated in a plasmonic material such as a thin gold film that is thick enough to block transmitted light to ensure that only the nanoaperture is responsible for the transmitted light. Similar to nanopores, the structures are usually milled into the film through direct ion beam milling or e-beam lithography [80–82]. Figure2.4c-e shows various structures fabricated with such techniques that were used to detect and tweeze nanoscale objects.

2.6. APPLICATION OF OPTICAL SENSING IN NANOPORES

Though the application of optical sensing and tweezing with nanoapertures is still in its infancy, early success with the tweezing of nanoparticles have led to the exploration of sensing and trapping of a variety of biological objects including bacterial cells, DNA, and single proteins [85–87]. Figure2.5a shows an array of gold nanoantennas (here fabricated as simply two parallel Au wires that were 500nm long and spaced ~30nm apart, thereby generating an optical gradient in the proximity of the antennas) were used to tweeze single E-coli [83]. Moving to smaller biomolecules, Gold nanoapertures were already employed in 2012 to optically tweeze and detect single proteins [84, 88] by the group of Gordon et al. (Figure.2.5b). Bovine serum albumin (BSA) was used as a model proteins in their double nanohole traps. When BSA was trapped, two different intensity levels could be seen above the baseline which they attribute to the two different protein conformations [89]. The same traps were also used to study a variety of reactions including binding rates of protein-antibodies [89]. Finally, Verschueren et al. and Shi et al. were able to optically detect single DNA molecules that traversed a plasmonic nanopore, in both transmission and reflection mode [71, 90] (Fig.2.5c). The DNA molecules were electrophoretically driven into the nanoapertures where they caused a shift in the resonance wavelength of the laser and a measurable change in the transmission (in this instance, a decrease). They verified their optical signal with conventional current blockade sig-

2
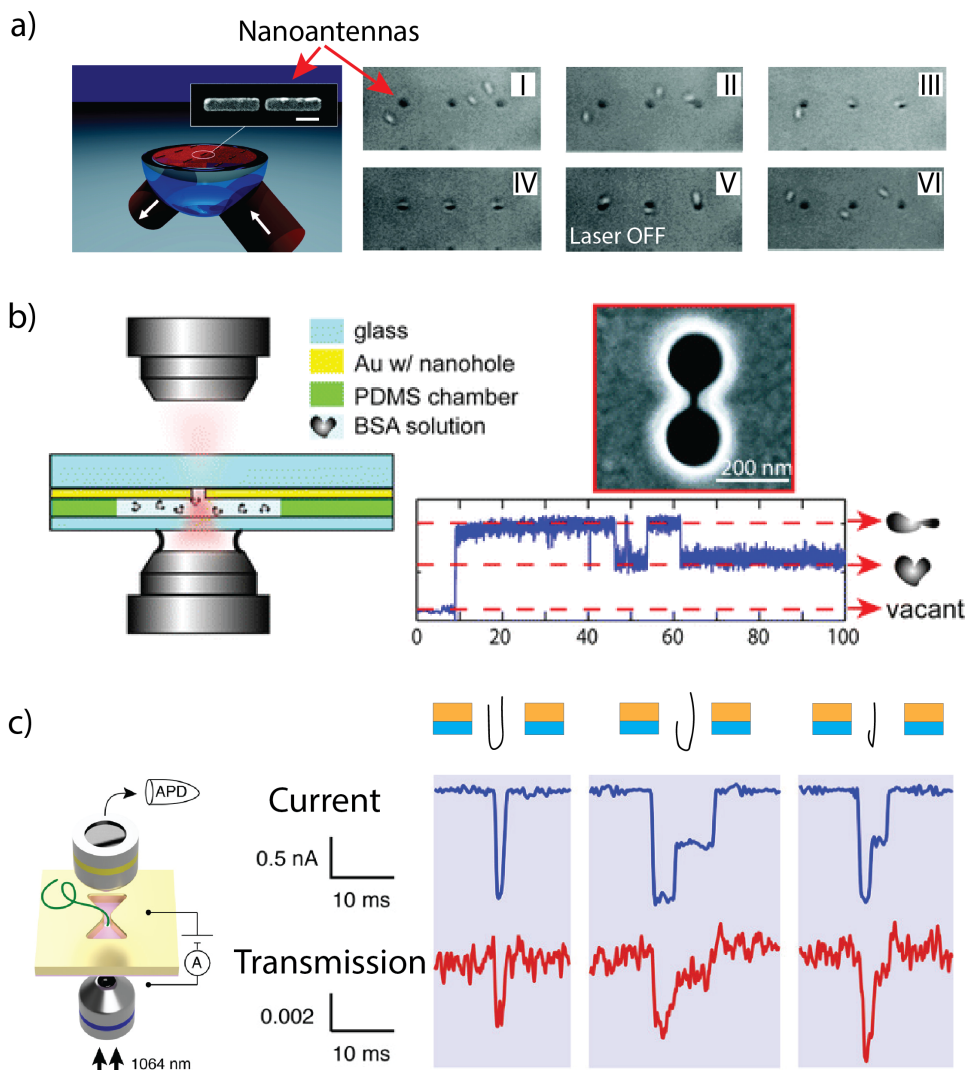
Figure 2.5: **Examples of optical detection and trapping of biomolecules in Au nanoapertures** a) Trapping of Escherichia coli bacteria with an array of Au nanoantenna. Scale bar is 200 nm. The Au nanoantenna was 500nm with a 30 nm gap between them. A set of time series shows the E. coli (white) localising to the nanoantennas (the pair of nanoantennas (1030nm) show up as black dots in the image). At time V, the incident laser was switched off and the E.coli was released from the vicinity of the nanoantennas indicating that they had been optically trapped. Reproduced from [83]. b) Trapping of BSA proteins in a double hole nanoapertures. When a single protein is trapped, two different intensity levels are observed, associated with two different conformational shapes [84]. c) Detection of DNA in Au nanoapertures. When DNA is electrophoretically driven into an inverted-bowtie-shaped nanoaperture, the ionic and optical signals can be simultaneously detected. Reproduced from [71].

nal from ionic sensing. Notably, even folds in the DNA during the passage through the nanoaperture led to a corresponding change in the optical signal.

These studies show some of the many exciting features of label-free biosensing. There is also the ability for multiplex sensing of parallel apertures where a high density of these sensors can be packed into a small volume and simultaneously read out, because each nanoaperture can be independently measured optically. Notably, optical sensing is independent of buffer solutions unlike ionic sensing which requires a salt solution, allowing native physiological buffers to be used [91]. The noise sources for optical readout methods are very different from the noise sources affecting electrical readout methods. They are usually dictated by sources in the far-field such as the laser source and aberrations in the optical components, rather than in local conditions such as surface effects. Finally, optical signals can be acquired by photodetectors at a much higher temporal resolution (as fast as picoseconds or 10^{12} Hz), fast enough to observe protein dynamics.

2.7. LIMITATIONS AND CHALLENGES IN OPTICAL SENSING

Yet, as any technique, optical sensing with nanoapertures also has some limitations. First, the fabrication of nanoapertures is extremely difficult because the plasmon response are very sensitive to small (~nm) geometric changes which can shift the resonance and thus decrease the sensitivity of the nanoaperture. Complex shapes with a well-defined sensing region are hard to produce as the fabrication process quickly reduces the sharpness of the structure, giving it rounded edges which damp out the plasmons and the focusing of the EM field. Generally, the fabrication process is critical, yet difficult to control and consistently reproduce. Second, the use of the laser source for the readout method can cause local heating which may lead to denaturation of proteins. Moreover, heating may introduce convection currents near the surface that decrease the potential well of the trapping force, allowing trapped objects to escape [92]. Lastly, unlike for conventional optical tweezers, there is a lack of detailed models for the trapping of single molecules [93].

Many of the challenges with nano-optical traps relate to the relative infancy of the technology. Various strategies are being explored to circumvent the above listed challenges. The limits of nanofabrication techniques can be pushed for example, from the current effectively ~5 nm scale [80, 94, 95] (set by the resolution of the resist used) with e-beam lithography and laser interferometry, to the 1-2 nm scale using maskless direct-milling techniques [82]. An interesting approach to circumvent resolution issues is to simply fabricate a huge array of structures on the same gold film [81], with each slightly different geometries and scanned with the laser to find structures that are ideal for optical sensing and trapping. Second, local heating from the impinging laser beam can be reduced by the use of heat sinks surrounding the nanoapertures [96]. Third, attempts are underway to improve modelling of nano-optical tweezers in order to better model probe and understand the nanoscale forces in the nanoaperture and guide future designs of such nanotraps [72, 79].
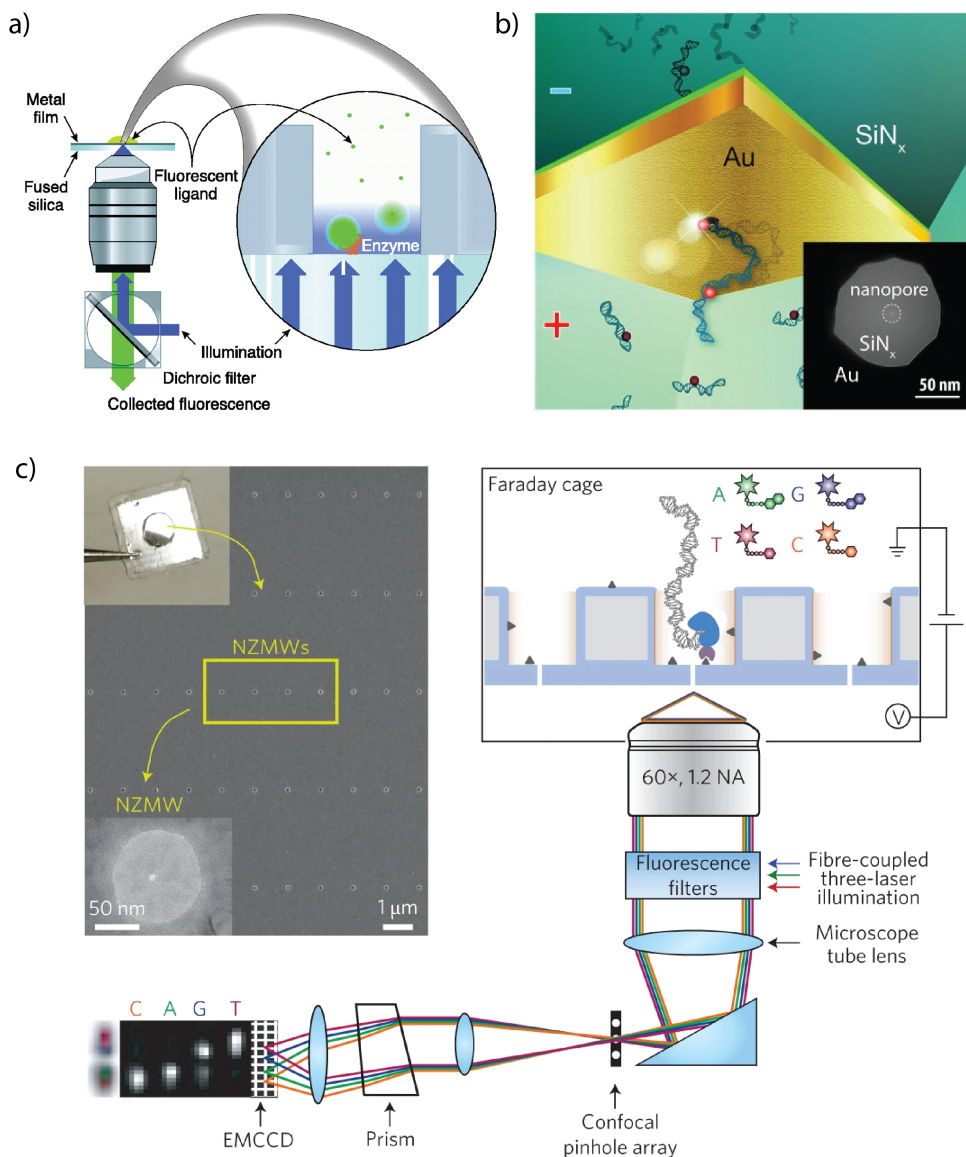
Figure 2.6: **Combined optical-ionic nanopores** a) Zero mode waveguides where an aperture is fabricated in a thin metal film to sense single enzymes. At the bottom of the well, a DNA polymerase complex is bound that produces a fluorescence signal that can be used to identify the DNA sequence of interest. Reproduced from [97]. b) Illustration of a nanowell milled in a thin gold film with an integrated nanopore termed "opto-nanopore". The nanopore is used to electrophoretically drive the DNA into the sensing area where it is optically sensed. Reproduced from [98]. c) Integration of a zero-mode waveguide with a nanopore that drives DNA molecules to the sensing area. Reproduced from [99].

2.8. SIMULTANEOUS IONIC AND OPTICAL SENSING

In the preceding sections, we have covered the features and limitations of both the ionic and optical sensing approaches. Given their complimentary advantages, efforts are ongoing to develop new sensors that combine the optical and ionic readout readouts. A variety of schemes are proposed to combine the thermophoretic (a byproduct of the optical readout) and electrophoretic effect to transport particles to targeted sensing area [100]. One such approach builds upon zero mode waveguides which are a class of nanoapertures where the fluorescence is enhanced in strongly localised regions, which can be used to sense single enzymes (Fig.2.6 a) [97]. However, these devices suffered from a lack of active delivery of the biomolecules into the sensing region. Wanunu et al. took inspiration from ionic sensing approaches and integrated a nanopore at the bottom of the zero-mode waveguide well where a DNA polymerase was assembled, in order to deterministically drive and deliver DNA for sequencing (Fig.2.6c) with a fluorescent readout method [99]. Similarly, Meller et al. developed what they called "opto-nanopores" where they integrated a nanopore at the bottom of the well of a nanoaperture (Fig.2.6b), thus allowing them to combine ionic sensing techniques in nanopores with a variety of optical readout methods for high-bandwidth measurements [101–103]. They, along with others, demonstrate optical detection and fingerprinting of DNA molecules through the use of fluorescent labels [71, 90]. The expansion of research in combining ionic and optical sensing in nanoapertures also led to the discovery that nanopores can be directly fabricated in thin SiN membranes with a laser beam. This opens up yet another scalable avenue for the reliable fabrication of nanopore arrays [104, 105].

2.9. SUMMARY AND OUTLOOK

Summing up, nanoapertures define a sensing volume that can be probed with an ionic current or through optical sensing at the single-molecule level. The two approaches offer complimentary advantages and recent attempts to combine them have led to the advent of a new class of optical nanopores for detection and manipulation of single biomolecules. These nanosensors will increasingly be benificial for a fundamental understanding of biology as well as for real-world applications such as the detection of biomarkers in point-of-care devices.

REFERENCES

[1] D. Branton, D. W. Deamer, A. Marziali, H. Bayley, S. A. Benner, T. Butler, M. Di Ventra, S. Garaj, A. Hibbs, X. Huang, S. B. Jovanovich, P. S. Krstic, S. Lindsay, X. S. Ling, C. H. Mastrangelo, A. Meller, J. S. Oliver, Y. V. Pershin, J. M. Ramsey, R. Riehn, G. V. Soni, V. Tabard-Cossa, M. Wanunu, M. Wiggin, and J. A. Schloss, *The potential and challenges of nanopore sequencing, Nature Biotechnology*, **26**, 1146 (2008).

[2] L. Restrepo-Pérez, C. Joo, and C. Dekker, *Paving the way to single-molecule protein sequencing,* Nature Nanotechnology **13**, 786 (2018).

[3] J. J. Kasianowicz and S. M. Bezrukov, *On 'three decades of nanopore sequencing',* Nature Biotechnology **34** (2016).

[4] J. Zlatanova and K. van Holde, *Single-Molecule Biology: What Is It and How Does It Work? Molecular Cell*, **24**, 317 (2006).

[5] T. Ha, A. G. Kozlov, and T. M. Lohman, *Single-molecule views of protein movement on single-stranded DNA, Annual Review of Biophysics*, (2012).

[6] W. Zhang, M. Caldarola, X. Lu, B. Pradhan, and M. Orrit, *Single-molecule fluorescence enhancement of a near-infrared dye by gold nanorods using DNA transient binding,* Physical Chemistry Chemical Physics **20**, 20468 (2018).

[7] K. R. Acharya and M. D. Lloyd, *The advantages and limitations of protein crystal structures,* Trends in Pharmacological Sciences **26**, 10 (2005).

[8] X. Michalet, S. Weiss, and M. Jäger, *Single-molecule fluorescence studies of protein folding and conformational dynamics, Chemical Reviews*, **106**, 1785 (2006).

[9] E. Kim, M. D. Baaske, I. Schuldes, P. S. Wilsch, and F. Vollmer, *Label-free optical detection of single enzyme-reactant reactions and associated conformational changes,* Science Advances **3**, e1603044 (2017).

[10] J. Kong, J. Zhu, and U. F. Keyser, *Single molecule based SNP detection using designed DNA carriers and solid-state nanopores,* Chemical Communications **53**, 436 (2017).

[11] Q. Zhao, G. Sigalov, V. Dimitrov, B. Dorvel, U. Mirsaidov, S. Sligar, A. Aksimentiev, and G. Timp, *Detecting SNPs using a synthetic nanopore,* Nano Letters **7**, 1680 (2007).

[12] A. M. Armani, R. P. Kulkarni, S. E. Fraser, R. C. Flagan, and K. J. Vahala, *Label-free, single-molecule detection with optical microcavities,* Science **317**, 783 (2007).

[13] D. C. Perez-Gonzalez and J. C. Penedo, *Single-Molecule Strategies for DNA and RNA Diagnostics* (Springer, Cham, 2015) pp. 297–332.

[14] D. R. Walt, *Optical methods for single molecule detection and analysis,* Analytical Chemistry **85**, 1258 (2013).

2

[15] E. Kim, M. D. Baaske, and F. Vollmer, *Towards next-generation label-free biosensors: recent advances in whispering gallery mode sensors, Lab on a Chip,* **17**, 1190 (2017).

[16] M. Muthukumar, C. Plesa, and C. Dekker, *Single-molecule sensing with nanopores,* Physics Today **68**, 40 (2015).

[17] N. Varongchayakul, J. Song, A. Meller, and M. W. Grinstaff, *Single-molecule protein sensing in a nanopore: a tutorial, Chemical Society reviews,* **47**, 8512 (2018).

[18] Y. Feng, Y. Zhang, C. Ying, D. Wang, and C. Du, *Nanopore-based Fourth-generation DNA Sequencing Technology,* Genomics, Proteomics & Bioinformatics **13**, 4 (2015).

[19] Q. Chen and Z. Liu, *Sensors (Switzerland),* Vol. 19 (MDPI AG, 2019).

[20] S. Garaj, W. Hubbard, A. Reina, J. Kong, D. Branton, and J. A. Golovchenko, *Graphene as a subnanometre trans-electrode membrane,* Nature **467**, 190 (2010).

[21] J. J. Kasianowicz, E. Brandin, D. Branton, and D. W. Deamer, *Characterization of individual polynucleotide molecules using a membrane channel,* Proceedings of the National Academy of Sciences of the United States of America **93**, 13770 (1996).

[22] Y. Xu, P. Bai, X. Zhou, Y. Akimov, C. E. Png, L.-K. Ang, W. Knoll, and L. Wu, *Optical Refractive Index Sensors with Plasmonic and Photonic Structures: Promising and Inconvenient Truth,* Advanced Optical Materials **7**, 1801433 (2019).

[23] H. Miller, Z. Zhou, J. Shepherd, A. J. Wollman, and M. C. Leake, *Single-molecule techniques in biophysics: A review of the progress in methods and applications, Reports on Progress in Physics,* **81**, 024601 (2018).

[24] B. Hellenkamp, S. Schmid, O. Doroshenko, O. Opanasyuk, R. Kühnemuth, S. R. Adariani, B. Ambrose, M. Aznauryan, A. Barth, V. Birkedal, *et al.*, *Precision and accuracy of single-molecule fret measurements—a multi-laboratory benchmark study,* Nature methods **15**, 669 (2018).

[25] M. Götz, P. Wortmann, S. Schmid, and T. Hugel, *A Multicolor Single-Molecule FRET Approach to Study Protein Dynamics and Interactions Simultaneously, Methods in Enzymology,* **581**, 487 (2016).

[26] W. H. Couter, *Means for counting particles suspended in a fluid,* Tech. Rep. (1953).

[27] H. Bayley and C. R. Martin, *Resistive-pulse sensing - from microbes to molecules,* Chemical Reviews **100**, 2575 (2000).

[28] M. Wanunu, *Nanopores: A journey towards DNA sequencing, Physics of Life Reviews,* **9**, 125 (2012).

[29] T. Albrecht, *Single-Molecule Analysis with Solid-State Nanopores,* Annual Review of Analytical Chemistry **12**, 371 (2019).

[30] A. J. Storm, J. H. Chen, X. S. Ling, H. W. Zandbergen, and C. Dekker, *Fabrication of solid-state nanopores with single-nanometre precision,* Nature Materials **2**, 537 (2003).

[31] D. V. Verschueren, W. Yang, and C. Dekker, *Lithography-based fabrication of nanopore arrays in freestanding SiN and graphene membranes,* Nanotechnology **29**, 145302 (2018).

[32] H. Kwok, K. Briggs, and V. Tabard-Cossa, *Nanopore Fabrication by Controlled Dielectric Breakdown,* PLoS ONE **9**, e92880 (2014).

[33] B. N. Miles, A. P. Ivanov, K. A. Wilson, F. Dogan, D. Japrung, and J. B. Edel, *Single molecule sensing with solid-state nanopores: Novel materials, methods, and applications,* Chemical Society Reviews **42**, 15 (2013).

[34] S. W. Kowalczyk, A. Y. Grosberg, Y. Rabin, and C. Dekker, *Modeling the conductance and DNA blockade of solid-state nanopores,* Nanotechnology **22**, 315101 (2011).

[35] R. M. Smeets, U. F. Keyser, D. Krapf, M. Y. Wu, N. H. Dekker, and C. Dekker, *Salt dependence of ion transport and DMA translocation through solid-state nanopores,* Nano Letters **6**, 89 (2006).

[36] D. Fologea, J. Uplinger, B. Thomas, D. S. McNabb, and J. Li, *Slowing DNA translocation in a solid-state nanopore,* Nano Letters **5**, 1734 (2005).

[37] J. Li, D. Stein, C. McMullan, D. Branton, M. J. Aziz, and J. A. Golovchenko, *Ion-beam sculpting at nanometre length scales,* Nature **412**, 166 (2001).

[38] L. D. Menard and J. M. Ramsey, *Fabrication of Sub-5 nm Nanochannels in Insulating Substrates Using Focused Ion Beam Milling,* Nano Letters **11**, 512 (2011).

[39] S. Pud, D. Verschueren, N. Vukovic, C. Plesa, M. P. Jonsson, and C. Dekker, *Self-Aligned Plasmonic Nanopores by Optically Controlled Dielectric Breakdown,* Nano Letters **15** (2015).

[40] K. Briggs, M. Charron, H. Kwok, T. Le, S. Chahal, J. Bustamante, M. Waugh, and V. Tabard-Cossa, *Kinetics of nanopore fabrication during controlled breakdown of dielectric membranes in solution,* Nanotechnology **26** (2015).

[41] Y. Zhang, Y. Miyahara, N. Derriche, W. Yang, K. Yazda, X. Capaldi, Z. Liu, P. Grutter, and W. Reisner, *Nanopore Formation via TipControlled Local Breakdown Using an Atomic Force Microscope,* Small Methods **3**, 1900147 (2019).

[42] K. Liu, M. Lihter, A. Sarathy, S. Caneva, H. Qiu, D. Deiana, V. Tileli, D. T. Alexander, S. Hofmann, D. Dumcenco, A. Kis, J. P. Leburton, and A. Radenovic, *Geometrical Effect in 2D Nanopores,* Nano Letters **17**, 4223 (2017).

[43] J. P. Thiruraman, P. Masih Das, and M. Drndic, *Stochastic ionic transport in single atomic zero-dimensional pores,* ACS nano **14**, 11831 (2020).

2

[44] R. Kumar Sharma, I. Agrawal, L. Dai, P. S. Doyle, and S. Garaj, *Complex DNA knots detected with a nanopore sensor,* Nature Communications **10**, 4473 (2019).

[45] E. C. Yusko, B. R. Bruhn, O. M. Eggenberger, J. Houghtaling, R. C. Rollings, N. C. Walsh, S. Nandivada, M. Pindrus, A. R. Hall, D. Sept, J. Li, D. S. Kalonia, and M. Mayer, *Real-time shape approximation and fingerprinting of single proteins using a nanopore,* Nature Nanotechnology **12** (2017).

[46] N. E. Weckman, N. Ermann, R. Gutierrez, K. Chen, J. Graham, R. Tivony, A. Heron, and U. F. Keyser, *Multiplexed DNA Identification Using Site Specific dCas9 Barcodes and Nanopore Sensing,* ACS Sensors **4**, 2065 (2019).

[47] J. Y. Y. Sze, A. P. Ivanov, A. E. G. Cass, and J. B. Edel, *Single molecule multiplexed nanopore protein screening in human serum using aptamer modified DNA carriers,* Nature Communications **8** (2017).

[48] J. Li, M. Gershow, D. Stein, E. Brandin, and J. A. Golovchenko, *DNA molecules and configurations in a solid-state nanopore microscope,* Nature Materials **2**, 611 (2003).

[49] M. Mihovilovic, N. Hagerty, and D. Stein, Physical Review Letters **110**, 028102 (2013).

[50] A. J. Storm, J. H. Chen, H. W. Zandbergen, and C. Dekker, *Translocation of double-strand DNA through a silicon oxide nanopore,* Physical Review E - Statistical, Nonlinear, and Soft Matter Physics **71**, 051903 (2005).

[51] C. Plesa, D. Verschueren, S. Pud, J. Van Der Torre, J. W. Ruitenberg, M. J. Witteveen, M. P. Jonsson, A. Y. Grosberg, Y. Rabin, and C. Dekker, *Direct observation of DNA knots using a solid-state nanopore,* Nature Nanotechnology **11**, 1093 (2016).

[52] C. Plesa, S. W. Kowalczyk, R. Zinsmeester, A. Y. Grosberg, Y. Rabin, and C. Dekker, *Fast translocation of proteins through solid state nanopores,* Nano Letters **13**, 658 (2013).

[53] R. M. Smeets, S. W. Kowalczyk, A. R. Hall, N. H. Dekker, and C. Dekker, *Translocation of RecA-coated double-stranded DNA through solid-state nanopores,* Nano Letters **9**, 3089 (2009).

[54] K. Chen, M. Juhasz, F. Gularek, E. Weinhold, Y. Tian, U. F. Keyser, and N. A. Bell, *Ionic Current-Based Mapping of Short Sequence Motifs in Single DNA Molecules Using Solid-State Nanopores,* Nano Letters **17**, 5199 (2017).

[55] W. Yang, L. Restrepo-Pérez, M. Bengtson, S. J. Heerema, A. Birnie, J. van der Torre, and C. Dekker, *Detection of CRISPR-dCas9 on DNA with Solid-State Nanopores,* Nano Letters **18**, 6469 (2018).

[56] S. W. Kowalczyk, D. B. Wells, A. Aksimentiev, and C. Dekker, *Slowing down DNA translocation through a nanopore in lithium chloride,* Nano Letters **12**, 1038 (2012).

[57] A. Fragasso, S. Schmid, and C. Dekker, *Comparing Current Noise in Biological and Solid-State Nanopores, ACS Nano,* **14**, 1338 (2020).

[58] C. Plesa, J. W. Ruitenberg, M. J. Witteveen, and C. Dekker, *Detection of individual proteins bound along DNA using solid-state nanopores,* Nano Letters **15** (2015), 10.1021/acs.nanolett.5b00249.

[59] S. E. Halford and J. F. Marko, *How do site-specific DNA-binding proteins find their targets? Nucleic Acids Research,* **32**, 3040 (2004).

[60] A. Fragasso, S. Pud, and C. Dekker, *1/f noise in solid-state nanopores is governed by access and surface regions,* Nanotechnology **30**, 395202 (2019).

[61] C. Wen, S. Zeng, K. Arstila, T. Sajavaara, Y. Zhu, Z. Zhang, and S. L. Zhang, *Generalized Noise Study of Solid-State Nanopores at Low Frequencies,* ACS Sensors **2**, 300 (2017).

[62] R. M. Smeets, U. F. Keyser, N. H. Dekker, and C. Dekker, *Noise in solid-state nanopores,* Proceedings of the National Academy of Sciences of the United States of America **105**, 417 (2008).

[63] C. Plesa, N. van Loo, P. Ketterer, H. Dietz, and C. Dekker, *Velocity of DNA during Translocation through a Solid-State Nanopore,* Nano Letters **15**, 732 (2015).

[64] J. K. Rosenstein, M. Wanunu, C. A. Merchant, M. Drndic, and K. L. Shepard, *Integrated nanopore sensing platform with sub-microsecond temporal resolution,* Nature Methods **9**, 487 (2012).

[65] A. Balan, C. C. Chien, R. Engelke, and M. Drndic, *Suspended Solid-state Membranes on Glass Chips with Sub 1-pF Capacitance for Biomolecule Sensing Applications,* Scientific Reports **5**, 1 (2015).

[66] M. H. Lee, A. Kumar, K. B. Park, S. Y. Cho, H. M. Kim, M. C. Lim, Y. R. Kim, and K. B. Kim, *A low-noise solid-state nanopore platform based on a highly insulating substrate,* Scientific Reports **4** (2014).

[67] G. F. Schneider, Q. Xu, S. Hage, S. Luik, J. N. H. Spoor, S. Malladi, H. Zandbergen, and C. Dekker, *Tailoring the hydrophobicity of graphene for its use as nanopores for DNA translocation,* Nature Communications **4**, 2619 (2013).

[68] S. J. Heerema and C. Dekker, *Graphene nanodevices for DNA sequencing,* Nature Nanotechnology **11**, 127 (2016).

[69] M. Graf, M. Lihter, D. Altus, S. Marion, and A. Radenovic, *Transverse Detection of DNA Using a MoS2 Nanopore,* Nano Letters **19**, 9075 (2019).

[70] M. Xiong, M. Graf, N. Athreya, A. Radenovic, and J.-P. Leburton, *Microscopic Detection Analysis of Single Molecules in MoS_2 Membrane Nanopores,* ACS Nano , 16131 (2020).

2

2

[71] D. V. Verschueren, S. Pud, X. Shi, L. De Angelis, L. Kuipers, and C. Dekker, *Label-Free Optical Detection of DNA Translocations through Plasmonic Nanopores,* ACS Nano **13**, 61 (2019).

[72] M. L. Juan, R. Gordon, Y. Pang, F. Eftekhari, and R. Quidant, *Self-induced back-action optical trapping of dielectric nanoparticles,* Nature Physics **5**, 915 (2009).

[73] A. Barik, L. M. Otto, D. Yoo, J. Jose, T. W. Johnson, and S.-H. Oh, *Dielectrophoresis-Enhanced Plasmonic Sensing with Gold Nanohole Arrays,* Nano Lett **14**, 2020 (2014).

[74] S. J. Yoon, J. Lee, S. Han, C. K. Kim, C. W. Ahn, M. K. Kim, and Y. H. Lee, *Non-fluorescent nanoscopic monitoring of a single trapped nanoparticle via nonlinear point sources,* Nature Communications **9**, 341401 (2018).

[75] C. Genet and T. W. Ebbesen, *Light in tiny holes, Nature,* **445**, 39 (2007).

[76] T. W. Ebbesen, H. J. Lezec, H. Ghaemi, T. Thio, and P. A. Wolff, *Extraordinary optical transmission through sub-wavelength hole arrays,* Nature **391**, 667 (1998).

[77] J. V. Coe, J. M. Heer, S. Teeters-Kennedy, H. Tian, and K. R. Rodriguez, *Extraordinary Transmission of Metal Films with Arrays of Subwavelength Holes,* Annual Review of Physical Chemistry **59**, 179 (2008).

[78] R. Gordon, *Biosensing with nanoaperture optical tweezers,* Optics & Laser Technology **109**, 328 (2019).

[79] P. Mestres, J. Berthelot, S. S. Acimovic, and R. Quidant, *Unraveling the optomechanical nature of plasmonic trapping,* Light: Science and Applications **5**, e16092 (2016).

[80] S. Aksu, A. A. Yanik, R. Adato, A. Artar, M. Huang, and H. Altug, *High-throughput nanofabrication of infrared plasmonic nanoantenna arrays for vibrational nanospectroscopy,* Nano Letters **10**, 2511 (2010).

[81] X. Shi, D. Verschueren, S. Pud, and C. Dekker, *Integrating Sub-3 nm Plasmonic Gaps into Solid-State Nanopores,* Small **14**, 1703307 (2018).

[82] M. K. Kim, H. Sim, S. J. Yoon, S. H. Gong, C. W. Ahn, Y. H. Cho, and Y. H. Lee, *Squeezing Photons into a Point-Like Space,* Nano Letters **15**, 4102 (2015).

[83] M. Righini, P. Ghenuche, S. Cherukulappurath, V. Myroshnychenko, F. J. De García Abajo, and R. Quidant, *Nano-optical trapping of rayleigh particles and Escherichia coli bacteria with resonant optical antennas,* Nano Letters **9**, 3387 (2009).

[84] Y. Pang and R. Gordon, *Optical trapping of a single protein,* Nano Letters **12**, 402 (2012).

[85] A. N. Koya, J. Cunha, T. Guo, A. Toma, D. Garoli, T. Wang, S. Juodkazis, D. Cojoc, and R. Proietti Zaccaria, *Novel Plasmonic Nanocavities for Optical TrappingAssisted Biosensing Applications,* Advanced Optical Materials **8**, 1901481 (2020).

[86] M. L. Juan, M. Righini, and R. Quidant, *plasmon nano-optical tweezers,* Nature Photonics **5**, 349 (2011).

[87] A. Kotnala and R. Gordon, *Double nanohole optical tweezers visualize protein p53 suppressing unzipping of single DNA-hairpins,* Biomedical Optics Express **5**, 1886 (2014).

[88] D. Verschueren, X. Shi, and C. Dekker, *Nano-Optical Tweezing of Single Proteins in Plasmonic Nanopores,* Small Methods **3**, 1800465 (2019).

[89] A. Zehtabi-Oskuie, H. Jiang, B. R. Cyr, D. W. Rennehan, A. A. Al-Balushi, and R. Gordon, *Double nanohole optical trapping: Dynamics and protein-antibody co-trapping,* Lab on a Chip **13**, 2563 (2013).

[90] X. Shi, D. V. Verschueren, and C. Dekker, *Active Delivery of Single DNA Molecules into a Plasmonic Nanopore for Label-Free Optical Sensing,* Nano Letters **18**, 8003 (2018).

[91] N. Hacohen, C. J. Ip, and R. Gordon, *Analysis of Egg White Protein Composition with Double Nanohole Optical Tweezers,* ACS Omega **3**, 5266 (2018).

[92] B. J. Roxworthy, A. M. Bhuiya, S. P. Vanka, and K. C. Toussaint, *Understanding and controlling plasmon-induced convection,* Nature Communications **5**, 1 (2014).

[93] E. Schäffet, S. F. Nørrelykke, and J. Howard, *Surface forces and drag coefficients of microspheres near a plane surface measured with optical tweezers,* Langmuir **23**, 3654 (2007).

[94] B. Malekian, K. Xiong, E. S. Kang, J. Andersson, G. Emilsson, M. Rommel, T. Sannomiya, M. P. Jonsson, and A. Dahlin, *Optical properties of plasmonic nanopore arrays prepared by electron beam and colloidal lithography,* Nanoscale Advances **1**, 4282 (2019).

[95] L. Pan, Y. Park, Y. Xiong, E. Ulin-Avila, Y. Wang, L. Zeng, S. Xiong, J. Rho, C. Sun, D. B. Bogy, and X. Zhang, *Maskless plasmonic lithography at 22 nm resolution,* Scientific Reports **1**, 1 (2011).

[96] K. Wang, E. Schonbrun, P. Steinvurzel, and K. B. Crozier, *Trapping and rotating nanoparticles using a plasmonic nano-tweezer with an integrated heat sink,* Nature Communications **2**, 1 (2011).

[97] H. J. Levene, J. Korlach, S. W. Turner, M. Foquet, H. G. Craighead, and W. W. Webb, *Zero-mode waveguides for single-molecule analysis at high concentrations,* Science **299**, 682 (2003).

[98] O. N. Assad, T. Gilboa, J. Spitzberg, M. Juhasz, E. Weinhold, and A. Meller, *Light-Enhancing Plasmonic-Nanopore Biosensor for Superior Single-Molecule Detection,* Advanced Materials **29**, 1605442 (2017).

[99] J. Larkin, R. Y. Henley, V. Jadhav, J. Korlach, and M. Wanunu, *Length-independent DNA packing into nanopore zero-mode waveguides for low-input DNA sequencing,* Nature Nanotechnology **12**, 1169 (2017).

[100] J. C. Ndukaife, A. V. Kildishev, A. George, A. Nnanna, V. M. Shalaev, S. T. Wereley, and A. Boltasseva, *Long-range and rapid transport of individual nano-objects by a hybrid electrothermoplasmonic nanotweezer,* Natue Nanotechnology **11** (2016).

[101] B. McNally, A. Singer, Z. Yu, Y. Sun, Z. Weng, and A. Meller, *Optical recognition of converted DNA nucleotides for single-molecule DNA sequencing using nanopore arrays,* Nano Letters **10**, 2237 (2010).

[102] B. N. Anderson, O. N. Assad, T. Gilboa, A. H. Squires, D. Bar, and A. Meller, *Probing solid-state nanopores with light for the detection of unlabeled analytes,* ACS Nano **8**, 11836 (2014).

[103] T. Gilboa and A. Meller, *Optical sensing and analyte manipulation in solid-state nanopores,* Analyst **140**, 4733 (2015).

[104] T. Gilboa, A. Zrehen, A. Girsault, and A. Meller, *Optically-Monitored Nanopore Fabrication Using a Focused Laser Beam,* Scientific Reports **8**, 1 (2018).

[105] T. Gilboa, E. Zvuloni, A. Zrehen, A. H. Squires, and A. Meller, *Automated, Ultra-Fast Laser-Drilling of Nanometer Scale Pores and Nanopore Arrays in Aqueous Solutions,* Advanced Functional Materials **30**, 1900642 (2020).

3

LITHOGRAPHY-BASED FABRICATION OF NANOPORE ARRAYS IN FREESTANDING SIN AND GRAPHENE MEMBRANES

We report a simple and scalable technique for the fabrication of nanopore arrays on free-standing SiN and graphene membranes based on electron-beam lithography and reactive ion etching. By controlling the dose of the single-shot electron-beam exposure, circular nanopores of any size down to 16 nm in diameter can be fabricated in both materials at high accuracy and precision. We demonstrate the sensing capabilities of these nanopores by translocating dsDNA through pores fabricated using this method, and find signal-to-noise characteristics on par with TEM-drilled nanopores. This versatile lithography-based approach allows for the high-throughput manufacturing of nanopores and can in principle be used on any substrate, in particular membranes made out of transferable 2D materials.

3.1. INTRODUCTION

Solid-state nanopores drilled in a thin membrane are unique tools that allow for label-free high-throughput single-molecule investigation of biomolecules such as DNA, proteins, and peptides chains [2]. Their robustness, versatility, and ease of integration in CMOS processing are paramount to the sustained interest this class of biosensors has received over the past 15 years [3]. The principle of interrogation for nanopore sensing derives elegance from its simplicity: a nanopore, typically drilled in a 20nm thick membrane, defines a nanoscale sensing volume through which biomolecules can be probed on passage, usually via an ionic-current readout [4]. More recently, nanopores in single-layer materials like graphene and MoS2 have received a great deal of attention, as the two-dimensional (2D) nature of these materials drastically reduces the sensing volume and helps to enhance the signal [5, 6]. Both SiN and 2D nanopores have been used to provide insight into many complex biophysical phenomena, such as DNA-protein interactions [5–9], protein-protein interactions [10], and DNA polymer physics [11, 12]. However nanopore fabrication is typically slow and expensive, particularly in 2D materials, preventing large-scale use of solid-state nanopores in commercial applications, such as clinical sensors for the detection of biomolecules in diagnostics [13, 14].

Currently, there are several techniques for the production of nanopores. First and foremost is the use of the electron beam of a Transmission Electron Microscope (TEM) [15]. This technique provides sub-nanometer precise control over the pore's diameter, but is very low in throughput, especially for larger sized nanopores (>15 nm) [16], very expensive, and labor intensive. A single nanopore takes at least 30 mins to be loaded into the TEM, aligned and sculpted to the desired size in a TEM by a trained operator. Furthermore, nanopores are notoriously hard to fabricate in 2D materials with conventional TEM drilling due to their sensitivity to carbon deposition and membrane damage [17]. Hence, the method lacks scalability and cost efficiency which are both required for commercialization. Fabrication using Helium Ion Microscope (HIM) is a promising, more high-throughput alternative for the fabrication of nanopores, but also requires access to expensive and delicate instrumentation [18, 19]. An alternative cost-effective technique is nanopore fabrication by controlled dielectric breakdown, where a nanopore is created by the timed termination of a large transmembrane voltage stress (~10V) [20, 21]. However, the stochastic nature of the breakdown process does not provide control over the position of the nanopore [22]. Other techniques use ion bombardment and subsequent chemical [23, 24] or electrochemical wet etching [25]. Whereas these techniques can be used at high throughput, challenges remain in the timed termination of the wet etching and the associated uniformity of the pore size.

Chemical dry etching or reactive ion etching (RIE) is a more promising alternative for high-throughput fabrication of large nanopores. In this widely used technique a pattern is predefined in a resist by electron-beam lithography (EBL), which is the standard technique used to define high-resolution structure in microfabrication, and is transferred into a substrate by plasma etching using reactive ions [26]. The directionality of the RIE process preserves the resolution obtained in the EBL pattern and allows for the resolution to be defined on a wafer scale [26–29]. The chemical dry etching allows a range of substrates to be used as membrane material [27], notably including 2D materials that require a transfer step. To exploit the potential of this technique for transferable materi-

als, the EBL patterning should be performed on a freestanding membrane. Furthermore, patterning on a thin membrane can improve resolution, because it eliminates electron backscatter [30].

Here, we present a novel and simple method for rapid nanopore fabrication based on electron-beam lithography with reactive ion etching. By patterning the nanopores as a last step in the fabrication process, in principle any (transferable) membrane material can be readily used. To demonstrate the flexibility of this technique, we create single nanopores and nanopore arrays in both 20 nm thick SiN and single-layer graphene membranes. TEM inspection shows that the fabricated nanopores are highly circular and uniform in size. We show that the nanopore diameter can be set with nanometer precision by controlling the electron-beam dose. Finally, we demonstrate lambda-DNA translocations through nanopores fabricated using this method. Although applied here for single-molecule biosensing, we anticipate that this simple, high-throughput, and versatile nanopore fabrication technique will find applications in other domains of the nanopore research field such as filtration, power generation and chemical sensing [5, 31, 32].

3.2. RESULTS AND DISCUSSION

Figure 3.1A outlines a schematic of the fabrication protocol for the production of a nanopore array in SiN. First, a layer a 100 nm thick layer of poly(methyl methacrylate) (PMMA-A3, 495K) electron sensitive resist (MicroChem Corp) is spin-coated on top of the chip containing a freestanding SiN membrane. Subsequently, the layer is patterned by exposing the resist with a 100 keV electron bundle from the electron-beam pattern generator (EBPG5200, Raith), using one single shot of e-beam exposure per nanopore. Details about the fabrication of the support and E-beam patterning can be found in the Supporting Information (SI3.4.1). After exposure, the PMMA is developed in a 1:3 mixture of methyl isobutyl ketone (MIBK) and isopropyl alcohol (IPA) for 1 min. Finally, the pattern is transferred into the SiN membrane by reactive ion etching with CHF3 (100 sec, 50 W, 50 sccm of CHF3, 2.5 sccm of O2, 8.6 μbar, Leybold) and the resist is stripped in hot acetone (50°C) for 2 hours.

The fabrication of the graphene nanopore array (Fig.3.1B) is analogous to the fabrication of the SiN nanopores. First, a layer of graphene (Graphenea, single layer CVD graphene on copper) is transferred onto a SiN membrane pre-patterned with square windows 1 μm in size, creating 1x1μm freestanding areas of graphene (see SI3.4.2). Then, a 150 nm thick layer of PMMA is spin-coated on top of the chip and the resist is exposed by a single shot from the electron beam. We note that thicker PMMA is used in the graphene nanopore arrays because the graphene requires an oxygen etch which also etches the PMMA mask substantially. After the development of the resist in 1:3 MIBK:IPA for one minute, the pattern is transferred into the graphene layer by reactive ion etching with oxygen (20 sec, 50 W, 20 sccm of O2, 3.3 μbar, Leybold). The remaining resist is stripped for 20 min in hot m-xylene (85°C) and air-dried. To avoid collapsing the freestanding graphene layer, the sample is gently plunged vertically into the solution. After 20 mins, the sample is removed and placed at an angle (20 degrees to the horizontal plane) to allow the remaining droplet of m-xylene to evaporate.

Figure 3.2 shows example TEM images of nanopore arrays fabricated in both SiN

3
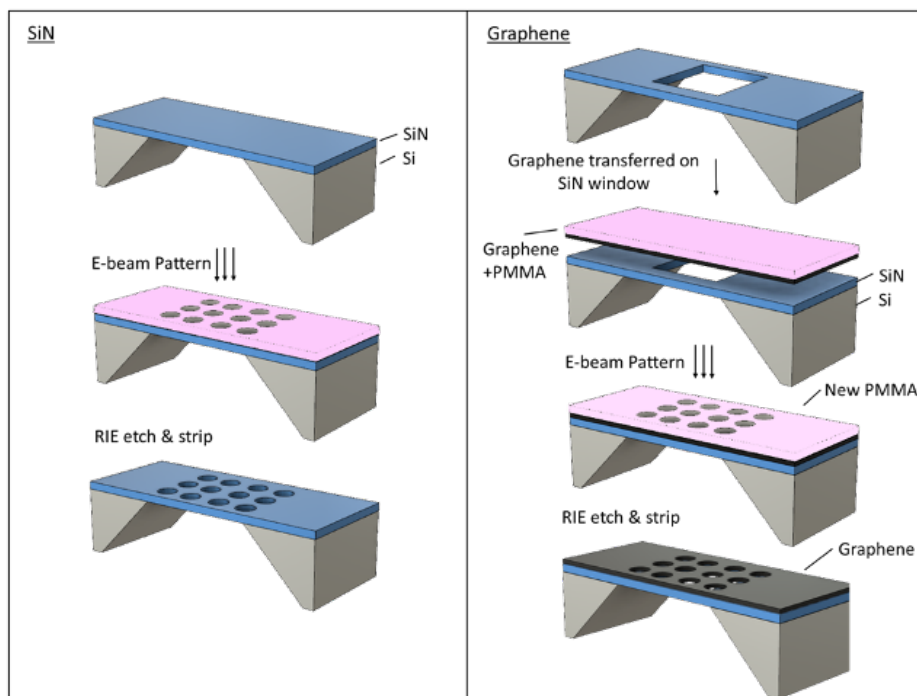
Figure 3.1: **Schematic of EBL assisted RIE nanopore fabrication.** A) Fabrication process on SiN membrane. A 100 nm thick layer of PMMA is spin-coated on a SiN membrane prior to e-beam patterning. The pattern is transferred into the SiN membrane by reactive ion etching in a CHF3 plasma. Finally, the remaining resist is stripped in hot acetone (50°C) leaving a functional nanopore array. B) The same process on the graphene membrane. A graphene layer with a supporting PMMA layer is deposited on a pre-etched SiN window. The supporting layer of PMMA is stripped and a new 150 nm of PMMA is deposited prior to e-beam patterning. The pattern is transferred into the graphene membrane by reactive ion etching in an oxygen plasma. Finally, the remaining resist is stripped in m-xylene, leaving a functional nanopore array.

(Fig. 3.2A) and in freestanding graphene (Fig. 3.2B) using the protocol outlined above. The nanopores in these examples were 29 ± 3 nm and 38 ± 2 nm (average ± standard deviation) in diameter, for the SiN and graphene respectively. The nanopores produced are highly circular; The average ratio between their major and minor axis (major/minor) is 1.08±0.08 for the SiN arrays and 1.08±0.14 for the graphene nanopore arrays. We note that the graphene pores fabricated through this method seem to exhibit much less carbon deposition around the edges of the pore than conventionally drilled TEM graphene pores [33].

By adjusting the electron dose used in the patterning, we are able to vary the size of the nanopores formed, as shown in Fig.3.3, where resulting diameter of the nanopore is plotted against the electron-beam dose used per shot of e-beam exposure, for both the SiN (Fig.3.3A) and graphene nanopores (Fig. 3.3 B). The smallest nanopore made was approximately 16±2 nm, both for SiN and graphene. Nanopores fabricated show similar variation in size (standard deviation is <10%) in both SiN and graphene. Because these
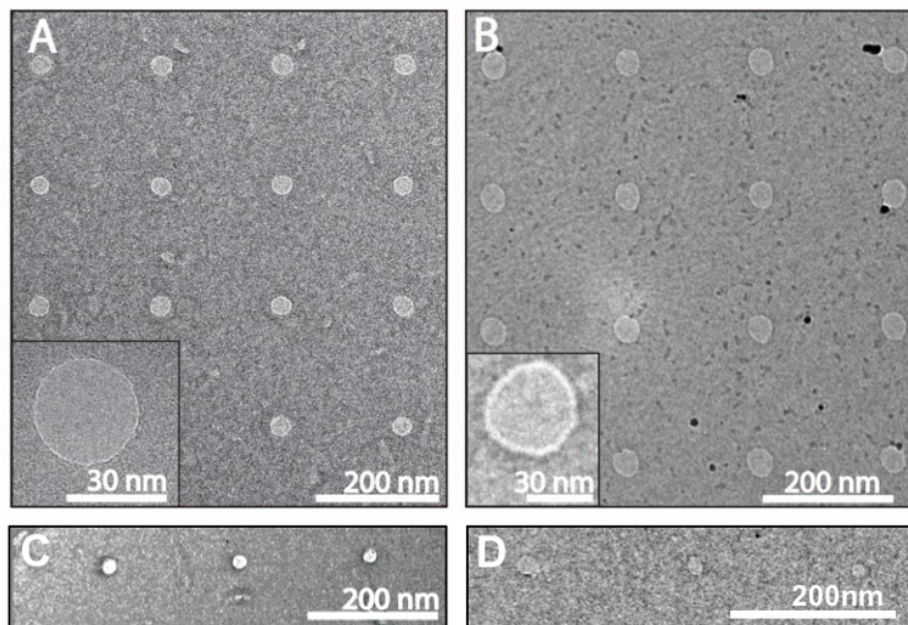
Figure 3.2: **TEM image of nanopore arrays fabricated using RIE.** A) Nanopore array fabricated in a SiN membrane. The array was fabricated using fabricated using a dose of 22 fC/shot, and the average pore diameter was 29±3 nm. B) Nanopore array fabricated in free-standing graphene. The array was fabricated using fabricated using a dose of 320 fC/shot, and the average pore diameter was 38±2 nm. The insets are zooms of a nanopore from each respective array, showing a circular nanopore. C) An array of 16±2 nm size pores in SiN. D) A dose test of nanopores on free-standing graphene. The nanopore diameters are, from left to right, 26nm, 19 nm, and 17 nm. More examples of nanopore arrays are attached in the Supporting Information.

values are similar and close to the size of the beamspot used (~15 nm), we speculate that the electron-beam spot size limits the resolution and hence it may be possible to fabricate smaller pores using a smaller spot size. By varying the electron-beam dose only, we obtained a range of nanopore sizes from 16 to >100 nm, though in principle even bigger sized pores can be produced by rasterizing a larger area with multiple shots of e⁻ beam exposure.

Interestingly, we find that the diameter of the resulting nanopore follows an empirical logarithmic relationship to the electron dose used for both SiN and graphene:

$$d = A * log(D) + B \tag{3.1}$$

where d is the nanopore diameter, D is the total electron dose, and A and B are fit parameters. A least-squares fit of Eqn. 3.1 to the red data points is plotted as a solid blue line in Fig. 3.3 and shows good agreement with the data (SiN: χ^2_{red}=2.8, graphene: χ^2_{red}=2.3). The specific values of the fit parameters A and B are not universal and will depend on experimental factors, such as the membrane material, resist thickness and the electron accelerating voltage. For instance, a higher dose is needed to create the same size of nanopores in free standing graphene as compared to SiN. A different dependence
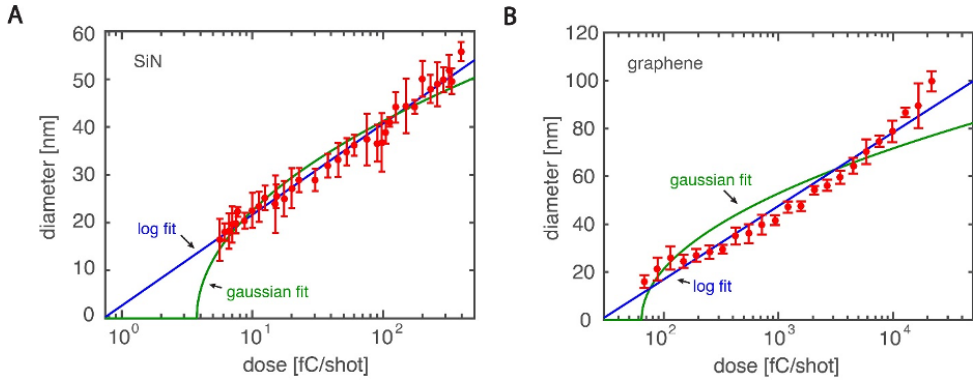
Figure 3.3: **Single-shot nanopore diameter versus electron-beam dose.** The solid blue line is an empirical logarithmic fit (A-SIN: χ^2_{red} = 2.8 B- Graphene : χ^2_{red}=2.3), the green curve is a fit assuming a Gaussian dependence of dose on diameter (A-SiN: χ^2_{red}=7.2, B-Graphene: χ^2_{red}=10.8). Error bars are the standard deviation, χ^2_{red} values are calculated using the standard error of the mean for each datapoint.

results if patterning is performed on a thick substrate since electron backscatter from the substrate will be the dominant contribution to the exposure [29]. The agreement between the data and relationship is somewhat surprising as a more complex dependence is expected if one assumes that the nanopore size is merely set by the point spread function (PSF) of the electron beam [30]. This dependency can be modelled by assuming the resist only develops after receiving a local electron dose per unit area $\tilde{D}$ larger than some threshold value of the dose D_T. Using a Gaussian PSF to describe the electron beam profile ($D(r) \propto De^{(-\gamma r^2)}$, where r is the distance from the center of the electron beam, D is the total dose, and γ is a fit parameter) and setting D_T= ~D(d), a dependency of the diameter on the total dose can be extracted. This dependency is plotted as a green line in Fig. 3.3 and does not explain the trend well. Only moderate agreement between data (SiN χ^2_{red}=7.2, graphene: χ^2_{red}=10.8) is obtained. Hence the phenomenological model in equation 3.1 should be used to determine the correct size of the nanopore from the dose.

One might wonder if the use of PMMA as a resist will set a maximum size for the nanopore size that can be fabricated, as it is known that PMMA will behave as a negative-tone resist at high doses [34] (>100fC). This is however not the case, as at high-dose exposure, the resist in the tail of the beam will still be exposed to a low dose. This leads to a donut-shaped cut in the resist after development which will create a hole in the membrane after pattern transfer by RIE. Moreover, standard resist patterning (rastering) can be used for nanopores larger than 50 nm in diameter or for large nanopores of different shapes.

To show that the SiN and graphene nanopores created using this method can be used for the detection of DNA, we performed double-stranded DNA (lambda-DNA, 48.5kbp) translocation experiments on these nanopores. A schematic of a typical nanopore experiment is shown in Fig. 3.4A, where DNA molecules added to the negatively-biased cis compartment of the flow cell are electrophoretically driven through the nanopore and
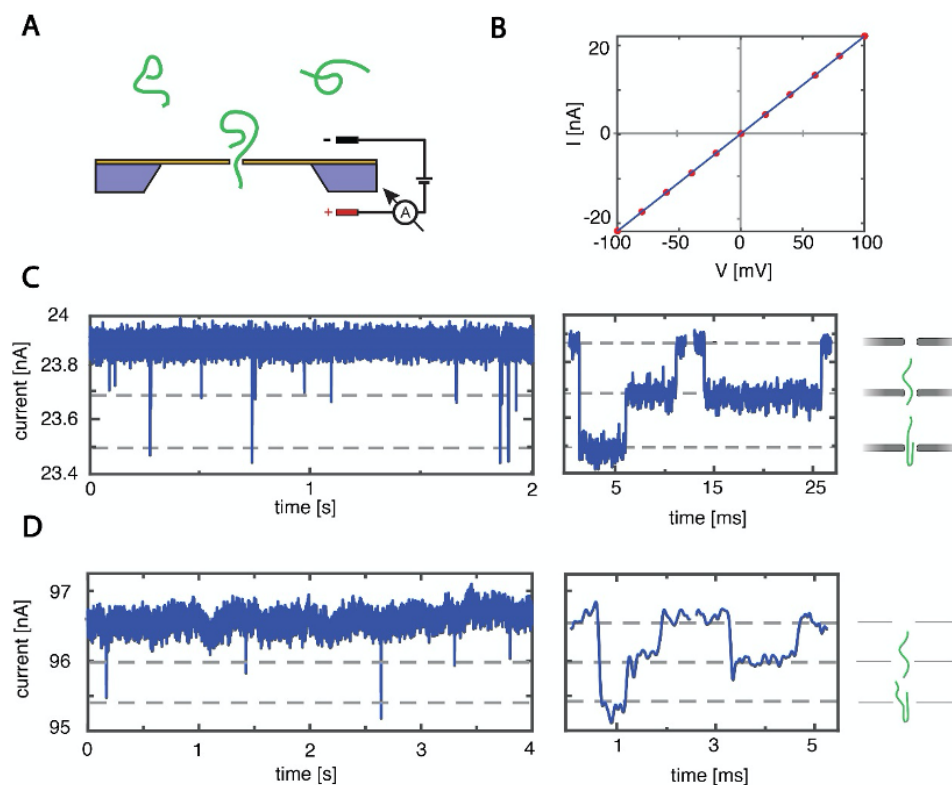
Figure 3.4: **DNA translocations through RIE-fabricated SiN and graphene nanopores.** (A) Schematic illustration of a DNA translocation experiment. (B) IV-curve of a 25 nm SiN nanopore with a resistance of 4.5 MΩ, with the corresponding linear fit. (C) Left: Current time trace through a SiN nanopore of 25 nm (4.5 MΩ). Data was taken at 100 mV in 2M LiCl and low-pass filtered at 10 kHz. Right: zooms of DNA translocations, showing a folded and a linear translocation. (D) Left: Current time trace through a graphene nanopore of 18 nm (4.0 MΩ). Data was taken at 500 mV in 2M LiCl and low-pass filtered at 5 kHz. The large driving voltage was used to enhance the DNA translocation rate. Right: zooms of DNA translocations, showing a folded and a linear translocation.

detected by a change in ionic current through the pore. Fig. 3.4B shows examples of DNA translocations through a 18 nm graphene nanopore, fabricated using a dose of 88 fC, and a 25 nm SiN nanopore, fabricated using a dose of 15 fC. DNA translocation experiments were done in a PEEK (Polyether ether ketone) flow cell in 2M LiCl (buffered with 20mM Tris-Cl, 2mM EDTA, pH 8) and we used Ag/AgCl electrodes and an Axopatch 200B amplifier (Molecular Devices) for current detection. To wet the graphene nanopore, we incubated the chip in the flow cell with a mixture of equal parts ethanol and water for 30 min.

Figure 3.4B shows the linear I-V curve of the SiN nanopore with a resistance of 4.5 MΩ. This compares well with the expected resistance of 3.9 MΩ for a 25 nm nanopore, calculated using a measured buffer conductivity of 13.8 nS/m and an effective membrane thickness of 6.7 nm. After adding lambda-DNA to the cis chamber at a concentra-

tion of 10 ng/μL, transient current blockades could be clearly discerned, as shown in the first panel of Fig. 3.4C. The translocations show excellent signal-to-noise characteristics, illustrated by the zooms in the right panel of Fig. 3.4C of two such DNA translocations, one molecule translocating in a linear fashion (right) and one in a folded conformation (left). The double-strand DNA conductance blockade of 1.8 nS (N = 580) matches the expected value of 1.8 nS well. The normalized current power spectral density can be found in the SI.

Fig. 3.4D shows example DNA translocations through a 18 nm graphene nanopore. The nanopore had a resistance of 4.9 MΩ, which agrees reasonably well with the expected 4.2 MΩ using an effective membrane thickness of 0.6 nm [35, 36]. We used a high driving voltage of 500 mV, to enhance the low capture rates often observed in bare graphene nanopores [37]. The current time trace shows considerable low-frequency current noise, similar to what was observed for TEM-drilled graphene nanopores [35] (see SI3.4.5). Analysis of all detected events at 500 mV (N = 59) show a blockade levels of 1.0 nS [38]. This is markedly lower than the theoretically expected blockade of 5.6 nS from a dsDNA strand in a 18 nm graphene nanopore [39], but the discrepancy is consistent with previous work on TEM-drilled graphene nanopores which gave values of 1.5 nS for similar sized pores [33]. Graphene nanopores drilled using this RIE based method suffer from the same challenges as graphene nanopores drilled using TEM such as low fabrication yield. These challenges include limited statistics and current-signal resolving power caused by graphene-DNA interactions and high 1/f noise [35, 40]. Overall about 10% of the graphene devices showed successful DNA translocation events compared to over 50% in SiN devices. Fortunately, these issues can be mitigated by reducing the freestanding area and using a molecular coating of the graphene [37]. Summarizing, these nanopores created using EBL with RIE show sensing characteristics that are on par with their TEM-drilled counterparts.

3.3. CONCLUSIONS

In conclusion, we have developed a facile method for rapid, flexible, and large-scale nanopore manufacturing in freestanding SiN and graphene membranes using electron-beam lithography with reactive ion etching which are very commonly available fabrication techniques. As the nanopore is created in the final step of the fabrication, our approach is extremely versatile and can in principle by used on any substrate, in particular 2D materials that require a transfer step. By adjusting the electron-beam dose, the diameter of the nanopore can accurately be controlled with a high-level of uniformity and precision. Furthermore, we demonstrate that the nanopores fabricated with this method show single-molecule sensing performances equivalent to their TEM drilled predecessors. The ease of the method allows for patterning large intact areas of freestanding 2D materials like graphene with a clearly defined array of nanopores. We expect that this technique will also find a range of applications beyond mere nanopore sensing, such as filtration with nano-sieves.

3.4. Supporting Information

3.4.1. Fabrication of SiN membrane supports with a $1 \times 1 \mu$m square and E beam patterning details

The silicon-nitride chips are fabricated using similar protocol as published in Janssen et al [41] to obtain 20 nm thick freestanding SiN membranes of 40 by 40 μm wide. The top layers on the substrate are removed to create a flat SiN surface extending over the chip. Subsequently squares are etched in the SiN membrane which defined the area of freestanding graphene, in a similar procedure to making the nanopore arrays in SiN. For this, the chips are spincoated with a 100 nm thick layer of poly(methyl methacrylate) (PMMA, 495K) electron sensitive resist (MicroChem Corp). Then, the layer is patterned by exposing the resist with a 100 keV electron bundle from the electron-beam pattern generator (EBPG5200, Raith). Depending on the experiment, either a single square or an array of squares is patterned. For the dose test, we patterned an array of squares (1 by 1 μm). After exposure, the PMMA is developed in a 1:3 mixture of methyl isobutyl ketone (MIBK) and isopropyl alcohol (IPA) for 1 min. The pattern is transferred into the SiN by reactive ion etching (1 min 40 sec, 50 W, 50 sccm CHF3 and 2.5 sccm O2, 8.5 μbar, Leybold). The remaining resist is stripped using hot acetone (50°C) for 20 mins. For the nanopore experiments, a single 100 by 100 nm wide square is etched to define the freestanding graphene area.

Electron-beam patterns are created in Layout-BEAMER (GenISys) from a gds file, where each nanopore is designed as a single 2x2nm pixel size. The beam step size is set equal to the pixel size to ensure a single exposure per pixel and a mainfield size of 520 by 520 μm is used. The pattern is subsequently imported into CJOB to generate a file compatible to the electron-beam pattern generator. Here an area dose is set and a beam is selected from a predefined list on the machine. The beam current used is 512pA at an aperture size of 300um. We note that using a different optimization marker on the sample holder did not reduce the optimized beam size of 16nm. The dose per shot is calculated by multiplying the area dose by the beam step size.

3.4.2. Graphene Transfer Process

A supporting layer of 150 nm of PMMA is spin coated onto CVD graphene on copper (bought from Graphenea). The copper is etched away in a solution of 0.1M ammonium persulfate ((NH4)2S2O8, 5g/100 ml). After 10 mins, the underside of the graphene-copper substrate is rinsed to strip the bottom layer of graphene. This is important to reduce the formation of graphene wrinkles. Subsequently, the graphene-copper substrate is placed back into the etching solution to fully etch the copper. The freely floating graphene-PMMA sample is scooped up by a clean glass slide and transferred into a beaker of clean deionized water. The sample was transferred to a second clean beaker of deionised water to completely remove all ammonium persulfate residues. In the final step, the graphene-PMMA sample is scooped up by the silicon nitride wafer sample (pre-etched with the freestanding window) and allowed to dry at an angle overnight. Finally, the PMMA is stripped by using a solution of hot acetone (45 °C) or hot xylene (85 °C) and the sample is ready for the patterning step.

3.4.3. TEM IMAGES OF GRAPHENE NANOPORE ARRAY
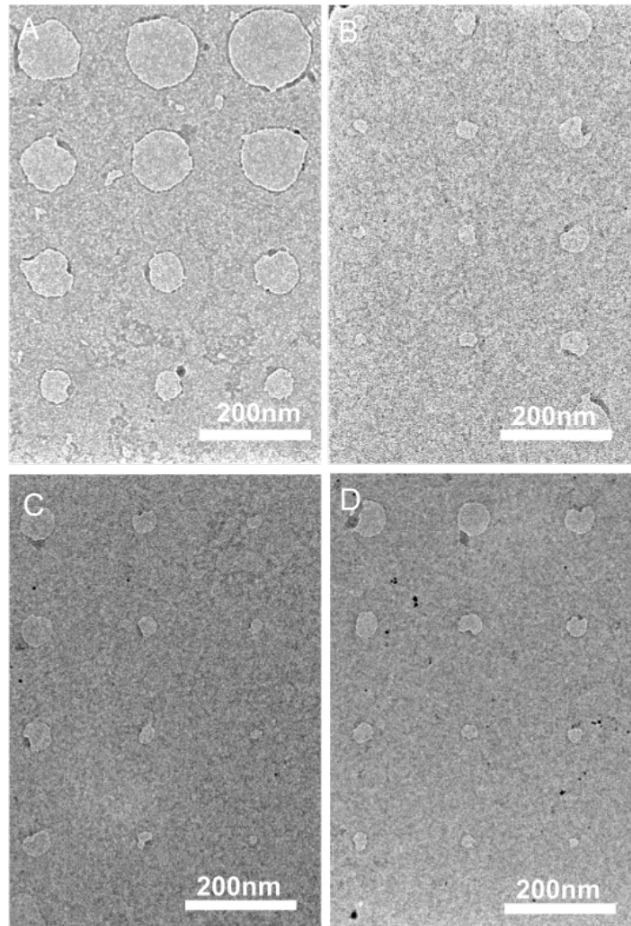
Figure 3.5: **Example TEM images of a nanopore arrays fabricated using RIE on graphene.** The electron dose was varied to produce different sized holes. A) Graphene nanopore array with diameters ranging from 140 nm to 67 nm. B-D) Graphene nanopore array with diameters ranging from (B) 69 nm to 23 nm, (C) 62 nm to 17 nm (D) 53 nm to 18 nm. The variance in size of hole produced at each of the respective dose is reported in the main text.

3.4.4. TEM IMAGES OF GRAPHENE NANOPORE ARRAY
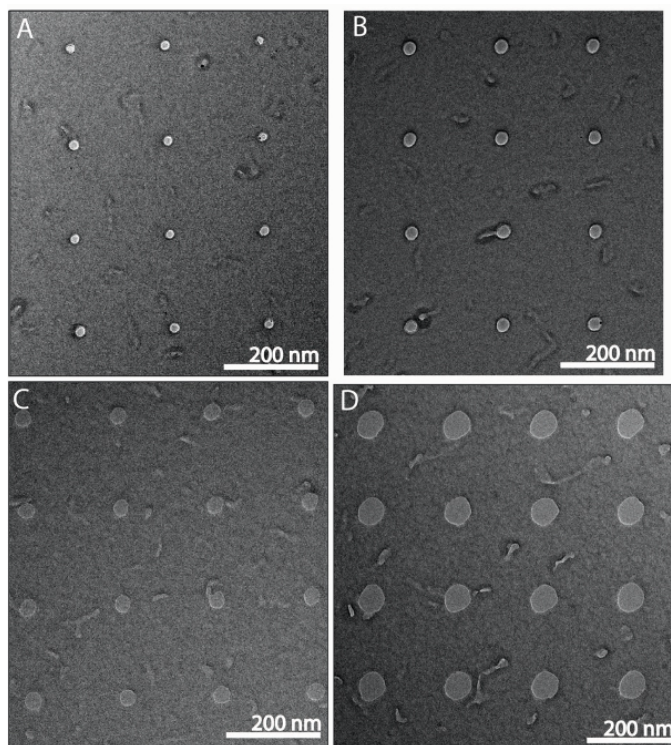
Figure 3.6: **Example TEM images of a nanopore arrays fabricated using RIE in SiN.** (A) Nanopore array with an average diameter of 16±2 nm. (B) Nanopore array with an average diameter of 26±2 nm. (C) Nanopore array with an average diameter of 35±3 nm. (D) Nanopore array with 62±2nm.

3.4.5. NOISE SPECTRUM OF RIE FABRICATED GRAPHENE NANOPORE
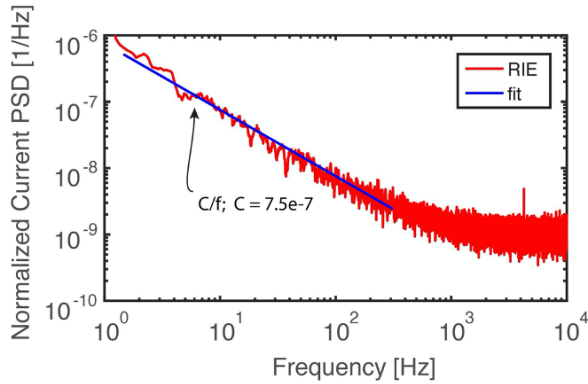
Figure 3.7: **Noise spectrum of graphene nanopore** Normalized current power spectral density (PSD) (S_I/I^2) of a 18 nm graphene nanopore fabricated using RIE using a dose of 88fC and a fit to flicker noise contribution (S_I/I^2)=C/f,), where f is the frequency and C is low-frequency noise amplitude. The fit shows a value for the low-frequency noise amplitude of $7.5*10^{-7}$, which is similar to values obtained from graphene nanopores drilled with the TEM (10^{-6}) [35]. The PSDs are smoothened using a 20 point moving average.

3.4.6. NOISE SPECTRUM OF RIE FABRICATED SIN NANOPORE
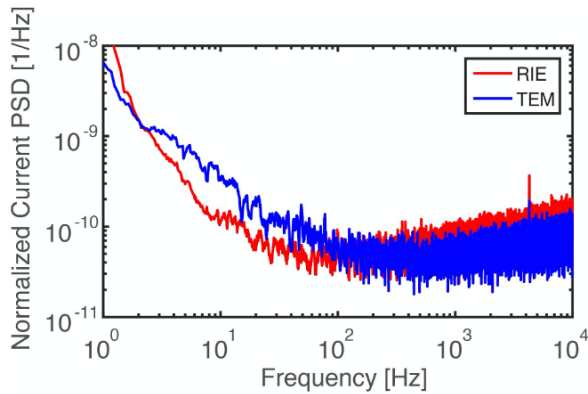
Figure 3.8: **Noise spectrum of SiN nanopore** Normalized current power spectral density (PSD) (S_I/I^2) of a 25 nm SiN nanopore fabricated using RIE with a dose of 15fC and a 20 nm nanopore created using TEM drilling. The low frequency component of the noise (< 1kHz) is comparable between TEM drilled and RIE fabricated nanopores. The PSDs are smoothened using a 20-point moving average.

REFERENCES

[1] D. V. Verschueren, W. Yang, and C. Dekker, *Lithography-based fabrication of nanopore arrays in freestanding SiN and graphene membranes,* Nanotechnology **29**, 145302 (2018).

[2] H. Arjmandi-Tash, L. A. Belyaeva, and G. F. Schneider, *Single molecule detection with graphene and other two-dimensional materials: Nanopores and beyond,* Chemical Society Reviews **45**, 476 (2016).

[3] B. N. Miles, A. P. Ivanov, K. A. Wilson, F. Dogan, D. Japrung, and J. B. Edel, *Single molecule sensing with solid-state nanopores: Novel materials, methods, and applications,* Chemical Society Reviews **42**, 15 (2013).

[4] M. Wanunu, *Nanopores: A journey towards DNA sequencing,* Physics of Life Reviews **9**, 125 (2012).

[5] J. Feng, M. Graf, K. Liu, D. Ovchinnikov, D. Dumcenco, M. Heiranian, V. Nandigana, N. R. Aluru, A. Kis, and A. Radenovic, *Single-layer MoS2 nanopores as nanopower generators,* Nature **536**, 197 (2016).

[6] S. J. Heerema and C. Dekker, *Graphene nanodevices for DNA sequencing,* Nature Nanotechnology **11**, 127 (2016).

[7] J. Chen, C. Li, and G. Shi, *Graphene materials for electrochemical capacitors,* Journal of Physical Chemistry Letters **4**, 1244 (2013).

[8] D. E. Jiang, V. R. Cooper, and S. Dai, *Porous graphene as the ultimate membrane for gas separation,* Nano Letters **9**, 4019 (2009).

[9] C. Raillon, P. Cousin, F. Traversi, E. Garcia-Cordero, N. Hernandez, and A. Radenovic, *Nanopore detection of single molecule RNAP-DNA transcription complex,* Nano Letters **12**, 1157 (2012).

[10] G. Goyal, Y. B. Lee, A. Darvish, C. W. Ahn, and M. J. Kim, *Hydrophilic and size-controlled graphene nanopores for protein detection,* Nanotechnology **27** (2016).

[11] M. M. Marshall, J. Ruzicka, O. K. Zahid, V. C. Henrich, E. W. Taylor, and A. R. Hall, *Nanopore analysis of single-stranded binding protein interactions with DNA,* Langmuir **31**, 4582 (2015).

[12] D. Japrung, A. Bahrami, A. Nadzeyka, L. Peto, S. Bauerdick, J. B. Edel, and T. Albrecht, *SSB binding to single-stranded DNA probed using solid-state nanopore sensors,* Journal of Physical Chemistry B **118**, 11605 (2014).

[13] K. Chen, M. Juhasz, F. Gularek, E. Weinhold, Y. Tian, U. F. Keyser, and N. A. Bell, *Ionic Current-Based Mapping of Short Sequence Motifs in Single DNA Molecules Using Solid-State Nanopores,* Nano Letters **17**, 5199 (2017).

[14] J. Y. Sze, A. P. Ivanov, A. E. Cass, and J. B. Edel, *Single molecule multiplexed nanopore protein screening in human serum using aptamer modified DNA carriers,* Nature Communications **8** (2017).

[15] M. J. Kim, M. Wanunu, D. C. Bell, and A. Meller, *Rapid fabrication of uniformly sized nanopores and nanopore arrays for parallel DNA analysis,* Advanced Materials **18**, 3149 (2006).

[16] T. Deng, M. Li, Y. Wang, and Z. Liu, *Development of solid-state nanopore fabrication technologies,* Vol. 60 (Science in China Press, 2015) pp. 304–319.

[17] Q. Xu, M. Y. Wu, G. F. Schneider, L. Houben, S. K. Malladi, C. Dekker, E. Yucelen, R. E. Dunin-Borkowski, and H. W. Zandbergen, *Controllable atomic scale patterning of freestanding monolayer graphene at elevated temperature,* ACS Nano **7**, 1566 (2013).

[18] J. Yang, D. C. Ferranti, L. A. Stern, C. A. Sanford, J. Huang, Z. Ren, L. C. Qin, and A. R. Hall, *Rapid and precise scanning helium ion microscope milling of solid-state nanopores for biomolecule detection,* Nanotechnology **22** (2011).

[19] Y. Deng, Q. Huang, Y. Zhao, D. Zhou, C. Ying, and D. Wang, *Precise fabrication of a 5 nm graphene nanopore with a helium ion microscope for biomolecule detection,* Nanotechnology **28**, 045302 (2016).

[20] H. Kwok, K. Briggs, and V. Tabard-Cossa, *Nanopore fabrication by controlled dielectric breakdown,* PLoS ONE **9** (2014).

[21] A. T. Kuan, B. Lu, P. Xie, T. Szalay, and J. A. Golovchenko, *Electrical pulse fabrication of graphene nanopores in electrolyte solution,* Applied Physics Letters **106** (2015).

[22] A. Zrehen, T. Gilboa, and A. Meller, *Real-time visualization and sub-diffraction limit localization of nanometer-scale pore formation by dielectric breakdown,* Nanoscale **9**, 16437 (2017).

[23] S. R. Park, H. Peng, and X. S. Ling, *Fabrication of nanopores in silicon chips using feedback chemical etching,* Small **3**, 116 (2007).

[24] T. Deng, J. Chen, C. N. Wu, and Z. W. Liu, *Fabrication of Inverted-Pyramid Silicon Nanopore Arrays with Three-Step Wet Etching,* ECS Journal of Solid State Science and Technology **2**, P419 (2013).

[25] K. Yasuda, A. Ghicov, T. Nohira, N. Kani, R. Hagiwara, and P. Schmuki, *Preparation of organized Ti nanorods by successive electrochemical processes in aqueous solution and molten salt,* Electrochemical and Solid-State Letters **11** (2008).

[26] A. Han, M. Creus, G. Schürmann, V. Linder, T. R. Ward, N. F. De Rooij, and U. Staufer, *Label-free detection of single protein molecules and protein-protein interactions using synthetic nanopores,* Analytical Chemistry **80**, 4651 (2008).

[27] J. Bai, D. Wang, S. W. Nam, H. Peng, R. Bruce, L. Gignac, M. Brink, E. Kratschmer, S. Rossnagel, P. Waggoner, K. Reuter, C. Wang, Y. Astier, V. Balagurusamy, B. Luan, Y. Kwark, E. Joseph, M. Guillorn, S. Polonsky, A. Royyuru, S. Papa Rao, and G. Stolovitzky, *Fabrication of sub-20 nm nanopore arrays in membranes with embedded metal electrodes at wafer scales,* Nanoscale **6**, 8900 (2014).

[28] A. G. Ahmadi and S. Nair, *Geometry of nanopore devices fabricated by electron beam lithography: Simulations and experimental comparisons,* Microelectronic Engineering **112**, 149 (2013).

[29] R. Wei, D. Pedone, A. Zürner, M. Döblinger, and U. Rant, *Fabrication of metallized nanopores in silicon nitride membranes for single-molecule sensing,* Small **6**, 1406 (2010).

[30] I. Adesida, T. E. Everhart, and R. Shimizu, *High resolution electron-beam lithography on thin films,* Journal of vacuum science & technology **16**, 1743 (1979).

[31] A. Aghigh, V. Alizadeh, H. Y. Wong, M. S. Islam, N. Amin, and M. Zaman, *Recent advances in utilization of graphene for filtration and desalination of water: a review,* Desalination **365**, 389 (2015).

[32] S. Howorka and Z. Siwy, *Nanopore analytics: Sensing of single molecules,* Chemical Society Reviews **38**, 2360 (2009).

[33] G. F. Schneider, S. W. Kowalczyk, V. E. Calado, G. Pandraud, H. W. Zandbergen, L. M. Vandersypen, and C. Dekker, *DNA translocation through graphene nanopores,* Nano Letters **10**, 3163 (2010).

[34] H. Duan, D. Winston, J. K. W. Yang, B. M. Cord, V. R. Manfrinato, and K. K. Berggren, *Sub-10-nm half-pitch electron-beam lithography by using poly(methyl methacrylate) as a negative resist,* Journal of Vacuum Science & Technology B **28**, C6C58 (2010).

[35] S. Heerema, G. Schneider, M. Rozemuller, L. Vicarelli, H. Zandbergen, and C. Dekker, *1/f noise in graphene nanopores,* Nanotechnology **26**, 074001 (2015).

[36] R. C. Rollings, A. T. Kuan, and J. A. Golovchenko, *Ion selectivity of graphene nanopores,* Nature Communications **7** (2016).

[37] G. F. Schneider, Q. Xu, S. Hage, S. Luik, J. N. Spoor, S. Malladi, H. Zandbergen, and C. Dekker, *Tailoring the hydrophobicity of graphene for its use as nanopores for DNA translocation,* Nature Communications **4** (2013).

[38] C. Plesa and C. Dekker, *Data analysis methods for solid-state nanopores,* Nanotechnology **26**, 084003 (2015).

[39] A. T. Carlsen, O. K. Zahid, J. Ruzicka, E. W. Taylor, and A. R. Hall, *Interpreting the conductance blockades of DNA translocations through solid-state nanopores,* ACS Nano **8**, 4754 (2014).

[40] Y. Kabiri, A. N. Ananth, J. van der Torre, A. Katan, J. Y. Hong, S. Malladi, J. Kong, H. Zandbergen, and C. Dekker, *Distortion of DNA Origami on Graphene Imaged with Advanced TEM Techniques,* Small **13** (2017).

[41] X. J. Janssen, M. P. Jonsson, C. Plesa, G. V. Soni, C. Dekker, and N. H. Dekker, *Rapid manufacturing of low-noise membranes for nanopore sensors by trans-chip illumination lithography,* Nanotechnology **23**, 475302 (2012).

3

4

DETECTION OF CRISPR-DCAS9 ON DNA WITH SOLID-STATE NANOPORES

Solid-state nanopores have emerged as promising platforms for biosensing including diagnostics for disease detection. Here we show nanopore experiments that detect CRISPR-dCas9, a sequence-specific RNA-guided protein system that specifically binds to a target DNA sequence. While CRISPR-Cas9 is acclaimed for its gene editing potential, the CRISPR-dCas9 variant employed here does not cut DNA but instead remains tightly bound at a user-defined binding site, thus providing an excellent target for biosensing. In our nanopore experiments, we observe the CRISPR-dCas9 proteins as local spikes that appear on top of the ionic current blockade signal of DNA molecules that translocate through the nanopore. The proteins exhibit a pronounced blockade signal that allows for facile identification of the targeted sequence. Even at the high salt conditions (1M LiCl) required for nanopore experiments, dCas9 proteins are found to remain stably bound. The binding position of the target sequence can be read from the spike position along the DNA signal. We anticipate applications of this nanopore-based CRISPR-dCas9 biosensing approach in DNA-typing based diagnostics such as quick disease-strain identification, antibiotic-resistance detection, and genome typing.

4.1. Introduction

While nanopores are most well-known for their use in biophysics experiments and DNA sequencing [2], they also hold great promise as diagnostic sensing devices, due to their high sensitivity, simple readout, ease of device fabrication, and their ability to detect individual disease-related biomarkers. A solid-state nanopore is a nanometer-sized hole that is etched in a thin membrane such as silicon nitride (SiN). Upon application of a voltage across the nanopore in an electrolyte solution, biomolecules such as DNA will translocate through the pore, thus temporarily blocking the passage of ions that leads to a drop in the current, which constitutes the basic sensing signal. This simple and elegant principle enables an easy readout and interpretation of the nanopore signal. Solid-state nanopores feature a number of additional advantages for developing biosensors such as their robustness, sensitivity, versatility, and compatibility with CMOS fabrication processes [3]. Indeed, in recent years, solid-state nanopores have been applied to study protein–DNA interactions with proteins such as nucleosomes [4] or antibodies [5] and for protein-sensing applications of medically relevant proteins such as thrombin [6]. The larger hydrodynamic radius of these protein–DNA complexes gives rise to a larger blockade current signal as they transverse the pore. These studies have suggested a genome-mapping type of approach through the monitoring of sequence-specific proteins [7]. However, such an approach has remained challenging because suitable strong-DNA-binding proteins are rare due to the high salt concentrations that are required for decent signals in nanopore experiments.

Here we employ the CRISPR-dCas9 protein system for the detection of DNA motifs. In recent years, Clustered Regularly Interspaced Short Palindromic Repeats (CRISPR) and its CRISPR-associated (Cas) proteins have gained enormous attention for its unprecedented potential as a gene-editing tool. The Cas9 protein is able to bind to a target DNA sequence through a guide RNA (gRNA) [8]. This gRNA is easily programmable, allowing Cas9 to target any DNA sequence, including DNA motifs that uniquely identify a variety of disease-DNA [9]. The CRISPR-Cas9 protein has been shown to be sensitive to even single nucleotide mismatches and has a large hydrodynamic diameter (~7 nm) [10, 11]. The Cas9 protein can be modified to remove its endonuclease activity (i.e. cleaving activity) while keeping its programmable DNA-binding activity intact [12]. This Cas9 variant, known as dCas9, is favorable to be repurposed as a DNA detection tool in the nanopore detection scheme proposed here.

In this work, we demonstrate a solid-state nanopore-based detection scheme for probing DNA motifs using CRISPR-dCas9 (Fig. 4.1). Target RNA is preincubated with dCas9 and then mixed with the DNA sample of interest (see Methods). Next, the DNA with bound CRISPR-dCas9 is driven through the solid-state nanopore where the dCas9 protein gives rise to a pronounced feature on top of the DNA signal which allows for facile identification of specific DNA motifs (Fig.4.1B,C). We demonstrate stable binding of dCas9 to DNA, even in the high salt concentrations of the nanopore buffer. The high salt concentration and the large hydrodynamic radius of the dCas9 boost the nanopore signal and allow for identification of the targeted sequence in easily fabricated large-diameter solid-state nanopores. The binding position of dCas9 along the DNA can be determined from the spike position along each nanopore event. We anticipate applications of the CRISPR-dCas9 detection scheme in DNA-typing diagnostics with solid-state
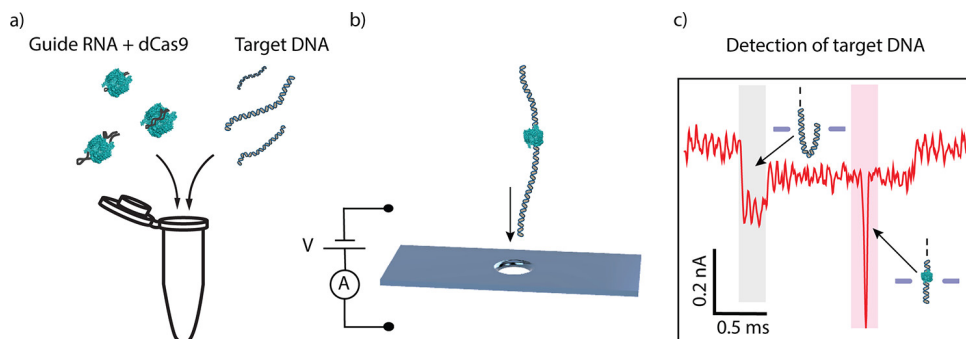
Figure 4.1: **dCas9-DNA nanopore detection scheme.** A) gRNA is preincubated with dCas9 (labeled in green; not to scale) and then incubated to form a complex with target DNA prior to nanopore detection. B) Voltage applied across the membrane induces an ionic current through a 20 nm size nanopore aperture and drives dCas9-DNA complexes to translocate through the nanopore. C) The dCas9 signal appears as an additional blockade event (the sharp spike in the red shaded region) on top of the single-molecule DNA ionic-current signature which shows a constant current blockade except for the start of the event (gray shaded area) where DNA enters the pore in a folded manner [13]

.

nanopores such as quick disease strain identification, antibiotic resistance detection, and genome typing.

4.2. Results and Discussion

CRISPR-dCas9 is found to stably bind to DNA even at the high salt concentrations that are favored for nanopore experiments. Figure 4.2a shows a clear shift of the band of the dCas9-DNA complex with respect to the DNA control bands in both the Cas9 reaction buffer and 1 M LiCl conditions. Notably most of the DNA gets bound by dCas9, even in the 1 M LiCl condition. The experiment also shows that dCas9 can remain bound over the ~2.5 h course of the gel experiment. Note that the bands in the 1 M LiCl condition did not run to the same position as the Cas9 reaction buffer because of electrostatic screening in the high-salt conditions. Gel experiments for the full range of salt concentrations from 0.5 M LiCl to 4 M LiCl can be found in the Supporting Information (see SI4.6).

DNA translocation events in nanopore experiments clearly show the signatures of CRISPR-dCas9 binding. Upon addition of a control sample with bare DNA to the flow cell with a 20 nm SiN nanopore, we observe the typical current trace signals (Figure 4.2b), namely, a ~2ms long partial blockade of the ionic current with a blockade current of I_o= 0.12 nA, often starting with a double-blockade current of $2I_o$ at the start of the current trace that can be attributed to the capture and translocation of a folded ds-DNA at the start of the event [13]. Notably, the nanopore events for the CRISPR-dCas9-incubated sample look exactly the same except for the fact that they contain a single sharp spikelike feature on top of the DNA current signature; see Figure 4.2 c. We attribute these spikes along the DNA blockade to the presence of the locally bound dCas9 protein. The localized spikes have a short duration (~25–60 μs) and a much deeper blockade level (up to 1.5 nA) than the bare dsDNA. Such a large signal is also expected since the dCas9 protein
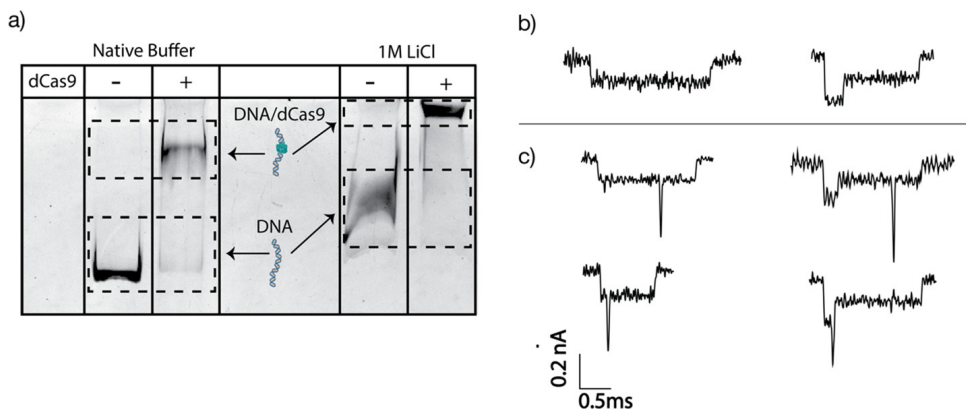
Figure 4.2: **Stability of dCas9 on DNA at high salt and examples of nanopore current traces.** A) Gel shift assay showing binding of dCas9 in 1 M LiCl nanopore buffer. A clear shift in the DNA band at 1 M LiCl indicates that the dCas9 remains bound on the DNA even at high salt concentrations. The plus (+) sign indicates 1 kbp DNA samples that were incubated with the dCas9 complex. B) Examples of nanopore current traces for a 20 kb long dsDNA-only control sample. The left trace shows a type 1 event, where the DNA translocated in a linear head-to-tail fashion, while the right trace shows a type 2–1 event, where there is a fold at the start of the translocation. C) Examples of nanopore current traces for a sample where CRISPR-dCas9 was incubated with DNA. Due to the CRISPR-dCas9 complex that is locally bound along the DNA, additional spikes are seen on top of the DNA events. Left and right traces show type 1 and type 2–1 events, respectively. The dCas9 complex was mixed in a solution of 20 kb dsDNA and incubated at 37°C for 30 min prior to nanopore experiment. The sample was then diluted to a final concentration of 1 M LiCl.

will block a sizable part of the pore volume upon translocating through the nanopore. Though most spikes were sharp, some of them exhibited broadening or more complex features due to sticking events (see SI4.5.7). The results reported here are mainly obtained from one particular experiment on the same pore with N = 308 events recorded for the dCas9-DNA samples as well as N = 308 events for the DNA-only control sample. Similar results were obtained for three independent other runs with different pores (yielding 30%, 34%, and 33% of events with spikes higher than $3I_o$).

The deep spike-like events enable us to clearly separate two different populations, i.e., those with and those without dCas9 bound to the DNA. The two can best be discriminated based on the maximum current blockade of each translocation event. Figure 4.3C,D displays a scatter plot of the maximum current blockade versus dwell time of each translocation event. Both for the dCas9-DNA sample and for the DNA-only control sample, two clusters can be observed with maxima at ~0.12 and ~0.24 nA. These two clusters are due to, respectively, linear head-to-tail translocations of dsDNA, known as type 1 events (cf. Figure 4.2b left) that show up as the 0.12 nA level, and type 2–1 events (cf. Figure 4.2b right) where DNA enters the pore in a folded fashion, resulting in twice the blockade leve l[13]. While virtually all events for bare dsDNA have a maximum current blockade level of less than 0.4 nA, the data for the dCas9-DNA sample shows a population with a clearly larger maximum current blockade level.
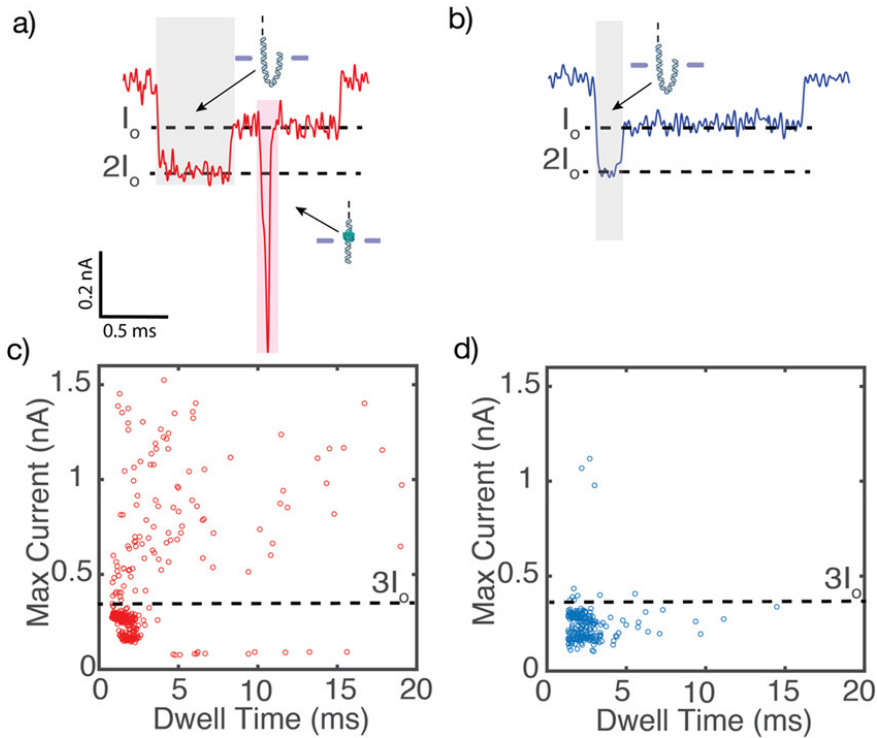
Figure 4.3: **Statistics of nanopore measurements of CRISPR-dCas9 bound to DNA.** A) Typical example of a dCas9-labeled DNA translocation event. The dCas9-labeled DNA displays an additional spike in the current blockade signal that is observed when the DNA-bound protein transverses the pore (shaded in red). A deeper current blockade of DNA at the start of the translocation (shaded in gray) is due to a fold in the DNA as it first enters the pore. B) Example translocation signal from a typical DNA event. C,D) Scatter diagrams of the maximum current blockade versus dwell time of each translocation event for the dCas9-DNA sample and the bare DNA-only control sample, respectively. Unlike the bare DNA sample, the maximum current for dCas9-labeled DNA events shows very large values of 0.4–1.5 nA that clearly exceed 3 times the blockade level I_o for bare DNA ($3I_o = 0.36$ nA).

We observed spikes on a large fraction of the events for the dCas9-DNA sample. Upon using a threshold of $3I_o = 0.36$ nA, we largely select only the events that corresponded to dCas9-bound DNA. In this way, we deduce that 35% of the events (108/308) for the dCas9-DNA sample showed these spikes. In the bare DNA-only control sample, this fraction was much lower, ~5% (10/308). The fraction of spiked events did not reduce during the typical duration of the nanopore experiment of ~2 h, indicating that the dCas9 remained stably bound to the DNA for extended periods of time even in the high-salt nanopore buffer.

We demonstrate that the spikes were indeed due to the bound dCas9 targeting our DNA region of interest by performing a number of different controls (Figure 4.4a). First, we investigated the translocation behavior of only the dCas9 protein by translocating a sample containing 150 nM of dCas9 (~5× excess of the concentration used in the dCas9-DNA experiments). This yielded translocation events only in the opposite applied bias
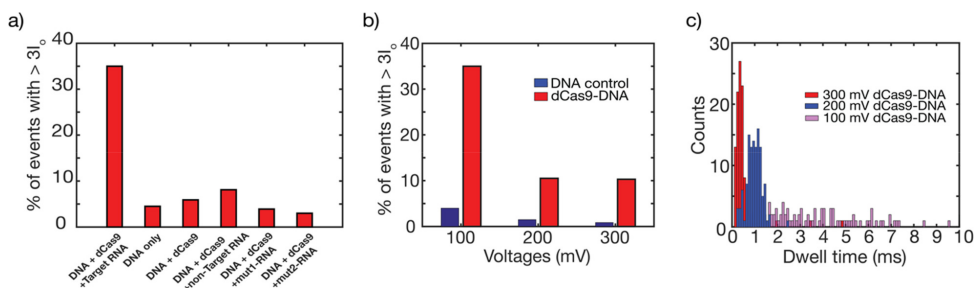
Figure 4.4: **Percentage of spike events and dwell times histograms.** A) Percentage of spike events, for various conditions. Left bar shows a much higher number of events with spikes than in all controls where one of the components was lacking or where the guide RNA was mutated or nonfitting to the target DNA sequence. B) Bar graph showing the percentage of spikes larger than $3I_o$ for the dCas9-DNA sample and the DNA-only control at three different voltages. At all voltages, the percentage of spike events in the dCas9-DNA sample significantly exceeds the presence of spike events of the DNA-only events (that are due to knots and folds). C) Histogram of the dwell times of the dCas9-DNA at 100 mV (purple), 200 mV (blue), and 300 mV (red). At 300 and 200 mV, the distribution times are clustered near 0.5 and 1 ms, respectively, whereas a broadening of the dwell times is observed at 100 mV due to interactions with the pore.

(see SI.4.5.5). Also the dCas9-RNA complex translocated in the opposite polarity to the dCas9-RNA-DNA (see SI.4.5.5). Furthermore, we investigated the effect of the gRNA sequence on the binding of dCas9 to the DNA. For this, we incubated dCas9 with gRNA containing a sequence that is not complementary to our 20 kbp DNA. We saw a sharp drop in the percentage of spike events, as compared to the 35% observed when the gRNA and target site on the 20 kbp DNA were complementary in their sequences. We then performed two more experiments where we used a mutated target gRNA sequence: (i) Mut1, where base pair 1 and 3 (as counted from the NGG region) were mutated, and (ii) Mut2, where every alternate base pair was mutated from the target sequence (see SI.4.5.2, changes highlighted in yellow). In both cases, we again observed a sharp drop in the percentage of spike events, as expected. Only when the entire target sequence is present, the percentage of spike events was found to rise to a much larger value of ~35% (Figure 4.4a).

The fraction of dCas9 events was measured as a function of applied voltage, see Figure4.4b. The percentage of spikes in the dCas9-DNA sample is found to be lower at the higher voltages. Although the current blockade signals are more pronounced at the higher voltages (see SI.11 Figure S-13 for example traces), the translocation speed of the dCas9-DNA molecules is also higher which causes dCas9 spikes to be missed due to the limited bandwidth of the amplifier. Across the entire voltage range, however, the percentage of spikes was always 5–7 times higher than that measured in the DNA-only control sample. The 5% false positives can be attributed to DNA knots which show up as deep blockade events [14]. From the work reported by Plesa et al. we expect about 2–5% events with knots at or beyond the 3I0 level for our linear 20 kb dsDNA. Figure 4.4c shows dwell time histograms of dCas9-DNA events. At the higher applied voltages (cf. the 200 and 300 mV data), we observe, as expected, a narrow dwell-time distribution, indicating that the dCas9-DNA complex flows freely through the pore. At lower voltage, however, a broadening of the distribution is observed for the dCas9-DNA events (e.g., the 100 mV
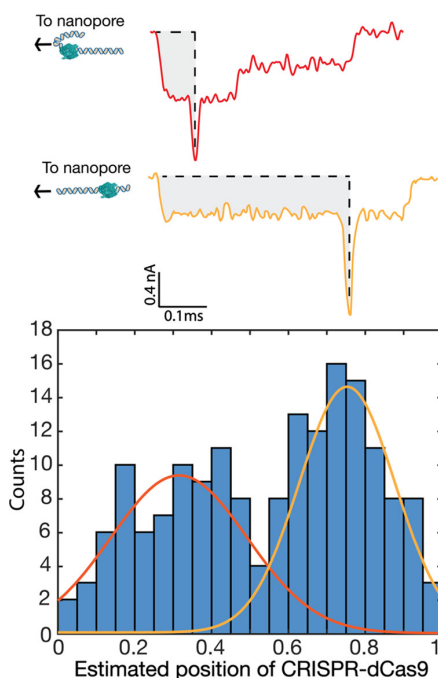
Figure 4.5: **CRISPR-dCas9 binding position as detected in the translocation events.** A) Two examples of events where a dCas9-induced spike is located near the start or end of an event, which can be attributed to the fact that a DNA molecule can enter the pore with either of its two ends. In order to determine the relative binding position of the dCas9 proteins along the DNA, the integral of the current blockade up to the spike position was divided by the total integral of the entire translocation event. B) Histogram of this fraction, binned into 20 bins. Two peaks are observed at 0.31 $\pm$0.04 and 0.75 $\pm$ 0.02 (where the errors are the standard error of the mean). The two peaks correlate well with the designed positions of the target site of the dCas9 on the DNA which are at 0.28 (5872/20678 kbp) or 0.72 (14806/20678 kbp) for the two orientations.

data in Figure 4.4c), which was not seen for the DNA-only sample (see SI.4.12). We attribute this to temporary sticking interactions between the protein and the inner SiN surface of the nanopore, as the dCas9 protein is positively charged in the pH 7.5 buffer (given its isoelectric point of 9), whereas the SiN surface is negatively charged.

Interestingly, we can discern the location where the dCas9 protein binds along the DNA molecule as it translocates through the nanopore. For estimating this location, we measure, for each event, the integral of the current blockade up to the dCas9 spike, as well as the integral of the full event. These values are a measure for, respectively, the amount of DNA that has translocated until the dCas9 is encountered and the total amount of DNA. Accordingly, the relative position of the dCas9 along the DNA strand is given by the ratio of these two integral current values. Figure 4.5 shows a histogram of the dCas9 position obtained from the method thus applied. We observe two peaks, corresponding to the two orientations in which a translocating DNA molecule can enter the nanopore, either first with the end close to the protein-labeled site or, in the other case, leading with the end further away from that site. We fit two Gaussian curves to the

histogram and obtained two peaks at 0.31 ± 0.04 and 0.75 ± 0.02 (errors are the standard error of the mean). These peak values match remarkably well with the targeted site of the dCas9 on the DNA at 0.28 (5872/20678 kbp) or equivalently (counting from the other end) 0.72 (14806/20678 kbp).One might ask whether some error might arise from assuming a constant average translocation velocity, as there will be some speed up of DNA velocity toward the end of the translocation [15]. However, quantitatively this effect is very small for long molecules. The significant width of the two Gaussian peaks can be explained by residual nanopore-protein interactions occurring during translocation as well as by stochastic fluctuations in the velocity of the translocating molecule that broaden the distribution [15]. For the first peak, the folded 2-1 events may furthermore introduce an ambiguity in the localization of the dCas9 peak position in the, relatively rare, cases that the folded region involves a large (>28% of the DNA length) fold at the start of the event.

4.3. Conclusions

Looking ahead, the development of a nanopore-based diagnostic tool for direct DNA detection of disease-inducing agents presents key advantages over traditional serological methods based on the detection of antibodies, proteins, and biomarkers emanating from infectious agents. The presence of such biomarkers can differ strongly depending on the progression and stage of the disease [16], while the DNA of the causative agents remains present throughout. In the scheme proposed here, the use of dCas9 opens new avenues for DNA-sequence-sensing capabilities with large-diameter solid-state nanopores that can be scaled up and mass-produced [17]. The resiliency of the dCas9 protein to the high-salt concentrations (whereas most DNA-binding proteins detach from DNA at high salinity) makes it a particularly fitting candidate as a sequence-specific protein that can be detected through the read-out capabilities of solid-state nanopores.

In recent years, other nanopore-based DNA mapping techniques have been proposed as alternatives to the more conventional PCR-based (polymerase chain reaction amplification) DNA-detection method, which require thermocycling. These proposed nanopore techniques rely on the use of functionalized surfaces or complementary DNA labels [18–22]. Compared to these approaches, our detection scheme has multiple advantages. First, the ease of programmability of the gRNA enables versatile detection of a wide range of targets as well as multiplexing. Other nanopore approaches require extensive preparation of either the sample (design, folding, and attachment of DNA origami labels) or the nanopore surface (cleaning and (re)functionalization of the nanopore), and procedures will have to be repeated between each experimental run for the detection of different analytes. Furthermore, the dCas9 protein can target and search dsDNA directly without any temperature cycling step or additional enzyme for unzipping the DNA. This significantly speeds up the sample processing time, and may be of use for straightforward point-of-care diagnostics. The ease of approach of our proposed dCas9 detection scheme over the other techniques makes nanopore sensing of DNA targets using CRISPR-dCas9 a promising platform for disease detection and diagnostics. Indeed, we envision the use of such nanopore sensing with CRISPR-dCas9 for the fast detection and identification of DNA motifs of medically relevant DNA targets.

4.4. Methods

4.4.1. gRNA-dCas9 Complex Assembly

We assembled gRNA, dCas9 and DNA in a 1× Cas9 Nuclease Reaction Buffer (New England Biolabs, 20 mM HEPES, 100 mM NaCl, 5 mM MgCl2, 0.1 mM EDTA (pH 6.5 @ 25 °C) in a molar ratio of 100:10:1 (RNA/dCas9/DNA). Excess ratios of dCas9 were used to ensure maximum binding of the protein to DNA. For the gel electrophoresis experiments, 1 kbp of DNA was incubated with the dCas9-gRNA complex. Full details on the gRNA sequence, DNA plasmids, and dCas9-gRNA complex assembly protocol can be found in the Supporting Information.

4.4.2. dCas9 binding Assay

The binding affinity of the dCas9 protein to the DNA in 1 M LiCl was first verified using 6% retardation polyacrylamide gel electrophoresis (PAGE). A volume of 10 μL of sample was diluted with 5 μL of 5% glycerol to aid with the loading of the sample into the gel. In all experiments, the sample was first prepared in 1× Cas9 reaction buffer and then diluted to the final salt concentration prior to the gel experiments. Two samples of dCas9-DNA complex were prepared, one with 1 M LiCl (buffered with 10 mM Tris-HCl, 1 mM EDTA, pH 8) and one in 1× Cas9 Nuclease Reaction Buffer (Cas9 reaction buffer) which served as a positive control. For the DNA-only control samples, DNA with the same concentration (300 nM) was diluted in the same salt conditions and loaded into the lane parallel to the respective dCas9-DNA complex lane. The gel was run at 120 V for 2 h and stained with ethidium bromide for imaging.

4.4.3. Nanopore Experiment

We used TEM-drilled 20 nm diameter SiN nanopores for the experiments. The SiN membrane containing the nanopore was loaded in a PEEK (Polyether ether ketone) flow cell. We used Ag/AgCl electrodes and an Axopatch 200B amplifier (Molecular Devices) for current detection. The traces were recorded at 100 kHz and further low pass filtered at 20 kHz for the data at 100 mV and 50 kHz for the data taken from 200 to 300 mV with the Transanalyzer Matlab package [23]. For the nanopore experiments, the dCas9-DNA complex, prepared in 1X reaction buffer, was diluted to a final concentration of 1.5 ng/μL in 1 M LiCl solution (buffered with 10 mM Tris-HCl, 1 mM EDTA, pH 8). Approximately 40 μL of the solution was pipetted to the negatively biased cis compartment of the flow cell. The complex was electrophoretically driven through the nanopore with a bias voltage of 100 mV (or otherwise, as indicated in the text) and detected by measuring changes in the current flowing through the pore. Following the experiment, the flow cell and nanopore were repeatedly flushed with 1 M LiCl solution. Blank traces were recorded to ensure that no residual sample remained prior to the DNA-only control experiment that was carried out in the same nanopore. The total measurement time was typically 1–2 h for each sample. During this time, we observed no discernible decrease in the event rate.

4.5. SUPPORTING INFORMATION

4.5.1. GRNA PRODUCTION

To make the gRNA, we first PCR amplify a dsDNA template which contains the target sequence from a DNA plasmid (pgRNA-bacteria plasmid from Addgen1,2) using a forward primer that contains a T7 promoter. The following thermal cycling conditions were used to generate the PCR template: 98°C for 3 minutes; 98°C for 10 seconds; 65°C for 20 seconds; 72°C for 15 seconds; go to step 2 for 29 cycles and 72°C for 8 minutes. PCR template were verified using gel electrophoresis (1,5% agarose, 1X TBE buffer, 120V for 90 minutes) and subsequently purified using the Wizard®SV Gel and PCR Clean-Up System (Promega) according to the manufacturer's instructions.

Forward primer: TAATACGACTCACTATAGGTACGGT TATCCACAGAATCAGTTTTAGAGCT AGAAATAGCAAGTTAAAATAAGG Reverse primer: AAAAAAAGCACCGACTCGGTGCCAC	gRNA: GGUACGGUUAUCCACAGAAUC AGUUUUAGAGCUAGAAAUAGC AAGUUAAAAUAAGGCUAGUCC GUUAUCAACUUGAAAAAGUGG CACCGAGUCGGUGCUUUUUUU

A single gRNA was then transcribed from the PCR template using the RiboMax^{TM} Large Scale RNA Production Systems kit (Promega) according to the manufacturer's instructions. Following transcription, RNA products were purified using the RNeasy®MinElute®Cleanup Kit (Qiagen) according to the manufacturer's instructions. RNA quality was verified using gel electrophoresis (Mini-Protean®TBE-Urea Precast Gels (Bio-Rad), 200V for 30 minutes).

4.5.2. GRNA SEQUENCE FOR TARGETING, NON-TARGETING RNA, MUT1-RNA, AND MUT2-RNA

Target RNA: TACGGTTATCCACAGAATCA (NGG)
Non—Target RNA: GGCGCATAAAGATGAGACGC (NGG)
Mut1-RNA: TACGGTTATCCACAGATTAA (NGG)
Mut2-RNA: TTCCGATTTGCTCTGTAACT (NGG)
(Mutations with respect to the targeting guide RNA are indicated in yellow.)

4.5.3. PREPARATION OF THE DCAS9-DNA COMPLEX

dCas9 was added to gRNA in a 1X Cas9 Nuclease Reaction Buffer (New England Biolabs) in a molar ratio of 1:10. The sample was incubated for 30 minutes at 25°C. Following this process, 20kbp pSuperCos-γ1,2 DNA, which was linearized with MSCI (New England Biolabs INC), was added in a molar ratio of 1:10 to dCas9 (PNA Bio INC), effecting a total molar ratio of 100:10:1 of gRNA:dCas9:DNA. An excess ratio was used to ensure complete binding. The complex was incubated for 30 minutes at 37°C. The dCas9 is expected to bind to the target sequence TACGGTTATCCACAGAATCA that was located at (14806/20678kbp) of the DNA.

4.5.4. GEL SHIFT ASSAY TO STUDY THE STABILITY OF DCAS9 ON DNA AT HIGH SALT CONCENTRATIONS
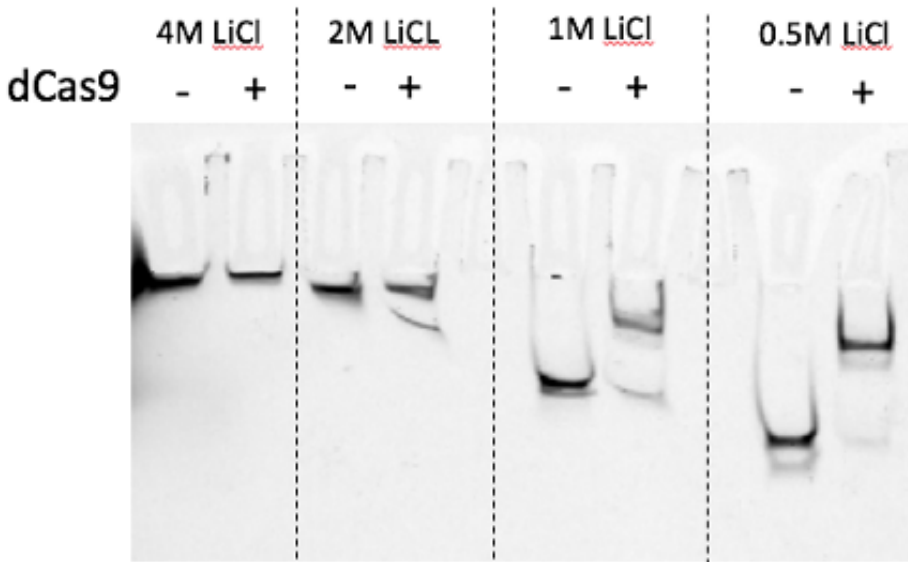
Figure 4.6: **Gel shift assay showing binding of dCas9 in 0.5-4M LiCl nanopore buffer.** A clear shift in the DNA band indicates that the dCas9 remains bound on the DNA at 0.5 and 1M LiCl. We did however not see a significant shift in the 2M and 4M LiCl conditions. The + sign indicates that the dCas9 complex was added to the 1kbp DNA samples.

4.5.5. DCAS9 AND DCAS9+GRNA CURRENT TRACES AND TRANSLOCATION
EVENTS
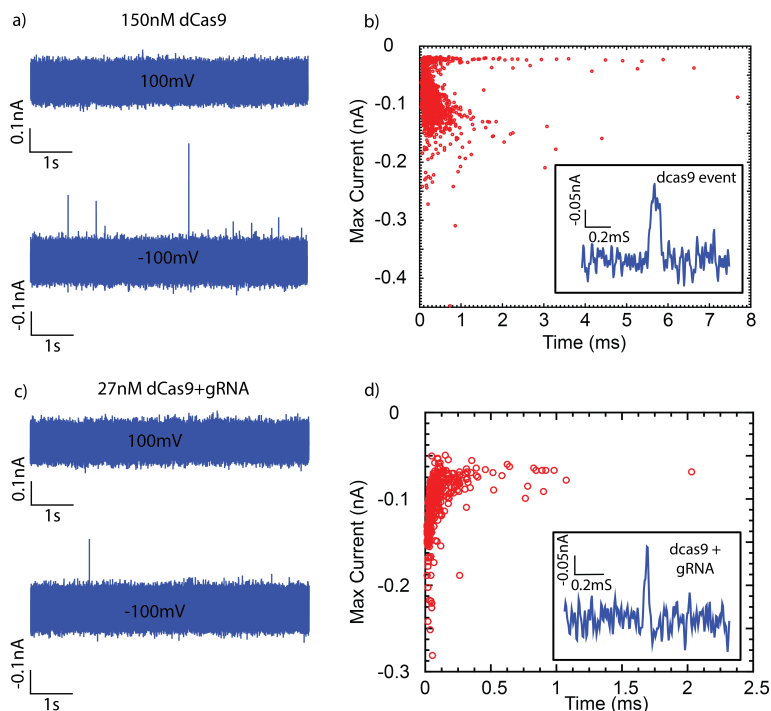
Figure 4.7: **Current traces and scatter diagram of unbound dCas9 and dCas9+gRNA.** a & c) Current trace of dCas9 and dCas9+gRNA, respectively at 150nM and 27nM. Typical baseline current values are ~7.2nA. The blockade signal is taken with respect to the baseline. Note that in the dCas9-only case a), we used 5X the concentration of dCas9 as in the main experiments. The current trace shows events only when the negative bias is applied, namely in the direction opposite to the applied voltage for DNA translocation. b & d) Scatter diagrams of the maximum current. Inserts show example events.

4.5.6. ADDITIONAL EXAMPLE TRACES OF DCAS9 SPIKE EVENTS
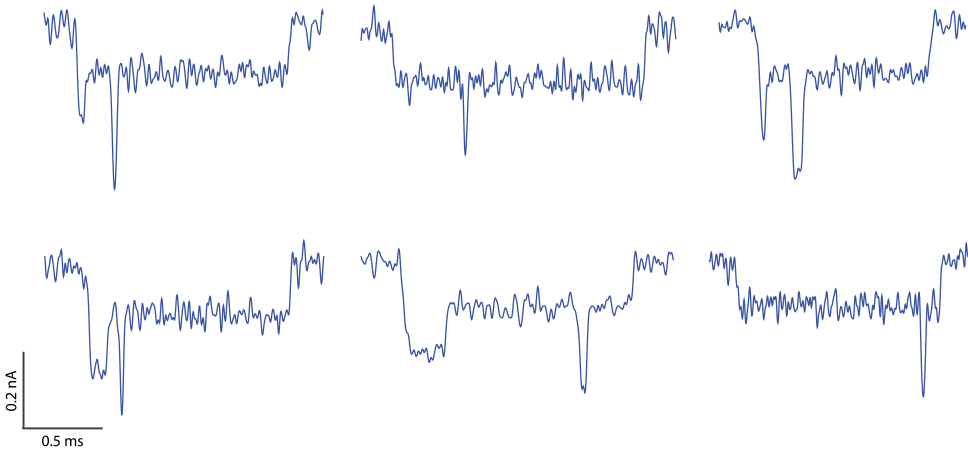
Figure 4.8: **Current traces from the dCas9-DNA complex through a 20nm SiN pore at a 100 mV bias.** The data was collected at the full 100kHz bandwidth of the amplifier and filtered at 20kHz with a Matlab program (Transanalyzer) [23].

4.5.7. EXAMPLE TRACES OF DCAS9 SPIKE EXHIBITING INTERACTIONS WITH THE PORE
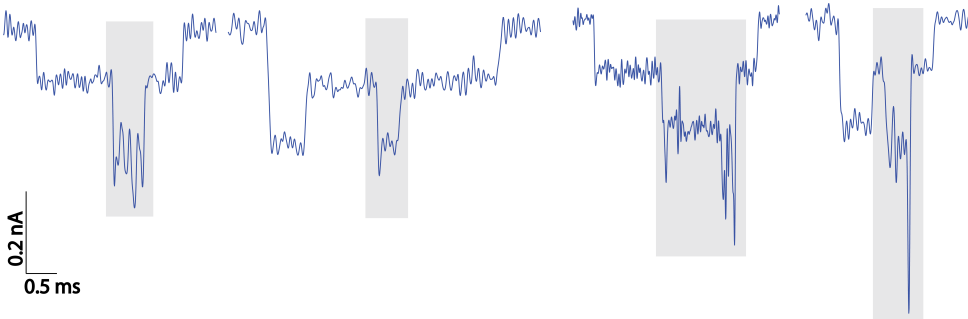
Figure 4.9: **dCas9-DNA complex events showing interactions with the pore** Current traces at 100mV from the dCas9-DNA complex through a 20nm SiN pore where the dCas9 protein was exhibiting interactions with the nanopore (grey shaded area).

4.5.8. SCATTER DIAGRAMS OF THE MAXIMUM CURRENT BLOCKADE VERSUS
DWELL TIME FOR DIFFERENT SAMPLES
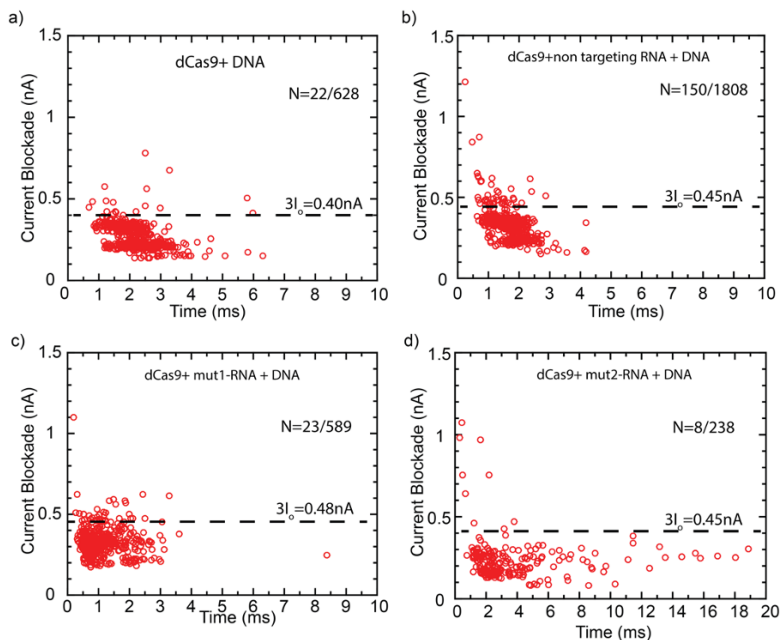
Figure 4.10: **Scatter diagrams of the maximum current blockade versus dwell time at 100mV for different samples.**The fraction of events with a maximum current value of more than 3 times the DNA blockade signal is listed. Mut1 and Mut2 mutational sequences are described in 4.5.2.

4.5.9. SCATTER DIAGRAMS OF THE MAXIMUM CURRENT BLOCKADE TAKEN AT 200MV AND 300MV
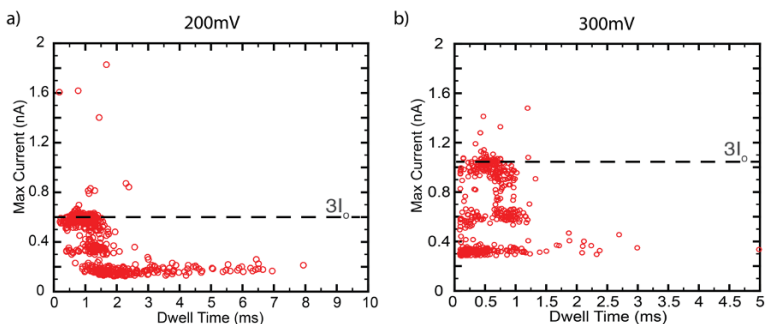
Figure 4.11: **Scatter diagrams of the maximum current blockade versus dwell time.** A) Data for 200mV; B) data for 300mV of the dCas9+gRNA+DNA complex.

4.5.10. HISTOGRAM OF DWELL TIME FOR BARE DNA EVENTS TAKEN AT 100MV AND 300MV
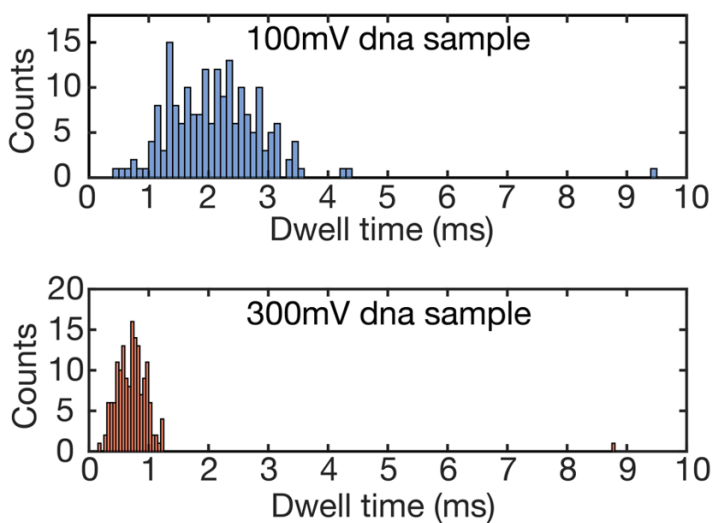
Figure 4.12: **Histogram of dwell times of bare DNA.** Histogram of the dwell times of the bare DNA sample at 100mV (top) and 300mV (bottom).

4.5.11. EXAMPLES OF DATA TRACES AT VARIOUS VOLTAGES
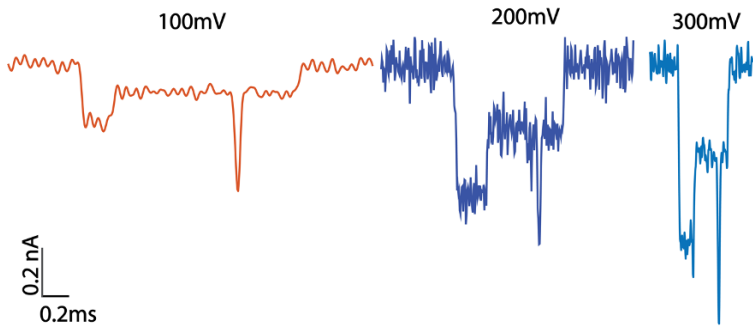
Figure 4.13: **Current traces measured at the applied voltage of 100, 200, and 300mV.** The signal from the higher voltages is larger at the expense of a shorter translocation time. The data were filtered at 20kHz for the 100mV and 50kHz for the 200 and 300mV trace.

REFERENCES

[1] W. Yang, L. Restrepo-Perez, M. Bengtson, S. J. Heerema, A. Birnie, J. van der Torre, and C. Dekker, *Detection of crispr-dcas9 on dna with solid-state nanopores,* Nano letters **18**, 6469 (2018).

[2] H. Bayley, *Nanopore sequencing: From imagination to reality,* Clinical Chemistry **61**, 25 (2015).

[3] C. Dekker, *Solid-state nanopores,* Nature Nanotechnology **2**, 209 (2007).

[4] G. V. Soni and C. Dekker, *Detection of nucleosomal substructures using solid-state nanopores,* Nano Letters **12**, 3180 (2012).

[5] C. Plesa, J. W. Ruitenberg, M. J. Witteveen, and C. Dekker, *Detection of individual proteins bound along DNA using solid-state nanopores,* Nano Letters **15** (2015).

[6] J. Y. Y. Sze, A. P. Ivanov, A. E. G. Cass, and J. B. Edel, *Single molecule multiplexed nanopore protein screening in human serum using aptamer modified DNA carriers,* Nature Communications **8** (2017).

[7] S. Howorka and Z. Siwy, *Nanopores and Nanochannels: From Gene Sequencing to Genome Mapping,* ACS Nano **10**, 9768 (2016).

[8] S. H. Sternberg, S. Redding, M. Jinek, E. C. Greene, and J. A. Doudna, *DNA interrogation by the CRISPR RNA-guided endonuclease Cas9,* Nature **507**, 62 (2014).

[9] O. O. Abudayyeh, J. S. Gootenberg, P. Essletzbichler, S. Han, J. Joung, J. J. Belanto, V. Verdine, D. B. T. Cox, M. J. Kellner, A. Regev, E. S. Lander, D. F. Voytas, A. Y. Ting, and F. Zhang, *RNA targeting with CRISPR–Cas13,* Nature **550**, 280 (2017).

[10] R. E. Haurwitz, M. Jinek, B. Wiedenheft, K. Zhou, and J. A. Doudna, *Sequence- and structure-specific RNA processing by a CRISPR endonuclease,* Science **329**, 1355 (2010).

[11] H. Ma, L.-C. Tu, A. Naseri, M. Huisman, S. Zhang, D. Grunwald, and T. Pederson, *Multiplexed labeling of genomic loci with dCas9 and engineered sgRNAs using CRISPRainbow,* Nature Biotechnology **34**, 528 (2016).

[12] L. S. Qi, M. H. Larson, L. A. Gilbert, J. A. Doudna, J. S. Weissman, A. P. Arkin, and W. A. Lim, *Repurposing CRISPR as an RNA-γuided platform for sequence-specific control of gene expression,* Cell **152**, 1173 (2013).

[13] A. J. Storm, J. H. Chen, H. W. Zandbergen, and C. Dekker, *Translocation of double-strand DNA through a silicon oxide nanopore,* Physical Review E **71**, 051903 (2005).

[14] C. Plesa, D. Verschueren, S. Pud, J. Van Der Torre, J. W. Ruitenberg, M. J. Witteveen, M. P. Jonsson, A. Y. Grosberg, Y. Rabin, and C. Dekker, *Direct observation of DNA knots using a solid-state nanopore,* Nature Nanotechnology **11**, 1093 (2016).

[15] C. Plesa, N. Van Loo, P. Ketterer, H. Dietz, and C. Dekker, *Velocity of DNA during translocation through a solid-state nanopore,* Nano Letters **15**, 732 (2015).

[16] W. Fierz, *Basic problems of serological laboratory diagnosis.* Methods in molecular medicine **94**, 393 (2004).

[17] D. V. Verschueren, W. Yang, and C. Dekker, *Lithography-based fabrication of nanopore arrays in freestanding sin and graphene membranes,* Nanotechnology **29**, 145302 (2018).

[18] R. Wei, D. Pedone, A. Zürner, M. Döblinger, and U. Rant, *Fabrication of metallized nanopores in silicon nitride membranes for single-molecule sensing,* Small **6**, 1406 (2010).

[19] U. Rant, K. Arinaga, S. Scherer, E. Pringsheim, S. Fujita, N. Yokoyama, M. Tornow, and G. Abstreiter, *Switchable DNA interfaces for the highly sensitive detection of label-free DNA targets,* Proceedings of the National Academy of Sciences of the United States of America **104**, 17364 (2007).

[20] H. Zhang, J. Chao, D. Pan, H. Liu, Y. Qiang, K. Liu, C. Cui, J. Chen, Q. Huang, J. Hu, L. Wang, W. Huang, Y. Shi, and C. Fan, *DNA origami-based shape IDs for single-molecule nanomechanical genotyping,* Nature Communications **8** (2017).

[21] J. Kong, J. Zhu, and U. F. Keyser, *Single molecule based SNP detection using designed DNA carriers and solid-state nanopores,* Chemical Communications **53**, 436 (2017).

[22] S. Hernández-Ainsa, N. A. W. Bell, V. V. Thacker, K. Göpfrich, K. Misiunas, M. E. Fuentes-Perez, F. Moreno-Herrero, and U. F. Keyser, *DNA origami nanopores for controlling DNA translocation,* ACS Nano **7**, 6024 (2013).

[23] C. Plesa and C. Dekker, *Data analysis methods for solid-state nanopores,* Nanotechnology **26**, 084003 (2015).

5

DNA SEQUENCE-DIRECTED COOPERATION BETWEEN NUCLEOID-ASSOCIATED PROTEINS

Nucleoid associated proteins (NAPs) are a class of highly abundant DNA binding proteins in bacteria and archaea. While the composition and relative abundance of the NAPs change during the bacterial growth cycle, surprisingly little is known about their crosstalk in mutually binding to the bacterial chromosome and stabilising higher-order nucleoprotein complexes. Here, we use atomic force microscopy and solid-state nanopores to investigate long-range nucleoprotein structures formed by the binding of two major NAPs, FIS and H-NS, to DNA molecules with distinct binding-site arrangements. We find that spatial organisation of the protein binding sites can govern the higher-order architecture of the nucleoprotein complexes. Based on sequence arrangement the complexes differed in their global shape and compaction, as well as the extent of FIS and H-NS binding. Our observations highlight the important role the DNA sequence plays in driving structural differentiations within the bacterial chromosome.

5.1. INTRODUCTION

Nucleoid-associated proteins (NAPs) represent a small class of highly abundant DNA architectural proteins involved in shaping the bacterial chromatin as well as in regulating the gene expression in prokaryotes and archaea [2–6]. During the bacterial growth cycle, these proteins are expressed in a growth-phase-dependent manner to coordinate the chromosome structure with the metabolic state [7–10]. NAPs bind DNA with varying affinities from nanomolar to micromolar concentrations and affect the gene expression by acting as bona fide transcription factors as well as so-called "topological homeostats" [11, 12]. The regulation of genomic transcription by NAPs is closely coupled to the availability of free or "unconstrained" DNA superhelicity, as NAPs constrain the DNA acting both as supercoil repositories and topological barriers to supercoil diffusion [12–16].

Factor for Inversion Stimulation (FIS) protein is the most abundant NAP during the exponential growth phase in Escherichia coli, while its concentration quickly drops to undetectable levels upon the transition of cells to stationary phase [7, 17, 18]. FIS has a global nucleoid-structuring function [19–22] as well as local accessory roles in the assembly of synaptic complexes by site-specific recombinases [23, 24]and transcription-initiation complexes at various promoters, including the exceptionally strong RNA (rRNA and tRNA) promoters [25, 26]. The latter are characterized by upstream activating sequences (UAS) containing multiple FIS-binding sites that are arranged in a helical register [27]. FIS is also a helix-turn-helix (HTH) DNA-bending protein [28] which upon binding at the phased sites in UAS forms a coherently bent DNA loop that associates with RNA polymerase [29]. In general, FIS nucleoprotein complexes form loops and stabilise branches in supercoiled DNA [11, 30–32].

In contrast to FIS, the Histone-like Nucleoid-Structuring (H-NS) protein is a NAP expressed throughout the entire bacterial growth cycle [7], slightly increasing in concentration towards the later growth stages. While overproduction of H-NS in vivo is lethal for the cel l[33], the deletion of the hns gene does not result in large scale restructuring of the nucleoid [19, 34, 35]. H-NS is a DNA-bridging protein that binds preferentially to A/T-rich DNA sequences [36, 37], in part mediated by an A-T hook motif that interacts with the DNA minor groove [38, 39]. It was shown that H-NS can bridge two DNA helices within a rigid filament [40, 41], trapping RNA polymerase [42, 43]. It is assumed that binding of H-NS nucleates at high-affinity sites and subsequently spreads along the DNA strands, leading to gene silencing [44–46]. While H-NS can polymerize on a single DNA duplex, resulting in its stiffening [47], it is the DNA-bridging mode facilitated by Mg^{2+} ions that has been primarily implicated in transcriptional repression [48–50].

While the structural role of FIS, H-NS and other DNA-binding NAPs has been intensively studied [19–22, 29, 40, 41], surprisingly little is known about putative cooperative binding effects and the architecture of the ensuing long-range DNA structures. From NAP expression patterns [7] it is clear that distinct combinations of these proteins interact with the genomic DNA during the different stages of the cell cycle [10]. Indeed, exploration of their cooperative binding effects appears indispensable for understanding gene regulation. Interestingly, previous studies using Atomic Force Microscopy (AFM) showed that cooperative binding of various combinations of NAPs to the linear phage λ-DNA led to regular structures that were quite distinct from those observed with individual proteins [51], while on binding to large supercoiled molecules, NAPs did phase

separate, forming domain-like regions [32]. Resolving specific higher-order structures formed by cooperative binding of NAPs is challenging, but it can be achieved by using model DNA sequences that contain a few high-affinity binding sites that facilitate the nucleation of long-range nucleoprotein complexes.

Two complementary single molecule techniques for probing DNA architecture are AFM microscopy and ionic pulse sensing in a solid state nanopore. AFM involves using a sharp cantilever to directly probe and 'feel' a surface as the sharp tip rasterises across the field of view [52–54]. Sample, such as DNA is mapped as changes in the surface interaction that can be reconstructed into height changes in a 3D map. The sample requires no further treatment beyond deposition on a freshly cleaved mica surface and is usually mapped in ambient air. While noted for their high resolution and label free method, AFM microscopy techniques suffer from a variety of effects including interactions with the surface, drying artefacts and long rastering times for the large enough field of view to gather enough statistics [55].

Solid state nanopores on the other hand, are able to screen large numbers of molecules in solution at the single molecule level which makes them an excellent complimentary tool to the AFM techniques [56]. Solid state nanopore employ the use of a tiny nanoaperture etched in a membrane separating two reservoirs. Analyte such as DNA are immersed in an ionic solution and electrophoretically driven through this aperture. During the passage through the aperture, the DNA blocks the flow of ions and shows up as current blockade in the measured ionic current trace. The current blockade depends on the volume of ions displaced and hence the instantaneous amount of DNA translocating through the pore. Nanopores have been successfully used in research to probe physical organisation of DNA such as knots and folds at the single molecule level as well as the degree of protein-induced DNA compaction which shows up as distinct current blockade levels [57–59].

Here, we explore whether the binding of a combination of two major bacterial NAPs, FIS and H-NS, leads to the emergence of distinct nucleoprotein structures that are more than the mere sum of those formed by the individual NAPs. Stating the question directly, "does the arrangement of the DNA sequence matter?". To address this question, we employed DNA sequences with various arrangements of FIS and H-NS binding sites and study the resulting higher-order nucleoprotein complexes using nanopore experiments in support of a larger work combining AFM studies.

5.2. FABRICATION AND RESULTS

5.2.1. PREPARATION OF THE PLASMID

To study the combined effects of FIS and H-NS proteins binding to DNA, we used two plasmids that differed in the sequence arrangement of the NAP-binding sites (Figure 5.1a,b). In one construct, we arranged a FIS-binding sequence UAS and an H-NS-binding sequence NRE in a Head-to-Tail fashion (HT: UAS-NRE-UAS-NRE). Here, UAS is the upstream activating sequence of tyrosyl tRNA gene promoter (tyrT UAS) [60] and NRE is the negative regulatory element of proV gene (proV NRE) from an osmoregulatory operon [61]. In the second construct, the same NAP-binding sequences were arranged in a Head-to-Head fashion (HH: UAS-NRE-NRE-UAS). These sequences were inserted into

a 2.9kb backbone devoid of any strong FIS or H-NS binding sites [32] (Figure 5.1.a & b, Materials and Methods). The 397bp-long tyrT UAS region contained three specific FIS binding sites (with Kd values ranging between 7.5 nM and 60 nM) arranged in a helical register [25], while the 264 bp long proV NRE contained two high-affinity H-NS sites (Kd values between 15 nM and 25 nM) separated by about 10 helical turns [44]. The constructs with Head-to-Tail (HT) and Head-to-Head (HH) arrangements have been described in detail in a previous study [32], which showed that the binding of H-NS to various arrangements of high-affinity binding sites led to the formation of distinct long-range plectonemic coiled structures, that differed in their shape, compaction, and capacity to constrain DNA supercoils.The total length of each of the two constructs were 4kb. As an additional control, we used pBR322 plasmid of a similar size (4.4kb) that was devoid of any strong FIS binding sites.
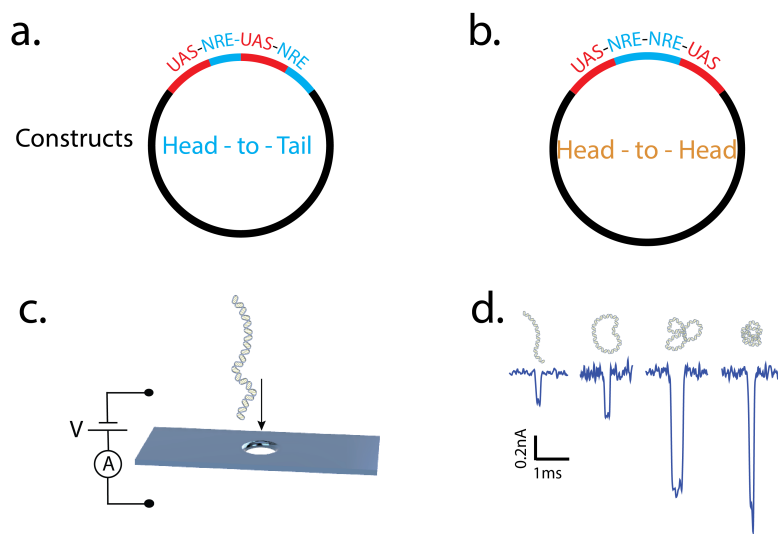
Figure 5.1: **Design of plasmid and schematics of experiment.** Design of plasmid and schematics of experiment. a-b) Schematic depiction of the Head-to-Tail (HT) and Head-to-Head (HH) circular constructs. The two plasmid were identical except for the arrangements of their UAS and NRE sequences. c) Schematics depicting the translocation of a DNA through a nanopore. d) Sample traces illustrating that different degrees of DNA compaction will show up as different maximum amplitudes in the current blockade level.

5.2.2. NANOPORE EXPERIMENTS

We investigated the formation of these nucleoprotein complexes in solution by use of solid-state nanopores (Fig. 5.1c). As schematically illustrated in Figure 5.1d, one can distinguish the level of folding and compaction of DNA molecules based on their current blockade levels [57, 58], as well as see if the molecules are bound by proteins [62]. If the HH and HT nucleoprotein complexes were different in their level of compaction, one would expect to see different blockade levels between the two constructs, i.e the higher the degree of compaction, the deeper the blockade level should be.

The two plasmids were incubated with FIS (5.6ng/μl incubation concentration) and

H-NS 6ng/μl incubation concentration) with the respective DNA molecules (10ng/μl) in binding buffer(we used DNA elution buffer (10mM Tris) in this case) for 10 mins. Each of the sample was then diluted 10 times in 1M LiCl buffer to a final DNA concentration of 1ng/μl and added to the cis side of the nanopore (15nm, TEM drilled SiN nanopore). A voltage of 100mV was applied and clear dips in the current can be seen in the current trace which show up as transient downward spikes. Figure5.2 a and b show the sample current trace for HH and HT incubated with FIS & H-NS respectively. The current dips represent the passage of the nucleoprotein complexes and recorded as events. Several hundred events were recorded in each condition to ensure sufficient statistics. Between the different samples, the nanopore was flushed with 1M LiCL solution and blank traces were recorded to prove that all of the preceding sample has been washed away (Figure 5.2). Additional details on the nanopore setup can be found in the method section.
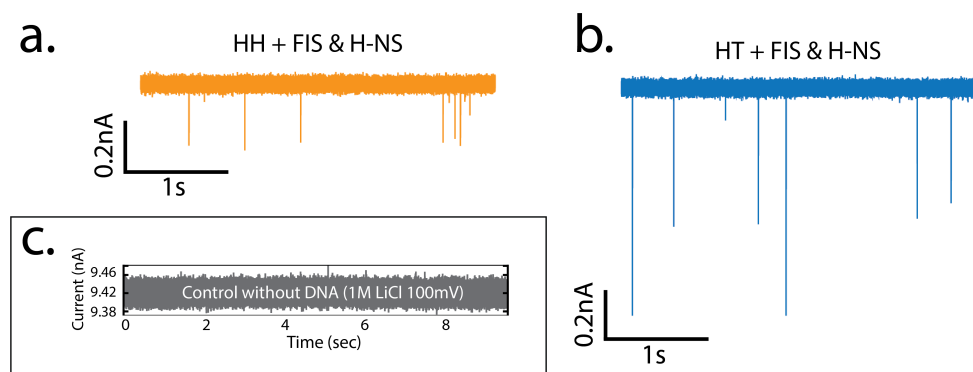
Figure 5.2: **Typical blockade events for HH and HT DNA construct passing through a nanopore.** a) Typical nanopore traces for the HH + FIS & H-NS samples (1ng/μl final DNA concentration, 100mV). b) Typical nanopore traces for HT+ FIS & H-NS samples, (1ng/μl final DNA concentration, 100mV). We note that the events are hetergenous and reach different blockade levels as compared to the HH case. c) Open nanopore current when no sample was added. No events can be seen.

We observe that the HT+FIS&H-NS sample showed much deeper and hetergenous blockade levels compared to the HH+FIS&H-NS sample in the current trace displayed in Figure 5.2 a and b. This deeper blockade level suggest a more compacted DNA in the case of HT+FIS& H-NS as more of the nanopore is blocked during the passage of the molecule. The nanopore events were collected and plotted in a scatter plot (see SI Figure 5.8) of their maximum amplitude reached and their calculated translocation time (dwell time)[62].

We calculated the increase in the number of deep events (more compacted DNA) for the HT and HH DNA when incubated with the proteins. To control for innate differences in the quality of the purified DNA for each of the plasmid, we set a threshold to select for the protein-bound molecules to obtain the percentage of events as compared to the control (the DNA only case, i.e, the average current blockade of a single-helix DNA event). This was done in order to measure the relative increase in the current blockade when the proteins were added to each of the respective plasmid. Figure 5.3a and b. show the relative increase in the number of deep events for the HT and HH case in the presence of
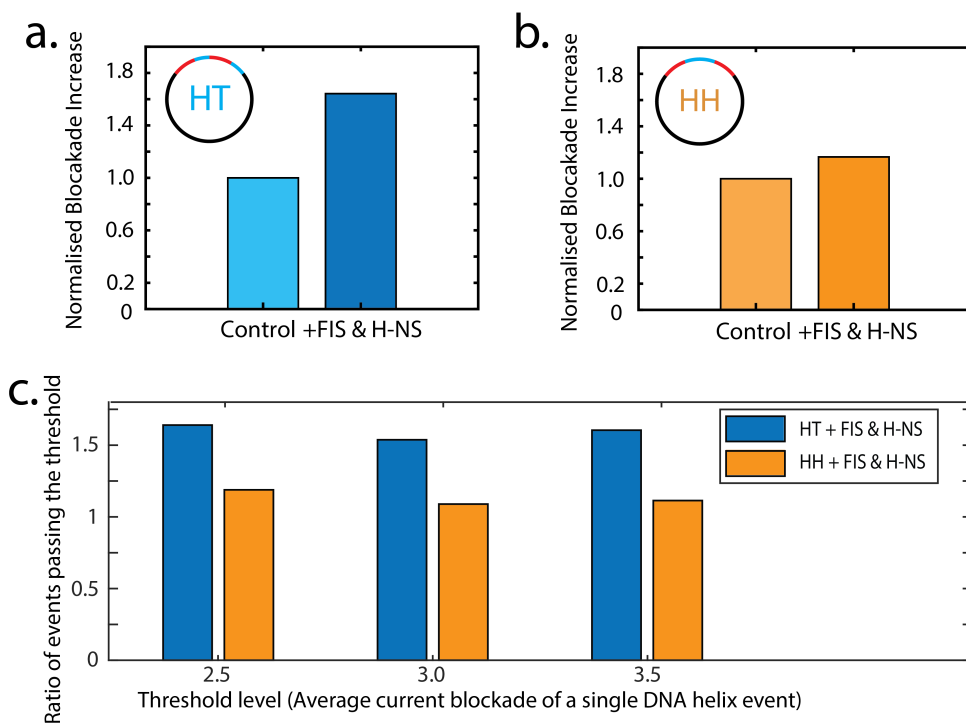
Figure 5.3: **Normalised increase in the blockade current.** . a-b) Normalized blockade events for the HT and HH constructs, showing that the deeper events occur much more frequently for the HT construct (in 38% of total events, $N_{HT+Protein}$=277 out of 737 total events), but not for the HH construct (in 18% of total events, $N_{HH+Proteins}$=329 out of 1812 total events). Overall this represented a 1.65 fold increase in the number of deep events for the HT construct, but only a 1.19 fold increase for the HH construct as compared to their DNA-only condition. c) Increase in deep events as set by threshold level. We see that the effect is significant irrespective of the used threshold up to 3.5X the average single helix DNA level.

both proteins. We observed a 1.65 fold increase in the number of deep events for the HT construct, but only a 1.19 fold increase for the HH construct. These data confirm that the NAPs binding of the HT construct indeed results in an increased compaction compared to the HH construct (irrespective of the used threshold, see Figure 5.3c which plots the increased in blockade vs. the threshold level).

Furthermore, while for HH-DNA, the blockade events in the presence of FIS and H-NS were uniform and homogeneous, the addition of individual NAPs to HH construct resulted in heterogeneous blockade levels. Figure5.4a shows the respective current trace. Furthermore, for HH-DNA, the blockade events in the presence of FIS and H-NS simultaneously were uniform and homogeneous, indicative of a similar organization of nucleoprotein complexes, whereas addition of individual NAPs to HH construct resulted in heterogeneous blockade levels (Figure 5.4b, the addition of H-NS to HH-DNA led to an increase in the number of events with a deep blocakde). This finding is consistent with the formation of regular hairpin structures in the presence of both FIS and H-NS observed in AFM [1].
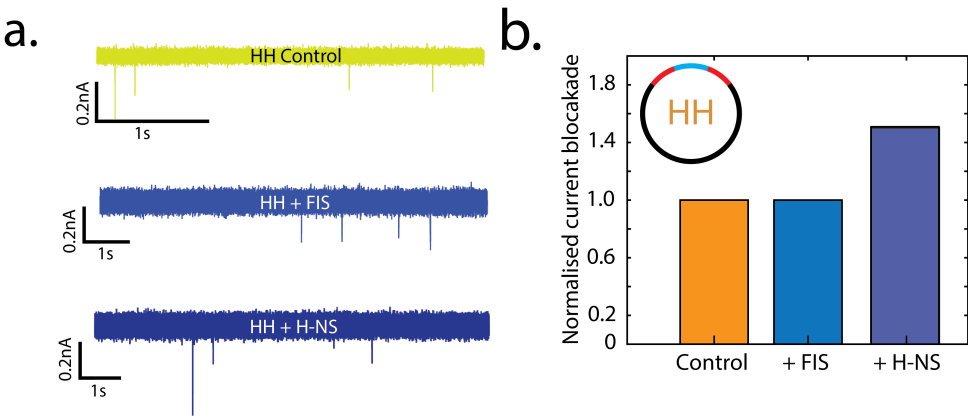
Figure 5.4: HH DNA showing binding with single NAPs. .a) Top to bottom: Sample current trace of HH-DNA, HH+FIS and HH+H-NS. (1ng/μl , 100mV). The events stayed largely homgenous except when H-NS was incubated with the sample. b) Bar graph showing the increased in blockade of HH-DNA with individual NAPs -HH construct bound with FIS,HH construct bound by H-NS. No significant increase can be seen except in the case where H-NS was added where we get deep and heterogeneous blockades, indicating various levels of nucleoprotein compaction.
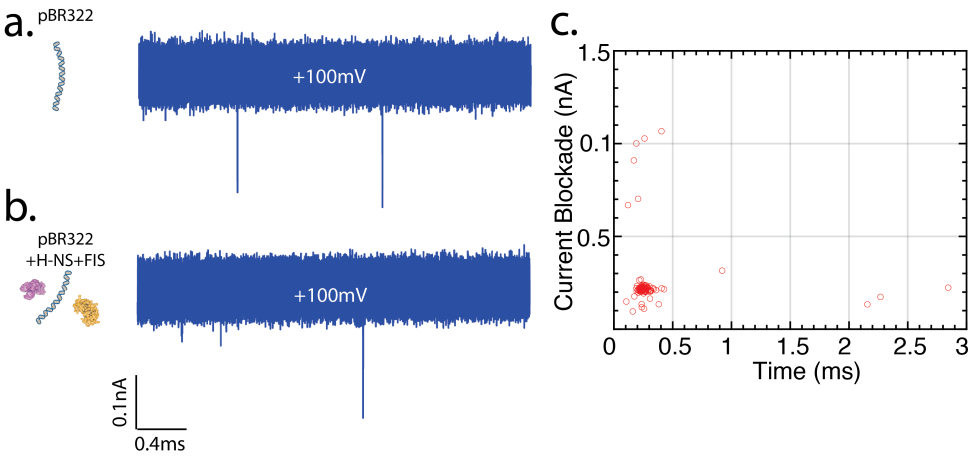
Figure 5.5: pBR322 control experiments in a nanopore .a-b) Sample current trace of pBR322and pBR322 incubated with H-NS and FIS in a nanopore (1ng/μl, 1M LiCL, 100mV). The events are extremely consistent at the 0.2nA level and we do not see any noticable change this level upon addition of the proteins. C) Collected scatter plot of pBR322 + H-NS and FIS showing no significant deep current blockade levels.
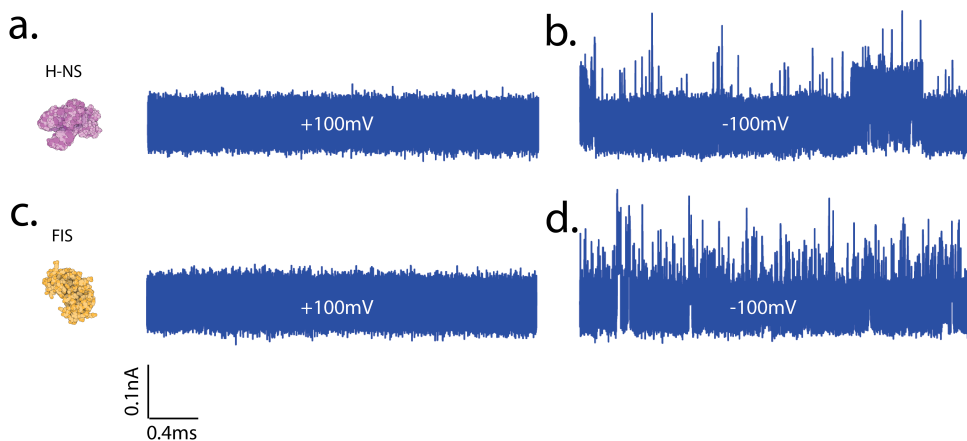
Figure 5.6: **Protein controls in a nanopore.** a-b) Sample current trace of H-NS in the forward (+100mv) and reverse bias (-100mV). No translocation can be seen in the forward bias and clear translocation can only be seen in the reverse bias. c-d) Sample current trace of FIS in the forward (+100mv) and reverse bias (-100mV). Clear translocation can only be seen in the reverse bias. These results indicate that the unbound proteins travel in the opposite direction to the direction of the DNA translocation.

As a control, we measured pBR322 which is known to have no strong FIS or H-NS binding sites. Figure5.5 a and b shows the sample trace from pBR322 and pBR322 incubated with the combination of the proteins (DNA-1ng/μl). Both pbR322 only and pBR322+H-NS& FIS sample displayed a current trace that was a homogenous blockade level even after incubation with H-NS and FIS. The events were collected and binned into the scatter plot in Figure 5.5c. No significant deep current blockade event can be seen in the collected scatter plot of the pBR322 - H-NS and FIS condition. To ensure that the nanopore had sufficient resolution and to eliminate the hypothesis of protein-pore interactions or co-translocation of unbound protein aggregates and DNA, we measured a sample containing only H-NS or FIS that was introduced in the same cis side as the DNA sample. Figure 5.6a and c shows the respective current trace in the forward bias (+100mV, the same bias applied for the DNA sample). When a negative bias was applied, clear upward events indicating protein translocation can be seen (-100mV, Figure 5.6b, d). This indicates that unbound proteins are drawn in the oppositely charged electrode and direction of the translocation of DNA [63].

5.3. CONCLUSION

In summary, to study the nucleoprotein complexes formed by combination of FIS and H-NS, we used two DNA substrates with a spatially different, Head-to-Head (HH) or Head-to-Tail (HT) arrangement of the NAP binding sites. In the nanopore studies, we see an increased compaction of the HT nucleoprotein complexes formed by FIS and H-NS (Figure 5.3, SI Figure 5.8). Additionally, we found that the HH nucleoprotein complexes formed by FIS and H-NS demonstrated regular current blockade levels in contrast to HT (Fig. 5.4) which suggest a higher structural regularity of the HH nucleoprotein com-

plexes compared to that of the HT nucleoprotein complexes. No binding or compaction was observed in the pBR322 case where there are no strong FIS or H-NS binding sites.

Taken together, the nanopore results demonstrates in bulk that there is increased binding and compaction of DNA in the HT arrangement as compared to the HH arrangement. These findings are consistent with further AFM study which shows structurally distinct nucleoprotein complexes formed by both arrangements. Remarkably, the two plasmid differed only in the arrangement of their UAS and NRE sequences. This shows that the presence of these sequence sites alone were not sufficient for DNA compaction and the arrangement of the sequence mattered in the formation of more compact and stable nucleoprotein complexes. Together with high resolution AFM imaging which can directly observe the structures and shape formed by the nucleoprotein complexes, the complex interplay between NAPs and their cognate genomic binding sites can be probed in order to understand spatiotemporal organisation of DNA structures.

5

5.4. MATERIALS AND METHODS

5.4.1. DNA AND PROTEIN PREPARATION

The two 3997 bp constructs (Head-to-Tail and Head-to-Head) were constructed as described earlier[32]. Briefly, the constructs contained sequences with FIS binding sites amplified from the UAS of the tyrT gene (denoted as UAS) and sequences with H-NS binding sites amplified from the NRE of proV gene (denoted as NRE) of E. coli. In these two constructs the individual UAS and NRE elements were cloned in different spatial arrangements.

Circular DNA constructs were nicked using the Nt.BspQI nuclease (New England BioLabs) and purified from 1% agarose gel. DNA was then diluted in the P1 buffer (1mM TRIS-HCl, 4mM MgCl2 , 0.003% Tween 20, 2.5% Glycerol, pH 7.9) to a final concentration of 10 ng/μl. Fis and H-NS were purified as previously described [64, 65].

5.4.2. NANOPORE EXPERIMENTS

We used TEM-drilled 15 nm diameter SiN nanopores for the experiments. The SiN membrane containing the nanopore was loaded in a PEEK (Polyether ether ketone) flow cell. The DNA samples were diluted in 1M LiCl to a final concentration of 1ng/μl before being introduced to the cis side (-ve) of the nanopore. We used Ag/AgCl electrodes and an Axopatch 200B amplifier (Molecular Devices) for current detection. In experiments where FIS (5.6ng/μl incubation concentration) and/or H-NS (6ng/μl incubation concentration) were used, the DNA molecules (10ng/μl) were pre-incubated with proteins in the binding buffer for 10min at room temperature. Afterwards the sample was diluted 10 times in 1M LiCl buffer (final DNA contecntration 1ng/μl) and added to the cis side of the nanopopore. Blank traces were recorded to ensure that no residual sample remained prior to the DNA-only control experiment that was carried out in the same nanopore. The total measurement time was typically 1–2 h for each sample. During this time, we observed no discernible decrease in the event rate.

The traces were recorded at 200 kHz and further low pass filtered at 10 kHz with the Transanalyzer Matlab package [66]. As DNA purification quality as well as self-folding of the DNA duplex may affect the current blockade levels, we normalized the blockade levels for each construct to set the control standard for comparison of the protein-bound constructs. We set a current blockade threshold at 2.5 times higher than the average current blockade of a single DNA helix event (threshold = 2.5·I_{DNA}) and quantified the percentage of events above this threshold as compared to the control. Variation of the thresholding level had nearly no effect on the results, as can be seen in Fig 5.3.

5.5. SUPPORTING INFORMATION

5.5.1. SAMPLE CURRENT TRACE FOR HT-DNA ONLY
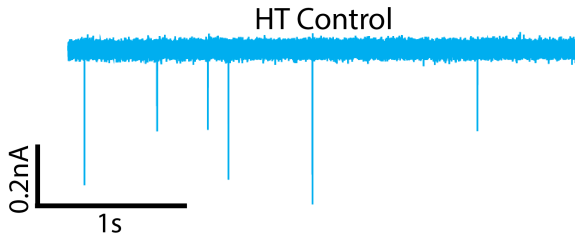
Figure 5.7: **Sample current trace for HT-DNA only** Sample current trace taken at 100mV for HT-DNA only (1ng/μl, 1M LiCL)

5.5.2. SCATTER PLOT FOR COLLECTED EVENT FOR THE DIFFERENT CONDITIONS.
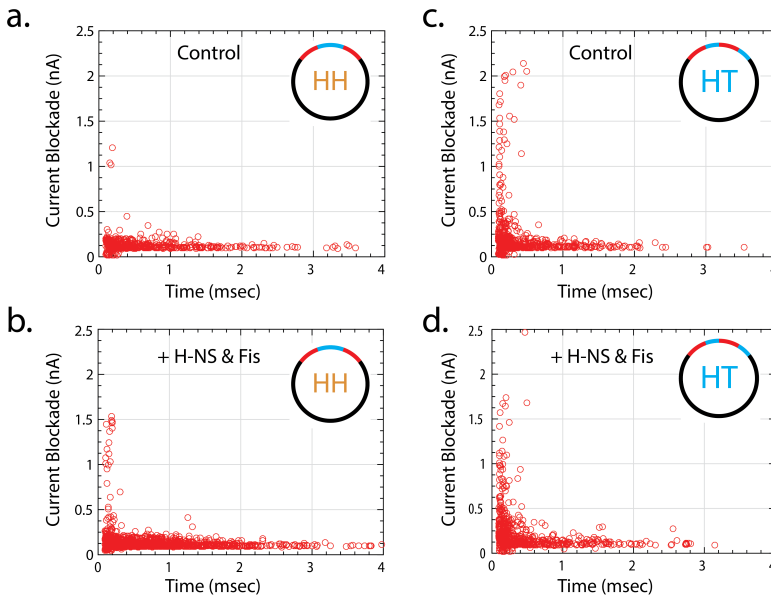
Figure 5.8: **Scatter plot for collected event for the different conditions.** Current blockade vs. blockade time scatter plots for a) control (N=491) and b) H-NS & FIS bound HH samples (N=1812). c) Current blockade vs. blockade duration scatter plots for control (N=707) and d) H-NS & FIS bound HT samples (N=737).

REFERENCES

[1] A. Japaridze, W. Yang, C. Dekker, W. Nasser, and G. Muskhelishvili, *Dna sequence-directed cooperation between nucleoid-associated proteins,* bioRxiv (2020).

[2] A. Travers and G. Muskhelishvili, *Bacterial chromatin,* Current Opinion in Genetics and Development **15**, 507 (2005).

[3] S. C. Dillon and C. J. Dorman, *Bacterial nucleoid-associated proteins, nucleoid structure and gene expression,* Nature Reviews Microbiology **8**, 185 (2010).

[4] M. S. Luijsterburg, M. C. Noom, G. J. Wuite, and R. T. Dame, *The architectural role of nucleoid-associated proteins in the organization of bacterial chromatin: A molecular perspective,* Journal of Structural Biology **156**, 262 (2006).

[5] R. P. C. Driessen and R. T. Dame, *Nucleoid-associated proteins in Crenarchaea,* Biochemical Society Transactions **39**, 116 (2011).

[6] R. T. Dame, F. Z. M. Rashid, and D. C. Grainger, *Chromosome organization in bacteria: mechanistic insights into genome structure and function,* Nature Reviews Genetics **21**, 227 (2020).

[7] T. A. Azam, A. Iwata, A. Nishimura, S. Ueda, and A. Ishihama, *Growth phase-dependent variation in protein composition of the Escherichia coli nucleoid,* Journal of Bacteriology **181**, 6361 (1999).

[8] N. Sonnenschein, M. Geertz, G. Muskhelishvili, and M. T. Hütt, *Analog regulation of metabolic demand,* BMC Systems Biology **5**, 40 (2011).

[9] P. Sobetzko, A. Travers, and G. Muskhelishvili, *Gene order and chromosome dynamics coordinate spatiotemporal gene expression during the bacterial growth cycle,* Proceedings of the National Academy of Sciences **109**, E42 (2012).

[10] A. Travers and G. Muskhelishvili, *Chromosomal Organization and Regulation of Genetic Function in Escherichia coli Integrates the DNA Analog and Digital Information,* EcoSal Plus **9** (2020).

[11] A. Travers, R. Schneider, and G. Muskhelishvili, *Dna supercoiling and transcription in escherichia coli: The fis connection,* Biochimie **83**, 213 (2001).

[12] G. Muskhelishvili and A. Travers, *Transcription factor as a topological homeostat,* Frontiers in Bioscience **8**, 279 (2003).

[13] G. W. Hatfield and C. J. Benham, *Dna topology-mediated control of global gene expression in escherichia coli,* Annual review of genetics **36**, 175 (2002).

[14] C. D. Hardy and N. R. Cozzarelli, *A genetic selection for supercoiling mutants of Escherichiacoli reveals proteins implicated in chromosome structure,* Molecular Microbiology **57**, 1636 (2005).

[15] M. Berger, V. Gerganova, P. Berger, R. Rapiteanu, V. Lisicovas, and U. Dobrindt, *Genes on a wire: The nucleoid-associated protein HU insulates transcription units in Escherichia coli,* Scientific Reports **6**, 31512 (2016).

[16] S. Dages, X. Zhi, and F. Leng, *Fis protein forms DNA topological barriers to confine transcription-coupled DNA supercoiling in Escherichia coli,* FEBS Letters **594**, 791 (2020).

[17] C. A. Ball, R. Osuna, K. C. Ferguson, and R. C. Johnson, *Dramatic changes in Fis levels upon nutrient upshift in Escherichia coli,* Journal of Bacteriology **174**, 8043 (1992).

[18] O. Ninnemann, C. Koch, and R. Kahmann, *The E.coli fis promoter is subject to stringent control and autoregulation.* The EMBO Journal **11**, 1075 (1992).

[19] F. Wu, P. Swain, L. Kuijpers, X. Zheng, K. Felter, M. Guurink, J. Solari, S. Jun, T. S. Shimizu, D. Chaudhuri, B. Mulder, and C. Dekker, *Cell Boundary Confinement Sets the Size and Position of the E. coli Chromosome,* Current Biology **29**, 2131 (2019).

[20] F. Wu, A. Japaridze, X. Zheng, J. Wiktor, J. W. J. Kerssemakers, and C. Dekker, *Direct imaging of the circular chromosome in a live bacterium,* Nature Communications **10**, 1 (2019).

[21] J. K. Fisher, A. Bourniquel, G. Witz, B. Weiner, M. Prentiss, and N. Kleckner, *Four-dimensional imaging of e. coli nucleoid organization and dynamics in living cells,* Cell **153**, 882 (2013).

[22] N. Hadizadeh Yazdi, C. C. Guet, R. C. Johnson, and J. F. Marko, *Variation of the folding and dynamics of the e scherichia coli chromosome with growth conditions,* Molecular microbiology **86**, 1318 (2012).

[23] G. Mertens, A. Klippel, H. Fuss, H. Blöcker, R. Frank, and R. Kahmann, *Site-specific recombination in bacteriophage Mu: characterization of binding sites for the DNA invertase Gin.* The EMBO Journal **7**, 1219 (1988).

[24] C. A. Ball and R. C. Johnson, *Journal of Bacteriology,* Tech. Rep. 13 (1991).

[25] L. R. Lazarus and A. A. Travers, *The Escherichia coli FIS protein is not required for the activation of tyrT transcription on entry into exponential growth.* The EMBO Journal **12**, 2483 (1993).

[26] A. J. Bokal IV, W. Ross, and R. L. Gourse, *The transcriptional activator protein fis: Dna interactions and cooperative interactions with rna polymerase at theescherichia coli rrnbp1 promoter,* Journal of molecular biology **245**, 197 (1995).

[27] C. A. Hirvonen, W. Ross, C. E. Wozniak, E. Marasco, J. R. Anthony, S. E. Aiyar, V. H. Newburn, and R. L. Gourse, *Contributions of UP Elements and the Transcription Factor FIS to Expression from the Seven rrn P1 Promoters in Escherichia coli,* Journal of Bacteriology **183**, 6305 (2001).

5

[28] S. Stella, D. Cascio, and R. C. Johnson, *The shape of the DNA minor groove directs binding by the DNA-bending protein Fis,* Genes and Development **24**, 814 (2010).

[29] S. Maurer, J. Fritz, G. Muskhelishvili, and A. Travers, *RNA polymerase and an activator form discrete subcomplexes in a transcription initiation complex,* EMBO Journal **25**, 3784 (2006).

[30] G. Muskhelishvili, A. Travers, H. Heumann, and R. Kahmann, *FIS and RNA polymerase holoenzyme form a specific nucleoprotein complex at a stable RNA promoter.* The EMBO Journal **14**, 1446 (1995).

[31] D. Skoko, D. Yoo, H. Bai, B. Schnurr, J. Yan, S. M. McLeod, J. F. Marko, and R. C. Johnson, *Mechanism of Chromosome Compaction and Looping by the Escherichia coli Nucleoid Protein Fis,* Journal of Molecular Biology **364**, 777 (2006).

[32] A. Japaridze, S. Renevey, P. Sobetzko, L. Stoliar, W. Nasser, G. Dietler, and G. Muskhelishvili, *Spatial organization of DNA sequences directs the assembly of bacterial chromatin by a nucleoid-associated protein,* Journal of Biological Chemistry **292**, 7607 (2017).

[33] R. Spurio, M. Dürrenberger, M. Falconi, A. La Teana, C. L. Pon, and C. O. Gualerzi, *Lethal overproduction of the Escherichia coli nucleoid protein H-NS: ultramicroscopic and molecular autopsy,* MGG Molecular & General Genetics **231**, 201 (1992).

[34] R. Brunetti, G. Prosseda, E. Beghetto, B. Colonna, and G. Micheli, *The looped domain organization of the nucleoid in histone-like protein defective Escherichia coli strains,* Biochimie **83**, 873 (2001).

[35] V. S. Lioy, A. Cournac, M. Marbouty, S. Duigou, J. Mozziconacci, O. Espéli, F. Boccard, and R. Koszul, *Multiscale Structuring of the E. coli Chromosome by Nucleoid-Associated and Condensin Proteins,* Cell **172**, 771 (2018).

[36] W. W. Navarre, S. Porwollik, Y. Wang, M. McClelland, H. Rosen, S. J. Libby, and F. C. Fang, *Selective silencing of foreign DNA with low GC content by the H-NS protein in Salmonella,* Science **313**, 236 (2006).

[37] B. Lang, N. Blot, E. Bouffartigues, M. Buckle, M. Geertz, C. O. Gualerzi, R. Mavathur, G. Muskhelishvili, C. L. Pon, S. Rimsky, S. Stella, M. Madan Babu, and A. Travers, *High-affinity DNA binding sites for H-NS provide a molecular basis for selective silencing within proteobacterial genomes,* Nucleic Acids Research **35**, 6330 (2007).

[38] B. R. Gordon, Y. Li, A. Cote, M. T. Weirauch, P. Ding, T. R. Hughes, W. W. Navarre, B. Xia, and J. Liu, *Structural basis for recognition of AT-rich DNA by unrelated xenogeneic silencing proteins,* Proceedings of the National Academy of Sciences of the United States of America **108**, 10690 (2011).

[39] C. Badaut, R. Williams, V. Arluison, E. Bouffartigues, B. Robert, H. Buc, and S. Rimsky, *The degree of oligomerization of the H-NS nucleoid structuring protein is related to specific binding to DNA,* Journal of Biological Chemistry **277**, 41657 (2002).

[40] R. T. Dame, C. Wyman, and N. Goosen, *H-NS mediated compaction of DNA visualised by atomic force microscopy,* (2000).

[41] R. Schneider, R. Lurz, G. Lüder, C. Tolksdorf, A. Travers, and G. Muskhelishvili, *Nucleic Acids Research*, Tech. Rep. 24 (2001).

[42] R. T. Dame, C. Wyman, and N. Goosen, *Structural basis for preferential binding of H-NS to curved DNA,* Biochimie **83**, 231 (2001).

[43] O. Schröder and R. Wagner, *The bacterial DNA-binding protein H-NS represses ribosomal RNA transcription by trapping RNA polymerase in the initiation complex,* Journal of Molecular Biology **298**, 737 (2000).

[44] E. Bouffartigues, M. Buckle, C. Badaut, A. Travers, and S. Rimsky, *H-NS cooperative binding to high-affinity sites in a regulatory element results in transcriptional silencing,* Nature Structural and Molecular Biology **14**, 441 (2007).

[45] C. Kahramanoglou, A. S. Seshasayee, A. I. Prieto, D. Ibberson, S. Schmidt, J. Zimmermann, V. Benes, G. M. Fraser, and N. M. Luscombe, *Direct and indirect effects of H-NS and Fis on global gene expression control in Escherichia coli,* Nucleic Acids Research **39**, 2073 (2011).

[46] M. Shin, A. C. Lagda, J. W. Lee, A. Bhat, J. H. Rhee, J.-S. Kim, K. Takeyasu, and H. E. Choy, *Gene silencing by H-NS from distal DNA site,* Molecular Microbiology **86**, 707 (2012).

[47] Y. Liu, H. Chen, L. J. Kenney, and J. Yan, *A divalent switch drives H-NS/DNA-binding conformations between stiffening and bridging modes,* Genes and Development **24**, 339 (2010).

[48] H. Afflerbach, O. Schröder, and R. Wagner, *Conformational changes of the upstream DNA mediated by H-NS and FIS regulate E. coli rrnB P1 promoter activity,* Journal of Molecular Biology **286**, 339 (1999).

[49] C. J. Lim, S. Y. Lee, L. J. Kenney, and J. Yan, *Nucleoprotein filament formation is the structural basis for bacterial protein H-NS gene silencing,* Scientific Reports **2**, 1 (2012).

[50] M. V. Kotlajich, D. R. Hron, B. A. Boudreau, Z. Sun, Y. L. Lyubchenko, and R. Landick, *Bridged filaments of histone-like nucleoid structuring protein pause RNA polymerase and aid termination in bacteria,* eLife **2015** (2015), 10.7554/eLife.04970.

[51] S. Maurer, J. Fritz, and G. Muskhelishvili, *A Systematic In Vitro Study of Nucleoprotein Complexes Formed by Bacterial Nucleoid-Associated Proteins Revealing Novel Types of DNA Organization,* Journal of Molecular Biology **387**, 1261 (2009).

[52] H. G. Hansma, *Surface biology of dna by atomic force microscopy,* Annual Review of Physical Chemistry **52**, 71 (2001).

5

[53] H. G. Hansma, R. L. Sinsheimer, M.-Q. Li, and P. K. Hansma, *Atomic force microscopy of single-and double-stranded dna,* Nucleic acids research **20**, 3585 (1992).

[54] Y. L. Lyubchenko, L. S. Shlyakhtenko, and T. Ando, *Imaging of nucleic acids with atomic force microscopy,* Methods **54**, 274 (2011).

[55] P. I. Chang, P. Huang, J. Maeng, and S. B. Andersson, *Local raster scanning for high-speed imaging of biopolymers in atomic force microscopy,* Review of scientific instruments **82**, 063703 (2011).

[56] C. Dekker, *Solid-state nanopores,* Nature nanotechnology **2**, 209 (2007).

[57] R. K. Sharma, I. Agrawal, L. Dai, P. S. Doyle, and S. Garaj, *Complex dna knots detected with a nanopore sensor,* Nature communications **10**, 1 (2019).

[58] C. Plesa, D. Verschueren, S. Pud, J. van der Torre, J. W. Ruitenberg, M. J. Witteveen, M. P. Jonsson, A. Y. Grosberg, Y. Rabin, and C. Dekker, *Direct observation of dna knots using a solid-state nanopore,* Nature nanotechnology **11**, 1093 (2016).

[59] G. V. Soni and C. Dekker, *Detection of nucleosomal substructures using solid-state nanopores,* Nano letters **12**, 3180 (2012).

[60] A. I. Lamond and A. A. Travers, *Requirement for an upstream element for optimal transcription of a bacterial tRNA gene,* Nature **305**, 248 (1983).

[61] J. Gowrishankar, *Journal of Bacteriology,* Tech. Rep. 1 (1985).

[62] W. Yang, L. Restrepo-Pérez, M. Bengtson, S. J. Heerema, A. Birnie, J. Van Der Torre, and C. Dekker, *Detection of CRISPR-dCas9 on DNA with Solid-State Nanopores,* Nano Letters **18**, 6469 (2018).

[63] C. Plesa, S. W. Kowalczyk, R. Zinsmeester, A. Y. Grosberg, Y. Rabin, and C. Dekker, *Fast translocation of proteins through solid state nanopores,* Nano letters **13**, 658 (2013).

[64] W. Nasser and S. Reverchon, *H-NS-dependent activation of pectate lyases synthesis in the phytopathogenic bacterium Erwinia chrysanthemi is mediated by the PecT repressor,* Molecular Microbiology **43**, 733 (2002).

[65] T. Lautier and W. Nasser, *The DNA nucleoid-associated protein Fis co-ordinates the expression of the main virulence genes in the phytopathogenic bacterium Erwinia chrysanthemi,* Molecular Microbiology **0**, 071119190133007 (2007).

[66] C. Plesa and C. Dekker, *Data analysis methods for solid-state nanopores,* Nanotechnology **26** (2015).

6

TRANSLOCATION OF DNA THROUGH ULTRATHIN NANOSLITS

Two-dimensional (2D) nanoslit devices, where two crystals with atomically flat surfaces are separated by only a few nanometers, have attracted considerable attention because their tunable control over the confinement allows for the discovery of unusual transport behavior of gas, water, and ions. Here, we study the passage of double-stranded DNA molecules through nanoslits fabricated from exfoliated 2D materials, such as graphene or boron nitride, and examine the DNA polymer behavior in this tight confinement. We observe two types of events in the ionic current: long current blockades that signal DNA translocation and short spikes where DNA enters the slits but withdraws. DNA translocation events exhibit three distinct phases in their current-blockade traces – loading, translation, and exit. Coarse-grained molecular dynamics simulation allows us to identify the different polymer configurations of these phases. DNA molecules, including folds and knots in their polymer structure, are observed to slide through the slits with near-uniform velocity without noticeable frictional interactions of DNA with the confining graphene surfaces. We anticipate that this new class of 2D-nanoslit devices may be used for studying polymer physics and lab-on-a-chip biotechnology.

6.1. Introduction

The translocation of biopolymers through nanoscale constrictions such as pores and channels has inspired a new class of lab-on-a-chip sensors that can sense, sort, and process DNA, RNA, and proteins for diagnostics and sequencing applications [1–4]. In particular, nanopores have been used abundantly for biophysics studies and DNA sequencing [5], while lab-on-a-chip platforms allow extensive microfluidic integration of different sensors and reactions [6]. Such methods require nanoscale manipulation and an understanding of the physics governing the transport of biopolymers. Despite decades of research with efforts to design and fabricate different geometric confinements [7] to probe various aspects of the transport process, the fundamentals of the biopolymer transport phenomena through artificial nanochannels have not been fully resolved. One challenge is the multitude of forces involved in the transport process on the nanoscale. Molecular transport is driven by the interplay of entropic, electroosmotic, and electrophoretic forces experienced by the biopolymers [7–12]. For example, nanoconfinement-induced entropic barriers hinder the insertion of large DNA polymer coils driven by the electrophoretic force into much smaller nanopores and channels that can be as small as the length scale of natural biochannels and porins. Another challenge lies in mimicking smooth and atomically precise surfaces that would allow researchers to disentangle the intrinsic polymer behavior from surface interactions [13]. Silicon nitride/oxide-based substrates have been extensively used for nanofluidic channels to translocate biopolymers, but they suffer from significant (few nm root mean square (rms)) surface roughness and inhomogeneous surfaces [14–16]. Attempts with carbon nanotubes (CNTs), which feature smooth inner surfaces, face challenges of device integration and leakage due to the stringent requirements of a perfect seal as well as a lack of systematic control of the channel length and diameter [17–19]. Until recently, it was impossible to fabricate individual artificial channels with atomic scale dimensions or even subnanometric size tunable nanofluidic devices which has hindered the further development of the field [20].

Here we report the first study of DNA transport through two-dimensional (2D) nanoslits with precisely designed dimensions and atomically smooth surfaces [21]. The nanoslits were fabricated using exfoliated 2D materials such as graphene or hexagonal boron nitride (hBN). They were assembled in a trilayer stack (Fig.6.1a), where the basal planes of the two crystals (top and bottom) provide atomically flat walls, while the third crystal with a precise controlled thickness serves as a spacer layer that separates these walls. The height of the confinement was determined by the thickness of the spacer layer that can be set at any value from a monolayer (0.34 nm) to tens of nanometers. The entire crystal can then be etched down to the desired length of the slit. Entry and exit to the slits were provided through out-of-plane bulk access reservoirs. Previous studies have demonstrated remarkable water-, ion-, and gas-transport properties [21–23] of such devices. Furthermore, the surface properties and chemical interactions of such nanoslits can be tuned for studying various surface interactions and sensor applications. Exploration of the DNA transport properties through nanoslits may experimentally answer questions about the strength of DNA-graphene interactions hypothesized by many previous studies [1, 24–26] and allow studies of DNA in strongly confined 2D slits on scales not previously probed by conventional nanofluidic devices.
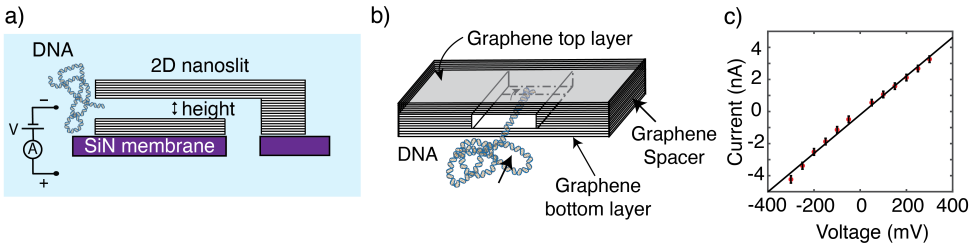
Figure 6.1: **DNA translocation through 2D-nanoslit devices.** a) Cross-sectional view of a 2D-nanoslit device in the DNA translocation setup. DNA is introduced from the cis (negatively biased) side and a positive voltage is applied to drive the DNA through the slit. b) Oblique-view schematic of the 2D nanoslit. The device is made by sandwiching graphene spacers between top and bottom layers of graphite crystals to form an atomically smooth surface within the slit. Graphene spacer defines the height of the device to an accuracy of a single layer – 0.34 nm. The entire graphene crystal was then masked and etched perpendicularly to define the length of the slit. The final device geometry was w= 110 nm, h= 6.5 nm, l= 400 nm. c) Typical I-V curve of our 2D-nanoslit device at 1M LiCl. The conductance is linear across this range. The measured conductance of our graphene device is 1.2 x 10^{-8} S.

6.2. FABRICATION AND RESULTS

The 2D-nanoslit devices were fabricated following the procedure previously outlined by Keerthi et al. [22] (for details, see SI). Schematically, the device is represented in Fig.6.1b. The spacer that controls the height of the nanoslit is made from few-layer thick graphene. To smooth out any roughness coming from the supporting SiN surface, thicker stacks of graphene (~20-30 nm) were used as the bottom and top crystals. The length, width, and height, of the major 2D-nanoslit device that we here report on was l = 400 nm, w = 110 nm, h = 6.5 nm, respectively (for other devices, see SI). To facilitate the detailed detection and analysis of translocation events of individual DNA molecules, our device contained only a single nanoslit. First, using 1M LiCl solution, we checked that the current-voltage characteristic was linear across the +300 to -300 mV range (Fig. 6.1c). From the slope of the I-V graph, we measured a slit conductance of 1.2 x 10^{-8} S – in line with the expected conductance of 1.9 x 10^{-8} S as estimated from the bulk ionic conductivity and geometric size. The 2D-nanoslit devices could be filled properly and did not show intrinsic instabilities. When left at a constant voltage (300 mV), the device showed a stable open slit current for many hours. The devices were extremely stable and could be used for weeks. For the DNA translocation experiments, the initial salt solution was replaced with 4M LiCl in order to increase the signal-to-noise resolution of the currents [27].
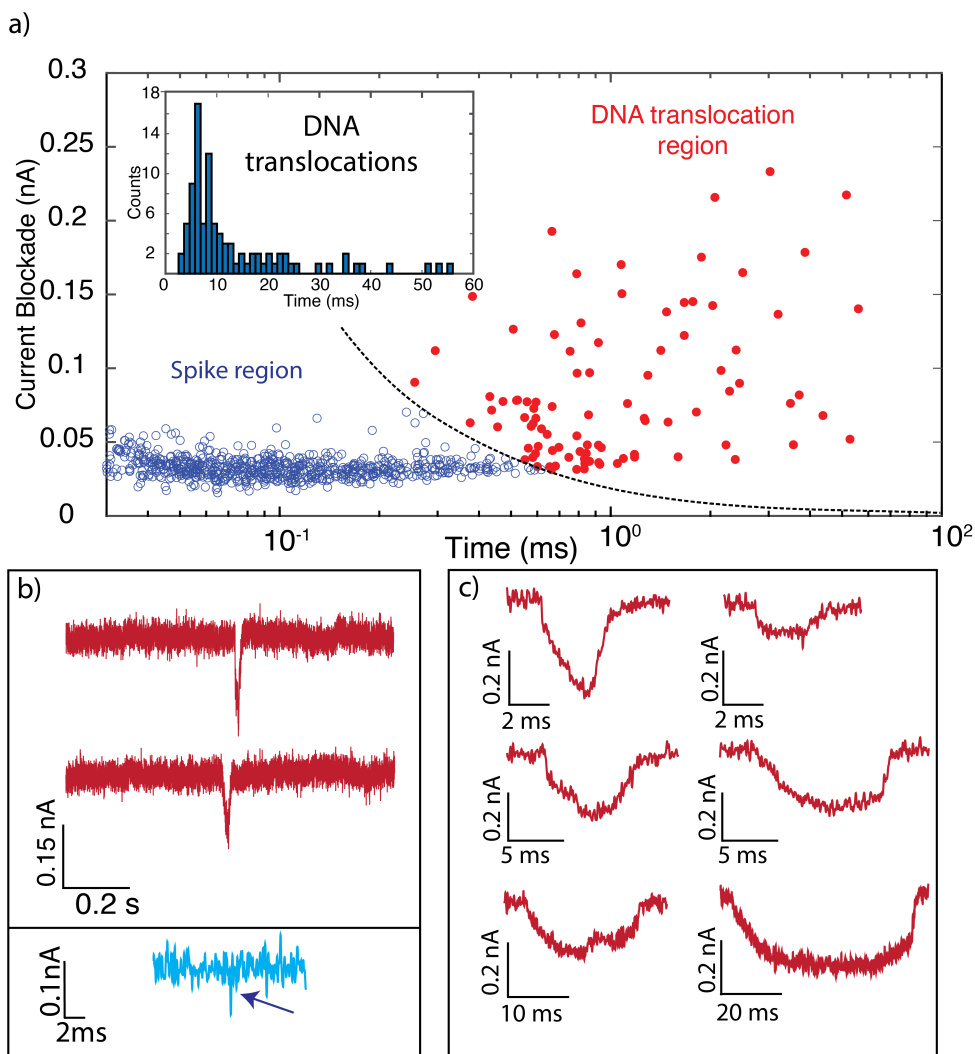
Figure 6.2: **Current blockades produced by DNA in 2D-nanoslit devices.** a) Scatter plot of the average current blockade versus the time of DNA events. Two regions can be seen – DNA translocation region which is marked by deep current blockades and long passage times (red). The inset shows a histogram of the event duration, with a median at 8.4 ms. The second region is the spike region (blue) marked by small current blockades and fast dwell times. b) Representative current traces for DNA translocation events (top panel, red) and a spike event (bottom panel, blue). We interpret the latter events as DNA probing the entrance of the slit but withdrawing due to entropic force. Data were filtered with a 3 kHz low pass filter. c) Six representative current traces produced by DNA translocation. The traces have an armchair shape and vary in the length and depth of the current blockades.

Upon addition of DNA (5 kbp, linear dsDNA) to the entry (cis, negative voltage-biased) side of the device, we observed clear temporary reductions in the ionic current through the 2D-nanoslit device at 300 mV. As is well known from the field of nanopores, such current events indicate the presence of DNA in the slit [28]. Events are characterized by their average blockade current and the time that the DNA spends within the slit. Fig. 6.2a plots these quantities in a scatter plot (N=796), where each dot represents a separate single-molecule event collected from our graphene device with the dimensions reported in the preceding paragraph (l = 400 nm, w= 110nm, h=6.5nm). Two main populations appear: a first one that we attribute to the translocation of DNA through the slit (termed 'DNA translocation region'), and a second region that comprises of much faster transient events (termed 'spike region'). These two populations of events are separated by a threshold value that is set, similar to DNA events in nanopore experiments [29], as a fraction of integrating the average current blockade level over the total time of the event (0.2 nA*ms). We interpret the high-amplitude (above threshold) dips in the current trace with a long passage of time (>1 ms) as events where the DNA molecule fully translocates through the slit. Here, DNA is electrophoretically driven across the slit, temporarily displacing ions within the slit, which leads to a drop in the measured current. This process is directly analogous to the blockade of the ionic current in solid state nanopores upon passage of DNA, but the dips are much longer here (tens of milliseconds versus ~0.5 ms for nanopores) owing to the length of the 2D-nanoslit which exceeds the typical nanopore channel length by about two orders of magnitude. Example current traces are shown in Fig.6.2b, c where we see individual dips that last from a few ms to more than 60 ms. Translocation times were broadly distributed, with a median translocation time of 8.4 ms (Fig.6.2a insert).

Closer examination of the DNA translocation events showed that most events had a characteristic armchair-like shape, displayed in the example events of Fig.6.2c, with a linear rise, plateau, and a linear decay. The rise, dwell, and fall times as well as the maximum blockade amplitude reached during the event varied vastly. The blockade current ranged between 0.5-1% of the open slit current, and a large spread in the total dwell time and average blockade current was observed (over 2 orders of magnitude in time and between 0.07-0.3 nA). We hypothesize that these variations originate from different number of DNA loops that were captured from the randomly oriented polymer blob and simultaneously translocated through the nanoslit – a scenario that we will further examine below. Remarkably, we did not see any clogging of the 2D-nanoslit devices and devices remained stable for hours showing clear DNA translocations, suggesting that any interactions of the DNA with the graphene surface were transient in nature.

Turning to the second population of observed events (Fig.6.2b, spikes), these events had a distinctive spike-like shape and exhibited smaller blockade current amplitudes and shorter dwell times. We interpret these blockades as transient excursions of DNA into the entrance of the nanoslit that did not result into complete translocations, but rather, the DNA withdrew back into the entry reservoir. Similar phenomena have been reported in a variety of nanofluidic experiments with microslits, nanopores, and other micro- or nanofluidic devices that presented an entropic barrier to polymer entry [11, 30, 31]. A polymer can access way less configurations within a narrow slit than in free solution, and hence the entry into the slit presents an entropic barrier. This barrier will

be lower for slits with taller heights (h) and for shorter DNA [32]. Shorter DNA therefore is expected to yield more translocation events. Additional experiments with DNA of different lengths, 10 and 1 kbp, in nanoslits of similar dimensions (see SI) provided support for this: while the 10 kbp DNA exhibited no translocation events but instead exclusively probing spike events, abundant translocation events were observed when 1 kbp DNA was used (see SI).

6.2.1. SIMULATIONS AND DISCUSSIONS

In order to evaluate the DNA translocation process in microscopic detail, we simulated the DNA translocation through graphene slits using a coarse-grained molecular dynamic approach. The device geometry and size, driving voltages, and salt conditions from the experiments were all recreated in the simulation setup (Fig.6.3a). Our simulations employed a custom coarse-grained model of DNA [33] and represented the graphene nanostructure as a frictionless repulsive potential. Prior to translocation, a 5kbp DNA molecule was equilibrated in the 160 nm x 110 nm x 500 nm entry reservoir near the entrance of the slit to generate a random starting configuration of the DNA. A three-dimensional (3D) electrostatic potential, as determined from continuum calculations, was applied to drive the DNA through the nanoslit. Indeed, the DNA was captured into and translocated through the slit. Instantaneous DNA conformations were used to compute the blockade current using a steric exclusion model [34]to build up a current profile of the entire event. Note that, as is generally found [35], the molecular dynamics simulations are typically faster than the nominal timescales by several orders of magnitudes and thereby cannot directly be compared to the dwell times in actual experiments. Fig.6.3b shows three typical current trace obtained from a simulation of a DNA translocation (See SI more examples from simulations).
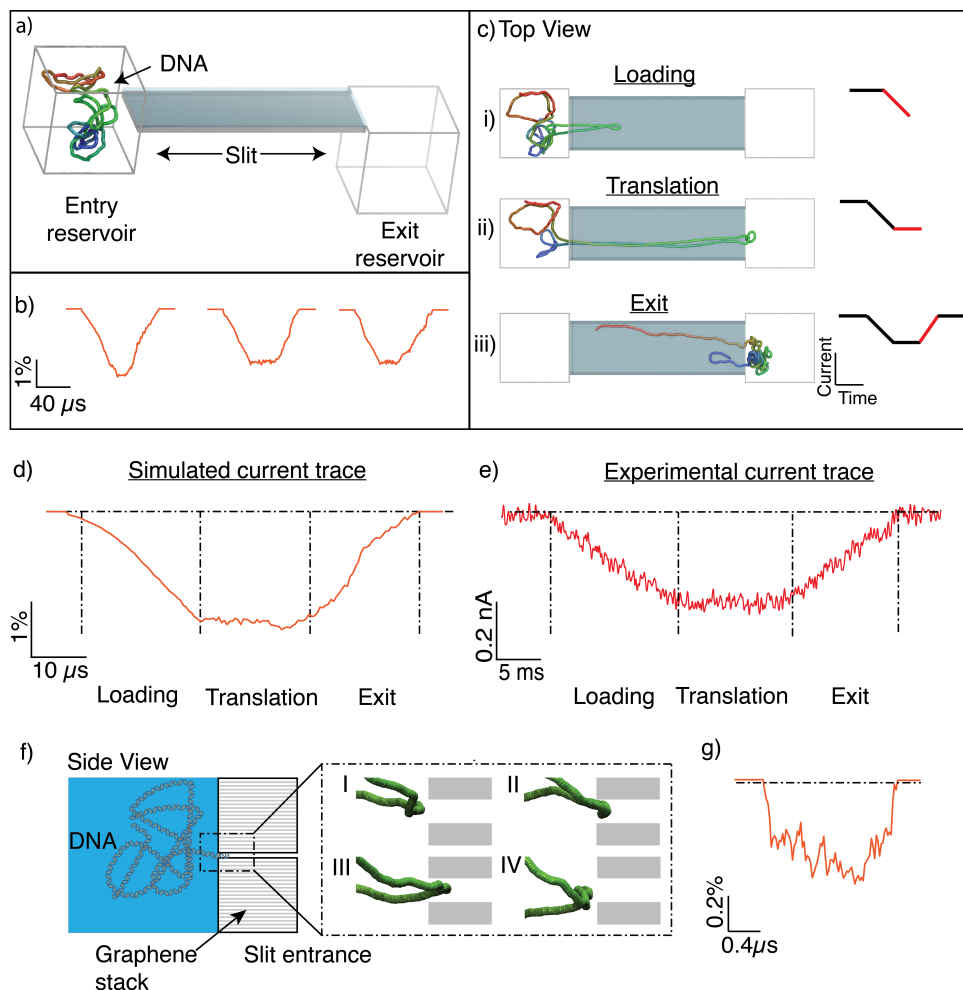
Figure 6.3: **MD simulation of DNA translocation through a 2D nanoslit.** a) To-scale coarse-grained model of the experimental 2D-nanoslit device. b) Ionic-current-blockade traces obtained from the simulations of DNA translocation through the slit at 1V. Events typically showed a 1-2% change of the open slit current and had an armchair shape (See SI for other simulation runs). c) Video stills from one simulation trajectory showing the three stages of a DNA translocation event – loading, translation and exit – and the corresponding three regions in the armchair current blockade. d) Zoomed-in view of a simulated current blockade trace at 1V. e) Zoomed-in view of an experimental current blockade trace that matches the armchair shape of the simulated current trace well. f) Snapshots of a simulation showing the DNA polymer exploring and probing the entrance of the slit at four different time points. g) Current-blockade signal for a DNA probing event. Similar to experimentally obtained traces, the current blockade shows up as quick spikes with a low current-blockade amplitude.

Current traces typically showed a 1-2% decrease relative to the open slit current and generally had an arm-chair shape. Video stills captured at three different time points (Fig.6.3c) illustrate different stages of the DNA translocation process, which we can directly relate to the current traces obtained from the experiment. The gradual entry of DNA into the slit decreases the current ('loading') until the leading segment exits the slit. From that point on, the amount of DNA in the slit remains approximately constant leading to a plateau in the current blockade ('translation'). Eventually, the trailing segments of the DNA enter the slit to translocate as well, which leads to a return to the open slit current ('exit'). Taken together, our simulations reproduce and explain the typical arm-chair shape of current blockade traces (Fig.6.3d) that was observed in the experiments (Fig.6.3e and 6.2c).

The simulations also allowed us to investigate the capture process of the DNA in greater detail. Upon initialization of the simulation, the DNA did not immediately get captured into the slit for translocation even under a strong applied voltage. Instead, segments of the DNA were observed to probe the entry of the slit with a partial insertion which subsequently retracted back into the reservoir, a phenomenon that occurred repeatedly. Fig.6.3f shows four video stills from such a process. Eventually, the DNA overcame the entropic barrier and fully translocated through the slit. Fig.6.3g shows the calculated current for such probing processes. Generally, much smaller blockade currents (<0.3% of the open slit current) were observed for the probing event that lasted much shorter than complete translocations. These findings match well with the results obtained from the experiments in the spike region.

The DNA transits from a 3D configuration in the polymer blob at the entrance of the slit to a significantly confined arrangement in the slit, as the slit height is much less than the persistence length of DNA (i.e. DNA persistence length ~50nm, slit height ~6.5 nm) which forces DNA into a 2D configuration. We were able to observe the capture and translocation of DNA features such as folds, loops, and knots in our simulations. For example, a series of video stills (Fig.6.4a) shows a DNA loop, which formed spontaneously upon the DNA capture, translocating through the slit (as marked by the dashed red box). The observation of such features is surprising as one might think that forces (i.e. the combination of electrophoretic, entropic, and frictional surface-interaction forces) in the translocation process would pull the DNA taut and smooth out any of these features. Contrary to such expectations, loops did not unfold or get stretched out by forces experienced by the DNA during the translocation process, but instead appeared to 'slide' through the slit without much internal rearrangements.

To gain a more quantitative understanding of the translocation dynamics of folds in the DNA, we plotted the displacement versus time curve separately for each of the subsequent 100bp segments comprising the DNA molecule (Fig.6.4b). Three such DNA segments are highlighted in particular, the leading DNA segment (the segment that first entered the slit), the middle segment (halfway during the translocation process), and the trailing segment (last segment of DNA that entered the slit). Neighboring segments are observed to have rather similar displacement curves, which indeed acts to preserve particular DNA features such as a loop or a fold throughout the translocation, as the segments slide together along the nanoslit in a frictionless manner with a near-constant velocity. Second, while the first strand always gets pulled into the slit from a volume near
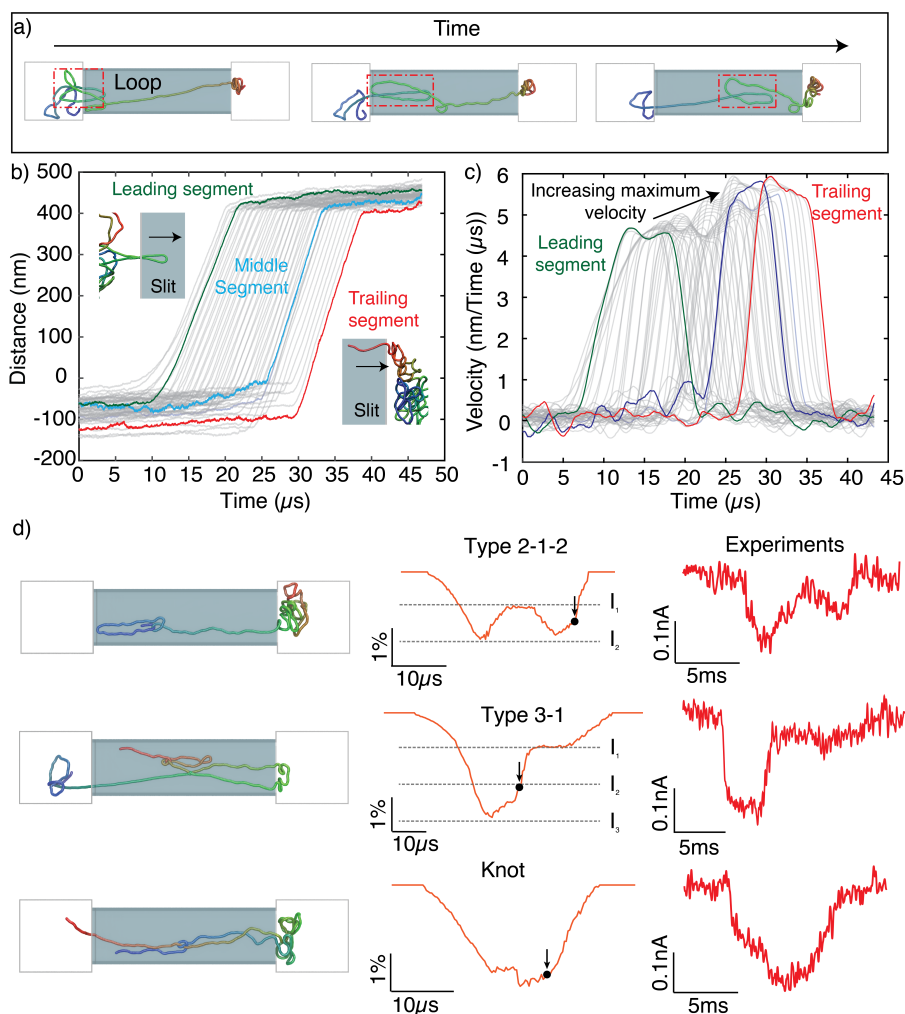
Figure 6.4: **DNA dynamics in 2D-nanoslit.** a) Video stills of a DNA loop translocating through the 2D nanoslit (top view). Upon capture into the slit, folds and loops along the DNA polymer chain (shown in the red dotted rectangle) are preserved throughout the entire translocation event. b) Distance versus time curves for every 100 bp segments along the same DNA molecule. The origin of the Y axis is defined to be at the entrance of the slit. Three segments are highlighted to show the general trend: green – leading segment, i.e., first segment of DNA to enter the nanoslit; cyan– middle segment; and red – trailing segment, the last one to enter the slit. Segments that were close together did not vary much in their displacement, which preserved local DNA conformations, such as loop and folds, throughout the translocation. c) Calculated velocity of DNA during the translocation. The maximum velocity increases for the trailing segments of the DNA. d) Snapshots illustrating the diversity of DNA polymer conformations in the simulations and the corresponding ionic current traces. Video stills correspond to the time point marked by the arrow in the current trace (full videos in the SI). Similar current traces were experimentally observed in the translocation measurements, confirming that complex DNA conformations can translocate through the 2D nanoslit without becoming unraveled.

the slit entrance, later segments are pulled in from further out of the reservoir (negative distances denote distances away from the slit into the entry reservoir, Fig.6.4b). The plot of the segment's velocities (Fig.6.4c) shows that nearby segments travel through the slit at nearly the same speed, suggesting that they experienced similar forces. However, there is a noticeable (~25%) increase in the maximum velocity that is attained by the segments towards the end of the DNA event. This can be attributed to a decrease in the amount of the DNA that still is residing in the entry reservoir before the slit, as more and more DNA is unwounded and loaded into the channel, yielding a reduced drag arising from pulling the remaining polymer blob and hence an increased velocity for the DNA translocating through the slit. We note that this drag force is the only observed factor affecting the otherwise near constant velocity transport of the DNA.

Armed with these microscopic insights, we are able to explain almost all features seen in the experimental current traces. We returned to the experiments and realized that the large variation in amplitudes reached by the different current traces are likely due to the presence of a varying number of folds, loops, or knots in the DNA polymer that reside within the slit [36, 37]. Current traces from the simulations gave us hints on how to identify such features, e.g. an abrupt change in the current level. We illustrate this with three event types from the simulations in Fig.6.4d, with corresponding experimental traces that exhibit the same profile in the current blockade (full videos are provided in the SI). First, current traces often exhibited multiple plateau levels, for example the one in Fig.6.4d top (denoted 2-1-2 event) where the current started with a plateau level that subsequently decreased by a factor of 2, to subsequently return to the plateau value again. These events are due to DNA that is translocating in a folded manner before straightening out into a single helix segment in the middle of the event. This in fact can be used to identify the blockade level of an individual double stranded DNA molecule, to characterize and sort the rest of the translocation events, such as the 3-1 event shown in Fig.6.4d where a large DNA segment made of multiple folds slides along the channel middle (see SI for the categorization of the events). Indeed, we also observed such 3-1 events in the experimental traces, which suggests an interaction-free surface of our 2D-nanoslits that allows these features to slide through. We also observed the translocation of a single DNA knot (Fig.6.4d) which shows up as an abrupt half-unit step in both the simulation and experiment current traces.

Taken together, these traces indicate that the dominating force during the translocation is the electrophoretic force that acts equally on the entire DNA polymer that resides within the slit. This allows loops and folds to translocate through without being pulled internally and relaxed. It is remarkable that these features persist even under the extreme slit-like confinement (6 nm) for at least 10 milliseconds, a confinement and time regime not probed by conventional nanofluidic experiments. We do not observe any evidence of graphene-DNA interactions, contrary to other graphene devices [24–26]. Additional experiments in hBN nanoslits show similar translocation profiles as the events obtained from graphene devices, suggesting that the translocation of DNA is dominated by the electrophoretic driving force and slides along the atomically smooth surface (as shown by AFM characterisation reported in the SI). In a liquid environment, the graphene surface may pick up a slight negative surface charge from residual OH^- groups which however will be readily screened by Li^+ ions in the high-salt buffer [38], resulting in weak

DNA-graphene interactions. The discrepancy with other reported graphene-DNA interaction may arise from the conventionally followed fabrication protocols in the literature that damage the graphene sheets, allowing for defect sites to interact with dsDNA [39–41], whereas our approach directly benefits from the atomically flat graphene planes of the exfoliated 2D materials which are not post-processed.

6.3. CONCLUSIONS

In summary, we studied translocation of DNA molecules through ultrathin nanoslits fabricated from 2D materials. Remarkably we did not require to apply any additional coating to overcome the clogging that is commonly reported in graphene nanopore devices, and our devices remained stable for hours [42]. Clear changes in the ionic current allowed us to identify three distinct phases of DNA translocation, namely loading, translation, and exit. The entry process is dominated by the entropic cost of confining the DNA into the 2D slit. Coarse-grained simulations provided a microscopic picture that was fully consistent with the experimentally obtained ionic current traces. Neighboring segments of the DNA slid together and translocated with the same velocity in a near-frictionless manner. Towards the end of the translocation, DNA segments faced a weaker retarding force due to the lower amount of DNA residing outside the entrance, thereby yielding higher translocation velocities. The weak forces involved in the translocation process did not stretch the DNA during translocation but allowed folds and knots to persist inside the slit. The folds and knots slid through the entire length of the nanoslit suggesting that interactions with the graphene surface are transient and weak.

Looking ahead, the 2D nanoslits provide a novel tool for probing biopolymer properties as they constitute a precisely engineered confinement with atomically smooth surfaces. We envision that the use of optically transparent 2D materials should allow future 2D nanoslit devices to be integrated with optical microscopy for fluorescence-based nanofluidic experiments. Such devices can be used to probe the evolution of DNA knots and folds under confinement with low surface interactions. An obvious next step for future investigations will be to study the interplay of entropy and polymer configuration under ultrahigh confinement by varying the height of the slits and the length of DNA in different salt concentrations and voltages. This may pave the way for future 2D sensing devices that can, for example, be used to separate different lengths of biopolymers. Furthermore, the use of these frictionless 2D nanoslits can be expected to shed light on the basic physics of biopolymer transport.

6

6.4. METHODS

6.4.1. DNA-SENSING EXPERIMENTS

2D nanoslit devices were loaded in a PEEK (Polyether ether ketone) flow cell. We used Ag/AgCl electrodes and an Axopatch 200B amplifier (Molecular Devices) for current detection. The traces were recorded at 100kHz and further low pass filtered at 5kHz for with the Transanalyzer Matlab package [43].

For the DNA sensing experiments, 5 μL of 500ng/μL of the stock solution (NoLimits Individual DNA Fragments, Thermo Fisher Scientific) was pipetted into the negatively-biased cis compartment of the flow cell containing 500μL of 4M LiCl solution (buffered with 40mM Tris-HCl, 4mM EDTA, pH 8). We used LiCl to maximise the translocation time and signal-to-noise (SNR) ratio as is commonly done in ionic sensing measurements. Li ions can bind strongly to the negative backbone of the DNA, screening most of the charge, and hence decreasing the electrophoretic force on the DNA [27]. This diluted the DNA to a final concentration of 1ng/μL in the reservoir. The DNA was electrophoretically driven through the slit with a bias voltage of 300mV and detected by measuring changes in the current flowing through the 2D slit.

6.4.2. MD SIMULATION

All simulations of dsDNA translocation through the nanoslit were performed using the Atomic Resolution Brownian Dynamics (ARBD) package [44]. COMSOL software (COMSOL Multiphysics 5.3a) was used to obtain the electrostatic potential that was applied in ARBD. Prior to translocation simulations, a 5000-bp DNA strand was equilibrated in a 160 nm3 volume using a multi-resolution simulation protocol [33] to create different DNA conformation. These conformations were then used to initialise the simulations of the dsDNA translocation. The pre-obtained electrostatic potential was then used to drive the DNA into the slit and begin the translocation process.

6.5. Supporting Information

6.5.1. Fabrication of 2D nanoslit devices

The fabrication procedure was originally reported in Keerthi et al [22] and modified for our single channel device.

Preparation of SiN membrane: We prepared a free-standing silicon nitride (SiNx) membrane with dimensions of about 50 μm × 100 μm using photolithography and wet etching, starting with a standard silicon (Si) wafer covered with 500 nm-thick layer of SiNx on both sides. A narrow rectangular hole (300 nm x 20 μm) was drilled by focused ion beam (FIB) on the free-standing SiNx membrane which is pre-coated with 10 nm aluminium on both sides of the membrane. Aluminium coating helped to alleviate the charging of the insulating SiNx membrane. After drilling the hole, the aluminium was removed by treating the SiNx wafer with alkaline solution (Microposit®MF319 developer). Following this, the membranes were exposed to oxygen plasma for 3 mins to clean the surface.

Patterning and etching of graphene slit: In the next step, a mechanically exfoliated thin (5 to 6.5 nm, error 0.1 nm) crystals of graphite were prepared on an oxidized Si wafer (300 nm of SiO$_2$). These crystals were then patterned and etched to make one long slit of 110 nm width. Extra nanocavities were created perpendicular to the main 2D-slit to prevent the formation of contamination bubbles formed from collected hydrocarbon contaminants during the self-cleansing process that happens when two 2D-crystals are placed on top of each other, as reported previously [45]. These cavities were perpendicular to the main channel and did not contribute to DNA translocation through the final devices. Pattering was done by electron-beam lithography using polymethyl methacrylate (PMMA) as a resist and oxygen plasma to etch away graphite. The PMMA mask was removed by mild sonication in acetone. The resulting patterned spacer crystal were transferred on to a bottom layer (around 20-30 nm thick graphite or hexagonal boron nitride, h-BN) on another oxidized Si wafer. Transfer of graphene stack: The double layer stack of bottom and spacer layers was transferred together by a wet transfer method, onto the previously made FIB milled aperture on the SiNx membrane as shown in Fig. S1- Step1a. Following the transfer, the hole was extended into this stack by dry etching from the underside of the SiNx/Si wafer (Fig. S6.5- Step1b). To this end, dry etching with oxygen plasma was used for graphite, whereas h-BN was etched in a mixture of CHF3 and oxygen.

Sealing of graphene slits: In the next step, a relatively thick (150 nm) crystal of h-BN/graphite was chosen as the top layer. For the case of graphite 2D slits, the top graphite crystal was covered with another hBN crystal (50 nm thick) which will later be used as a mask for a later etching step. The top layer was precisely transferred on top of the bottom and spacer stack so that it covers the FIB rectangular aperture and overlapped with the 2D-slit (Fig. S6.5- Step2a). After each transfer, the substrate was annealed in 10% hydrogen-in-argon at 400°C for 5 h. The annealing steps are essential for the cleanliness of the final devices and to avoid the clogging 2D slits with PMMA residues and other contaminants from the fabrication processes.

Defining the length of the channel: To define the desired length (L) of the 2D-slit in the final device, we used another step of e-beam lithography. After the pattern writing, the PMMA was used as mask to etch away top and bottom layers using dry-etching methods (Fig. S1- Step3). In the case of graphite 2D-slit devices, first, hBN present on the top graphite layer was etched, and using this hBN as a mask, graphite layers of remaining top, spacer and bottom crystals were etched. After etching, the PMMA was removed by dry etching. The final devices were annealed at 400 °C for 5 hrs (Fig. 6.5- Step4) and stored in DI water.
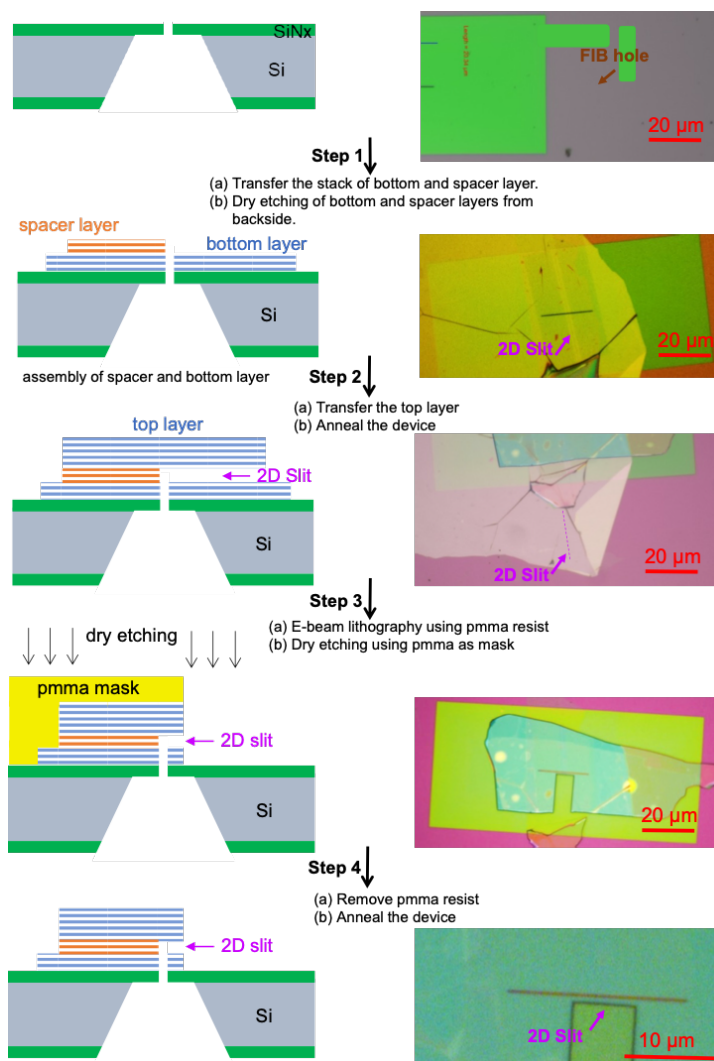
Figure 6.5: **Device fabrication flow chart.** Fabrication of 2D nanoslit devices is illustrated.

6.5.2. AFM PROFILE OF A 2D NANOSLIT
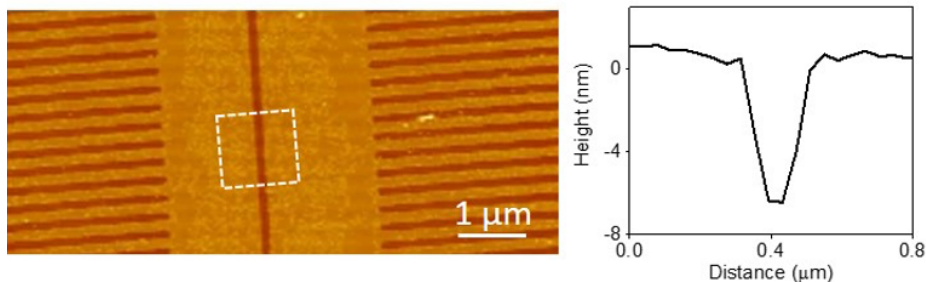
Figure 6.6: **AFM line profile of nanoslit.** An AFM line profile across an open 2D nanoslit device (before the top layer is transferred), showing the low (< 1 nm) RMS roughness. The height profile is taken from the area shown in the dotted white box. The perpendicular nanocavities for the collection of contaminants can be seen in the image.

6.5.3. MOUNTING AND WETTING PROCEDURE FOR THE 2D NANOSLIT
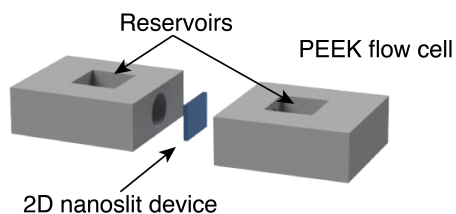
Figure 6.7: **Schematic of PEEK flow cell used to mount 2D nanoslit.** The 2D nanoslit device was mounted in a PEEK flow cell containing two large reservoirs (500μl in volume). For the wetting procedure, the following order was used. First, the device was rinsed with EtOH and gently blow-dried with a N2 gun. The device was then mounted into the PEEK flowcell. To help with the wetting of the 2D nanoslit, the following order of solution were used. First, the reservoirs were filled with 100% Ethanol. The Ethanol solution was then replaced by a solution containing 50% Ethanol and 50% MiliQ. That solution was then replaced by MiliQ several times (2-3 times) to ensure that all ethanol was removed from the reservoirs in order to prevent precipitation of DNA. Finally, the MiliQ was replaced by the desired salt solution (1,2,4 M LiCL). An Ag/AgCl electrode was inserted into each of the reservoir and connected to an Axopatch 200B amplifier (Molecular Devices) and the conductance of the slit was measured. The entire wetting procedure was repeated until the device obtained the expected conductance for the given geometry of the fabricated 2D nanoslit.

6.5.4. ADDITIONAL SAMPLE EVENTS OF DNA TRANSLOCATION IN 2D NANOSLIT
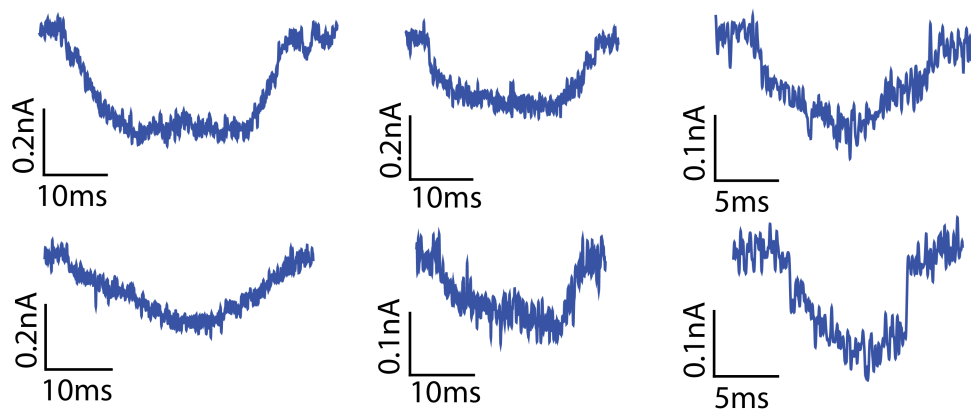
Figure 6.8: **Additional sample events of DNA translocation in 2D nanoslit** Additional DNA translocation event from the experiments in (300mV, 4M LiCl).

6

6.5.5. DNA TRANSLOCATION IN hBN 2D NANOSLIT

GM7 - 1 micron, 6nm, 116nm, 2M LiCL
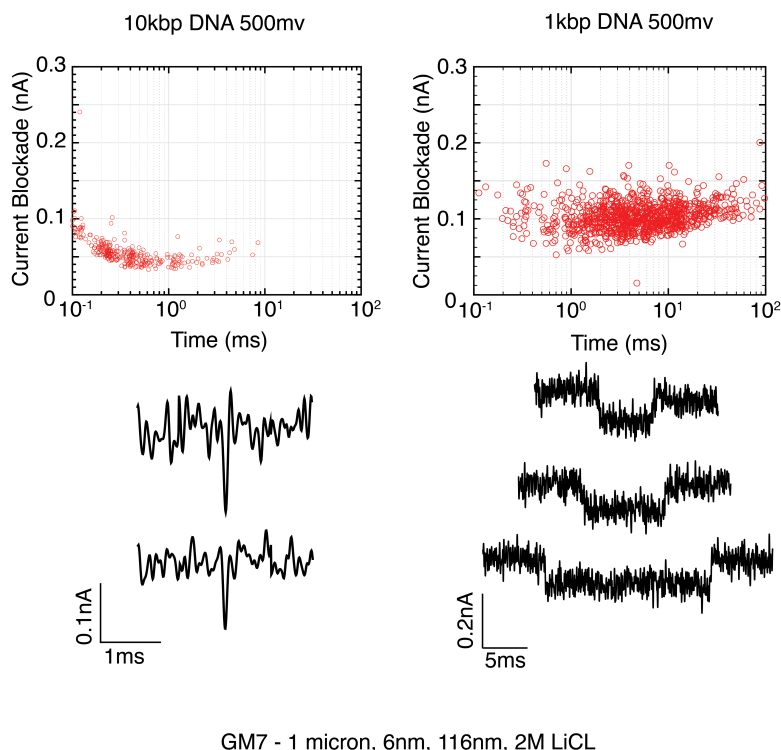
Figure 6.9: **hBN 2D-nanoslit device with DNA translocation events.** We observed exclusively spike events for the 10kbp DNA experiment while the experiment with 1kbp showed primarily DNA translocation event marked by higher current blockade and longer dwell time of the event.

A hBN nanoslit device (1μm x 6nm x 116nm) was fabricated using the procedure outlined in S1 with hBN top and bottom stacks used instead of graphene. Similar to the wetting procedure outline above, the slit was mounted in a PEEK flow cell and buffered with 2M LiCl. An I-V curve was taken to ensure that the device was properly wetted prior to the addition of 10 kbp DNA on the cis side of the flow cell at a bias voltage of 500mV. Similar to the data reported in the main paper, We observe only probing events characterised by short and quick spikes (left column of figure). The device was thoroughly cleaned by rinsing with buffer solution, EtOH and water repeatedly before dismounting. The device was stored in MiliQ water for several days to rinse out any remaining DNA material. The device was then annealed at 250°C in air for 2 hours to ensure complete degradation of DNA and drying of the slit. The device was then remounted and wetted with 2 M LiCl, of which the conductance remained the same as the first experiments with 10kbp DNA. Then 1kbp DNA was introduced from the cis side. This time, clear DNA translocation can be seen showing up as longer blockade in the current trace as well as longer translocation times as seen from the collected scatter plot on the right (right column of figure).

6.5.6. MD SIMULATION SETUP

All simulations of dsDNA translocation through the nanoslit were performed using the Atomic Resolution Brownian Dynamics (ARBD) package [44]. COMSOL software (COMSOL Multiphysics 5.3a) was used to obtain the electrostatic potential that was applied in ARBD. This process is described in detail below.

Continuum modeling The COMSOL software package was used to generate continuum solutions to the electrostatics problem. The computational domain consists of a 160 nm3 initial reservoir, a $400 \times 110 \times 3.5$ nm^3 slit that emerges from the center of the face of the initial reservoir and connects seamlessly to the top face of a 160 nm3 final reservoir. The material properties of the interior of the system were set to those of water, i.e., 100 kg/m^3 density, 0.00089 Pa*s dynamic viscosity, and a relative permittivity of 80. The distribution of the electrostatic potential was obtained using the Electrostatics module. The external potential was introduced into the calculation as Dirichlet boundary conditions on the x-face opposite the slit in the initial reservoir and the z-face opposite the slit in the final reservoir. We used a two-step process to obtain the mesh upon which COMSOL solved the Laplace's equation. First, a free tetrahedral mesh was created using a predefined 'Extremely fine' element size everywhere. We used the resulting mesh to find the initial solution to the electrostatics problem. Next, the solution was refined 5 times using an adaptive mesh procedure with a maximum coarsening factor and element growth rate of 3. The resulting mesh was then saved and used to solve all the electrostatics problems in this work.

MD simulations All simulations were performed using a GPU-accelerated simulation engine ARBD, a 40 fs simulation time step, and a two-bead-per-basepair model of dsDNA that was previously described [33]. The central bead in this model represents the interaction sites within double-stranded segments while the orientation bead represents the local twist of the helix. The bonded interactions in this model are enforced through harmonic potentials, while the non-bonded interactions were chosen to match the experimental measurements of Rau and Parsegian for DNA in a 25 mM MgCl2 electrolyte [46]. A Langevin integration scheme was used to maintain a constant temperature with diffusion constants of 120 and 79 Å/ns for the central and orientation beads, respectively. The CG MD simulation of ssDNA was coupled to the electrostatic potentials extracted from a continuum COMSOL model in the form of an external grid-based potential that applied to the central beads of the DNA. Each central bead was assigned an effective charge of 0.5e, where e is the charge of an electron, to account for electroosmotic forces [9, 47]. Additionally, a repulsive steric potential was applied, in the form of a 3D grid potential, to prevent the DNA from penetrating the solid boundaries of the system. The steric potential was generated using the find_boundaries routine of the image processing Python module, scikit-image [48], to identify a set of boundary layers (in steps matching the 1 nm × 1 nm × 0.5 nm resolution of the grid) from the binary geometry data exported from COMSOL. The values of the steric potential were zero in the reservoirs and slits and increased with each boundary layers as kd^2 where k=100 kcal/mol and d is the distance in nanometers outside the solid boundaries of the system.

Our coarse-grained simulations used point particle beads to represent DNA base pairs. The height that the beads could explore in our simulations was set to 3.5 nm, Figure 6.10. Physically, this corresponded to a slit height of about 6nm when the full di-

ameter of DNA is taken into account, which is about the same height as the slit reported in the experiments. The length and width of the simulated slit was 400 and 110 nm, respectively. Prior to translocation simulations, a 5000-bp DNA strand was equilibrated in a 160 nm3 volume using a multi-resolution simulation protocol. The initial conformation of the molecule was a straight line extending from (0,-55,-80) nm to (0,55,80) nm. The system was equilibrated in five steps of increasing resolution. We started with 108 steps of duration 200 fs/step with a resolution of 100 bp/bead. We then moved on to 10^7 steps at 200 fs/step with 50 bp/bead, 107 steps at 200 fs/step with 25 bp/bead, 107 steps at 100 fs/step with 5 bp/bead, and finally 2×106 steps at 40 fs/step with 1 bp/bead. Eighteen DNA conformations were created in this manner and used to initiate the 18 translocation simulations performed.
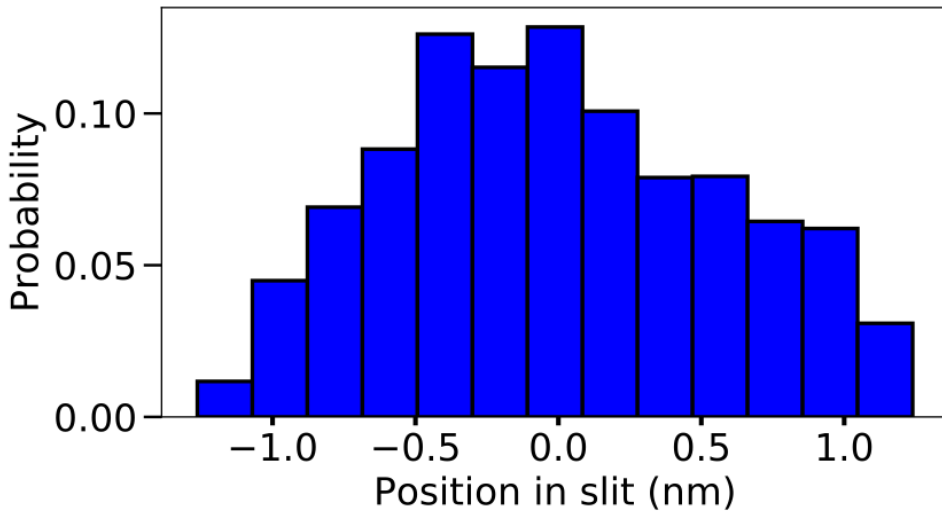
Figure 6.10: **Distribution of the vertical position of simulated DNA molecules** Distribution of the vertical (normal to the slit plane) coordinate of the 2500 (central) beads representing the molecule of DNA. The 3.5 nm height of the slit accessible to the DNA beads corresponds to an experimental slit height of 5.7 nm, taking into account the 2.2 nm diameter of the DNA.

6.5.7. Additional current trace of DNA events obtained from coarsed grained simulations
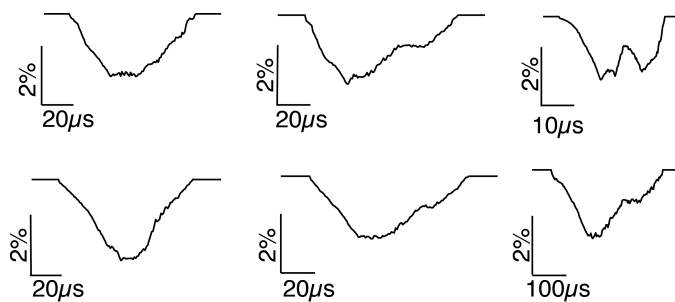
Figure 6.11: **Additional current trace of DNA events obtained from coarsed grained simulations** Simulated current trace of DNA events obtained from coarse-grained Brownian dynamics simulations.

6.5.8. HISTOGRAM OF CURRENT BLOCKADE AND CHARACTERISATION OF EVENT
TYPES
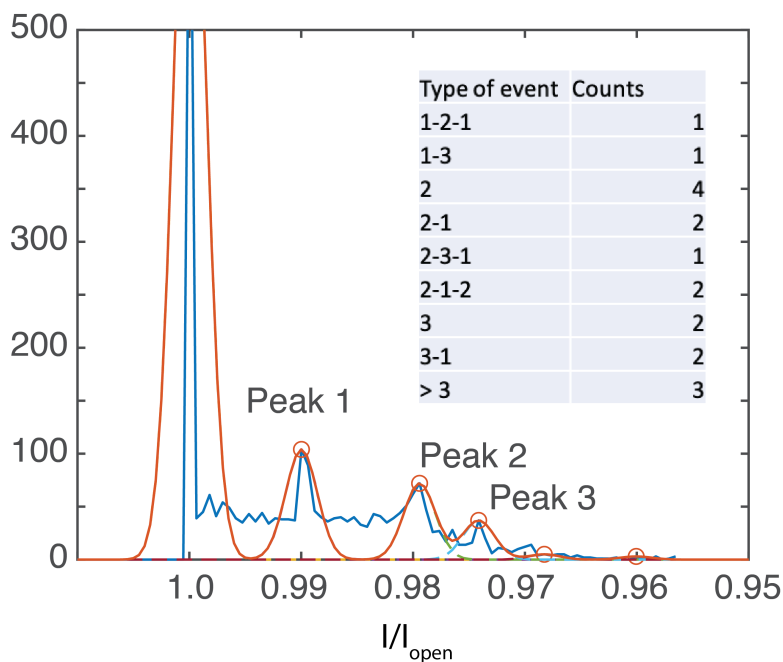
Figure 6.12: **Histogram of current blockade and characterisation of event types** Histogram of the current blockade level achieved for all 16 simulation runs and characterisation of event types. We can identify clear peaks arising from the plateaus from the simulated current trace. We sorted the event type by the plateau levels that they achieved during the translocation process (i.e., peak 1 = type 1). Matching the simulations, we see that the event type corresponds to the number of folds or loops in DNA present in the slit. We did not see a pure type1-only translocation in the simulations which would correspond to a single helix of ds-DNA translocating through the slit. At higher numbers, the accuracy between the number of folds and strands of the DNA diverges because the DNA can adopt different configurations which produces the same number of equivalent DNA strands.

References

[1] S. J. Heerema and C. Dekker, *Graphene nanodevices for DNA sequencing,* Nature Nanotechnology **11**, 127 (2016).

[2] J. J. Kasianowicz and S. M. Bezrukov, *On 'three decades of nanopore sequencing',* Nature Biotechnology **34** (2016).

[3] S. Howorka and Z. Siwy, *Nanopores and Nanochannels: From Gene Sequencing to Genome Mapping,* ACS Nano **10**, 9768 (2016).

[4] F. Persson and J. O. Tegenfeldt, *DNA in nanochannels—directly visualizing genomic information,* Chemical Society Reviews **39**, 985 (2010).

[5] C. Dekker, *Solid-state nanopores,* Nature Nanotechnology **2**, 209 (2007).

[6] E. Samiei, M. Tabrizian, and M. Hoorfar, *A review of digital microfluidics as portable platforms for lab-on a-chip applications,* Lab on a Chip **16**, 2376 (2016).

[7] C. H. Reccius, S. M. Stavis, J. T. Mannion, L. P. Walker, and H. G. Craighead, *Conformation, Length, and Speed Measurements of Electrodynamically Stretched DNA in Nanochannels,* 10.1529/biophysj.107.121020.

[8] B. Lu, F. Albertorio, D. P. Hoogerheide, and J. A. Golovchenko, *Origins and Consequences of Velocity Fluctuations during DNA Passage through a Nanopore,* (2011).

[9] S. van Dorp, U. F. Keyser, N. H. Dekker, C. Dekker, and S. G. Lemay, *Origin of the electrophoretic force on DNA in solid-state nanopores,* Nature Physics **5**, 347 (2009).

[10] C. Plesa, N. van Loo, P. Ketterer, H. Dietz, and C. Dekker, *Velocity of DNA during Translocation through a Solid-State Nanopore,* Nano Letters **15**, 732 (2015).

[11] S. W. P. Turner, M. Cabodi, and H. G. Craighead, *Confinement-Induced Entropic Recoil of Single DNA Molecules in a Nanofluidic Structure,* (2002).

[12] A. Balducci, P. Mao, J. Han, and P. S. Doyle, *Double-stranded dna diffusion in slitlike nanochannels,* Macromolecules **39**, 6273 (2006).

[13] G. B. Salieb-Beugelaar, J. Teapal, J. van Nieuwkasteele, D. Wijnperle, J. O. Tegenfeldt, F. Lisdat, A. van den Berg, and J. C. T. Eijkel, *Field-Dependent DNA Mobility in 20 nm High Nanoslits,* Nano Letters **8**, 1785 (2008).

[14] Y. Zhang and W. Reisner, *Fabrication and characterization of nanopore-interfaced nanochannel devices,* Nanotechnology **26**, 455301 (2015).

[15] D. Xia, J. Yan, and S. Hou, *Fabrication of Nanofluidic Biochips with Nanochannels for Applications in DNA Analysis,* Small **8**, 2787 (2012).

[16] L. D. Menard and J. M. Ramsey, *Fabrication of Sub-5 nm Nanochannels in Insulating Substrates Using Focused Ion Beam Milling,* Nano Letters **11**, 512 (2011).

[17] H. H. Liu, J. He, J. Tang, H. H. Liu, P. Pang, D. Cao, P. Krstic, S. Joseph, S. Lindsay, and C. Nuckolls, *Translocation of single-stranded DNA through single-walled carbon nanotubes.* Science (New York, N.Y.) **327**, 64 (2010).

[18] J. K. Holt, H. G. Park, Y. Wang, M. Stadermann, A. B. Artyukhin, C. P. Grigoropoulos, A. Noy, and O. Bakajin, *Fast mass transport through sub-2-nanometer carbon nanotubes.* Science (New York, N.Y.) **312**, 1034 (2006).

[19] J. Geng, K. Kim, J. Zhang, A. Escalada, R. Tunuguntla, L. R. Comolli, F. I. Allen, A. V. Shnyrova, K. R. Cho, D. Munoz, Y. M. Wang, C. P. Grigoropoulos, C. M. Ajo-Franklin, V. A. Frolov, and A. Noy, *Stochastic transport through carbon nanotubes in lipid bilayers and live cell membranes,* Nature **514**, 612 (2014).

[20] L. Bocquet, *Nanofluidics coming of age,* Nature Materials **19**, 254 (2020).

[21] B. Radha, A. Esfandiar, F. C. Wang, A. P. Rooney, K. Gopinadhan, A. Keerthi, A. Mishchenko, A. Janardanan, P. Blake, L. Fumagalli, M. Lozada-Hidalgo, S. Garaj, S. J. Haigh, I. V. Grigorieva, H. A. Wu, and A. K. Geim, *Molecular transport through capillaries made with atomic-scale precision,* Nature **538**, 222 (2016).

[22] A. Keerthi, A. K. Geim, A. Janardanan, A. P. Rooney, A. Esfandiar, S. Hu, S. A. Dar, I. V. Grigorieva, S. J. Haigh, F. C. Wang, and B. Radha, *Ballistic molecular transport through two-dimensional channels,* Nature **558**, 420 (2018).

[23] T. Mouterde, A. Keerthi, A. R. Poggioli, S. A. Dar, A. Siria, A. K. Geim, L. Bocquet, and B. Radha, *Molecular streaming and its voltage control in ångström-scale channels,* Nature **567**, 87 (2019).

[24] M. Shankla and A. Aksimentiev, *Step-defect guided delivery of DNA to a graphene nanopore,* Nature Nanotechnology **14**, 858 (2019).

[25] M. Shankla and A. Aksimentiev, *Conformational transitions and stop-and-go nanopore transport of single-stranded DNA on charged graphene,* Nature Communications **5**, 5171 (2014).

[26] M. Liu, H. Zhao, S. Chen, H. Yu, and X. Quan, *Capture of double-stranded DNA in stacked-graphene: giving new insight into the graphene/DNA interaction,* Chem. Commun. **48**, 564 (2012).

[27] S. W. Kowalczyk, D. B. Wells, A. Aksimentiev, and C. Dekker, *Slowing down DNA Translocation through a Nanopore in Lithium Chloride,* Nano Letters **12**, 1038 (2012).

[28] J. Li, D. Stein, C. McMullan, D. Branton, M. J. Aziz, and J. A. Golovchenko, *Ion-beam sculpting at nanometre length scales,* Nature **412**, 166 (2001).

[29] A. J. Storm, J. H. Chen, H. W. Zandbergen, and C. Dekker, *Translocation of double-strand DNA through a silicon oxide nanopore,* Physical Review E - Statistical, Nonlinear, and Soft Matter Physics **71**, 051903 (2005).

6

[30] M. Cabodi, S. W. Turner, and H. G. Craighead, *Entropic recoil separation of long dna molecules,* Analytical chemistry **74**, 5169 (2002).

[31] N. A. Bell, M. Muthukumar, and U. F. Keyser, *Translocation frequency of double-stranded DNA through a solid-state nanopore,* Physical Review E **93**, 022401 (2016), arXiv:1508.04396 .

[32] D. J. Bonthuis, C. Meyer, D. Stein, and C. Dekker, *Conformation and dynamics of DNA confined in slitlike nanofluidic channels.* Physical review letters **101**, 108303 (2008).

[33] C. Maffeo and A. Aksimentiev, *MrDNA: a multi-resolution model for predicting the structure and dynamics of DNA systems,* Nucleic Acids Research **48**, 5135 (2020).

[34] J. Wilson, K. Sarthak, W. Si, L. Gao, and A. Aksimentiev, *Rapid and Accurate Determination of Nanopore Ionic Current Using a Steric Exclusion Model,* ACS Sensors **4**, 634 (2019).

[35] R. Zwanzig, *Diffusion in a rough potential.* Proceedings of the National Academy of Sciences of the United States of America **85**, 2029 (1988).

[36] C. Plesa, D. Verschueren, S. Pud, J. van der Torre, J. W. Ruitenberg, M. J. Witteveen, M. P. Jonsson, A. Y. Grosberg, Y. Rabin, and C. Dekker, *Direct observation of DNA knots using a solid-state nanopore,* Nature Nanotechnology **11**, 1093 (2016).

[37] R. Kumar Sharma, I. Agrawal, L. Dai, P. S. Doyle, and S. Garaj, *Complex DNA knots detected with a nanopore sensor,* Nature Communications **10**, 4473 (2019).

[38] A. Esfandiar, B. Radha, F. Wang, Q. Yang, S. Hu, S. Garaj, R. Nair, A. Geim, and K. Gopinadhan, *Size effect in ion transport through angstrom-scale slits,* Science **358**, 511 (2017).

[39] D. W. Boukhvalov and M. I. Katsnelson, *Chemical Functionalization of Graphene with Defects,* Nano Letters **8**, 4373 (2008).

[40] S. Garaj, W. Hubbard, A. Reina, J. Kong, D. Branton, and J. A. Golovchenko, *Graphene as a subnanometre trans-electrode membrane,* Nature **467**, 190 (2010).

[41] F. Banhart, J. Kotakoski, and A. V. Krasheninnikov, *Structural Defects in Graphene,* ACS Nano **5**, 26 (2011).

[42] G. F. Schneider, Q. Xu, S. Hage, S. Luik, J. N. H. Spoor, S. Malladi, H. Zandbergen, and C. Dekker, *Tailoring the hydrophobicity of graphene for its use as nanopores for DNA translocation,* Nature Communications **4**, 2619 (2013).

[43] C. Plesa and C. Dekker, *Data analysis methods for solid-state nanopores,* Nanotechnnology **26**, 084003 (2015).

[44] J. Comer and A. Aksimentiev, *Predicting the DNA Sequence Dependence of Nanopore Ion Current Using Atomic-Resolution Brownian Dynamics,* The Journal of Physical Chemistry C **116**, 3376 (2012).

[45] S. J. Haigh, A. Gholinia, R. Jalil, S. Romani, L. Britnell, D. C. Elias, K. S. Novoselov, L. A. Ponomarenko, A. K. Geim, and R. Gorbachev, *Cross-sectional imaging of individual layers and buried interfaces of graphene-based heterostructures and superlattices,* Nature Materials **11**, 764 (2012).

[46] D. Rau, B. Lee, and V. Parsegian, *Measurement of the repulsive force between polyelectrolyte molecules in ionic solution: hydration forces between parallel dna double helices,* Proceedings of the National Academy of Sciences **81**, 2621 (1984).

[47] B. Luan and A. Aksimentiev, *Electro-osmotic screening of the DNA charge in a nanopore,* Physical Review E - Statistical, Nonlinear, and Soft Matter Physics **78**, 021912 (2008).

[48] S. van der Walt, J. L. Schönberger, J. Nunez-Iglesias, F. Boulogne, J. D. Warner, N. Yager, E. Gouillart, and T. Yu, *scikit-image: image processing in Python,* PeerJ **2**, e453 (2014).

6

7

TWEEZING OF INDIVIDUAL PROTEINS IN PLASMONIC NANOPORES

We show label-free optical trapping of individual 20 nm polystyrene beads as well as of individual proteins in inverted-bowtie-shaped plasmonic gold nanopores. Our system employs an optical readout method where the presence of the protein entering the trap is marked by an increase in the transmission of light through the nanoaperture due to the shifting of the plasmonic resonance. We show that arrays of these nanoapertures can be reliably and consistently produced using Focused Ion Milling with gap sizes of around 10-20 nm and single-nm variation, and a remarkable stability that allows for repeated use. The optical trapping force of the plasmonic nanopores allows individual 20 nm polystyrene beads and proteins such as Beta-amylase and Heat Shock Protein 90 (HSP90) to be trapped for very long times of multiple minutes. On demand, we can release the trapped molecule by turning off the laser, allowing the molecule to diffuse through the device and for another protein to be interrogated. The throughhole nanoapertures allow to drive out the analytes by translocation instead of relying only on diffusive processes. The protein-trapping approach opens up new routes to acquire information on protein shape, conformation, and dynamics. Given the preliminary success of the protein trapping with these nanoapertures, we propose future experiments on the conformational dynamics of HSP90 proteins modulated by nucleotide binding.

7.1. INTRODUCTION

Proteins are responsible for virtually all cellular functions [1, 2]. Just to name some examples which we will explore in this work, Beta-amylase is a catalytic enzyme that allows cells to breakdown and digest glucose [3, 4]. Other proteins such as the Heat Shock Protein are chaperone proteins that assist to other proteins in the cell with protein folding and allow them to adopt their proper functional shape [5]. In order to accomplish their function, many proteins are molecular machines that can exhibit several physical shapes that they transit between while performing their function. To understand the underlying mechanism of such conformational changes, it is necessary to resolve the internal dynamics of single proteins. Traditional techniques such as X-ray diffraction and cryo-EM resolve protein structure at near atomic level resolution but yield only static images, where dynamics has to be reconstructed a posteriori [6–10]. Other techniques such as FRET require site-specific labelling of the protein which may interfere with its function [11, 12]. Indeed there has been a strong drive in biophysics to search for new single molecule tools capable of sensing of protein dynamics in an in vitro environment [13].

An appealing idea from the field is to trap a single protein, tether-free in an aqueous buffer for an extended period of time for observation on its dynamics [14–17]. One approach has been to use solid-state nanopores where a nanoaperture is etched through a SiN membrane [18–20]. By monitoring the ionic current through this nanoscale opening, one may attempt to obtain some information on the protein shape and conformation as the protein translocates through the nanopore [21]. However, there are fundamental limitations in the sensing time as characteristically, the translocation time of the analyte is very fast (in the range of microseconds to milliseconds) [22]. Such approaches are limited to capturing only snapshots of the protein's shape. Various groups have proposed different techniques including microfluidic devices, most notably, the Anti-Brownian Electrokinetic Traps (ABEL) that tracks the molecule of interest and applies a real time electrokinetic feedback to compensate and negate the drift from Brownian motion [23–25]. The analyte can be kept in the field of view and monitored for seconds. However, this technique still requires the molecule to be labelled with a fluorescent tag in order to be accurately tracked and lacks the resolution to resolve the shape of the protein.

Plasmonic nanostructures have recently gained interest for biosensing [26]. These are nanostructures that are typically milled into a material (such as gold or silver) that support plasmons, coherent electron oscillations that are driven by an incident light [27]. These structures have the ability to focus electromagnetic fields into nanoscale volumes below the diffraction limit. The optical resonance of these structures is extremely sensitive to the geometry of the structures and local dielectric environment at subdiffraction volumes ($<nm^3$). One class of these structures are plasmonic nanopores, nanoapertures which are holes milled through the freestanding metal layer which can support plasmon excitations [28–30]. These structures can exhibit an enhanced optical transmission (extraordinary transmission), which can be magnitudes higher than classically predicted. An analyte entering this volume will cause a shift in the optical resonance that can be probed with a high-speed photodetector (typically an avalanche photodiode – APD). By monitoring the transmitted light at a single frequency, an induced shift in the optical resonance of the nanoaperture will lead to a measurable change in the transmission level recorded on the detector.

Additionally, the tight concentration of the incident laser light by the nanoaperture, in particular across a gap within the nanoaperture, can produce strong optical gradient forces that can give rise to a tweezing force [17, 31, 32]. These has been demonstrated for a variety of nanoapertures that were shown to tweeze small dielectric nanoparticles, i.e. beads and even single proteins. For example, Gordon et al used nanoapertures that are supported on a glass substrate to detect and tweeze polystyrene (PS) beads and proteins [33, 34]. The majority of trapping times of these structures have so far been limited to a few seconds, before the proteins would spontaneously escape due to Brownian motion. If further developed, this technique may potentially be used to detect changes in the shape of the proteins, as different conformations within the nanoaperture may show up as different levels in the optical transmission [33, 35]. Most development has focused on these well-shaped traps with one opening closed off by the substrate. However, the development of a throughhole nanoaperture will allow for features such as electrophoretically defined directionality and ionic sensing to be integrated, allowing for full control over the analyte's motion instead of relying on diffusive processes to drive the molecule into the sensing region as well as having the benefit of two complementary sensing techniques, viz., optical and electrical [36–38]. However, general progress on this tweezing and sensing technique has been hindered by challenges in the fabrication of plasmonics nanoapertures, as minute variations in the geometry of the fabricated structures give rise to large differences in the optical and nanotweezing properties.

Here, we demonstrate a focused-ion-beam (FIB) method to fabricate an array of bowties on a single membrane with outstanding properties for single-molecule trapping. The nanoapertures were defined as an inverted bowtie shape and milled into a layer of Au. We characterised the geometry by the gap size and the length of the bowtie. The variation in the two critical dimensions of the produced geometries within a produced array were found be very small, i.e., less than 2 nm. Consistent with that homogeneity of the plasmonic structures, all nanoapertures in the array displayed a similar optical response in terms of their optical transmission. The traps were used to tweeze and probe two types of proteins (Beta-amylase, HSP90) which were stably trapped for long times (> 180seconds). From the trapping signals, we find evidence for significant low frequency motion that may be associated with the internal protein dynamics. Proteins could be released on-demand and the structures were robust enough to be used across multiple experimental runs. The development of a throughhole nanoaperture allows for the direction of the analyte translocation to be controlled instead of relying only on diffusive processes. We conclude by proposing future experiments to study the dynamics of HSP90 by modulating it with nucleotides.

7.2. RESULTS

7.2.1. FABRICATION AND TEM CHARACTERIZATION OF INVERTED BOWTIE STRUCTURES

We fabricated our plasmonic structures using direct Focused Ion Beam (FIB) milling of gold. Most fabrication methods for the production of nanoapertures are based on e-beam lithography and etching. By contrast, FIB milling uses a highly energetic beam of ions (typically Ne or Ga) to knock out atoms directly from the substrate [39]. The
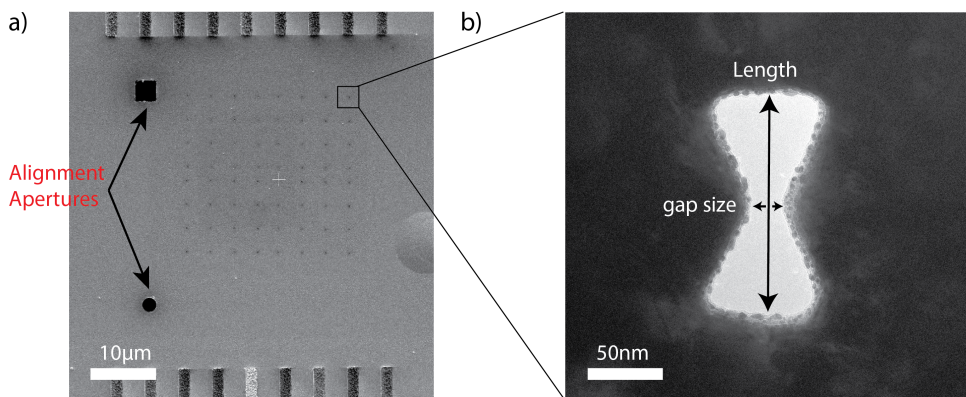
Figure 7.1: **Figure 1: Array of inverted bowtie nanoantennas.** a) SEM image of an array of inverted bowtie antennas. The apertures were drilled into a 100nm thick gold film on a freestanding SiN membrane by local milling with a FIB. Two alignment apertures were milled next to the array. b) TEM image of FIB-milled nanoaperture. The length and gap size are indicated. The fabricated structures were very consistent across the array with an average length and gap size of 160 ± 2 nm and 23 ± 2 nm, respectively.

lack of a masking step that is required in standard e-beam lithography techniques eliminates variables such as the resolution of the resist mask, development times, and etching times, which can drastically vary and thus influence the final shape of the produced structures [40]. FIB milling simplifies the process and reduced the parameters to two variables, the spot size and dwell time of the ion beam used.

Plasmonic structures were fabricated in a gold layer on a freestanding SiN membrane. A thin adhesion layer of 2-3 nm of Ti was deposited onto the SiN, before 100nm of Au was deposited, which provided the starting material for the plasmonics aperture to be milled in. We chose to fabricate inverted bowtie shape structures where the electromagnetic field will be concentrated at the edges near the center point of the bowtie. Such an inverted bowtie shape also allows for good thermal properties as heat from the incident laser is drained to the surrounding gold which acts as a heat sink. The structures were drilled with a Ga ion beam by intersecting two overlapping inverted triangles [41]. The dose and amount of overlap was optimized to produce the desired result in the gap size. The structure geometry and final gap size strongly depended on the size of the ion beam aperture used. Figure 7.1 shows an example of a SEM image of an array and a TEM image of a fabricated bowtie. Here, we fabricated 8x8 inverted bowties with the same parameters. The bowties were mutually spaced 2.5 μm apart in order to ensure that only one bowtie was illuminated within the laser spot (~1 μm) during the optical measurements. Additionally, we milled 2 larger apertures for the alignment and calibration of the laser.

The dimensions of the fabricated structures were characterized under TEM. For this particular array, the size of the gap was found to be 23 ± 2 nm (mean ± SD) while the length of the inverted structure was 160 ± 2 nm (mean ± SD). At the edges of the structures, we observed some grains from the deposited gold after milling, that appeared as jagged edges.
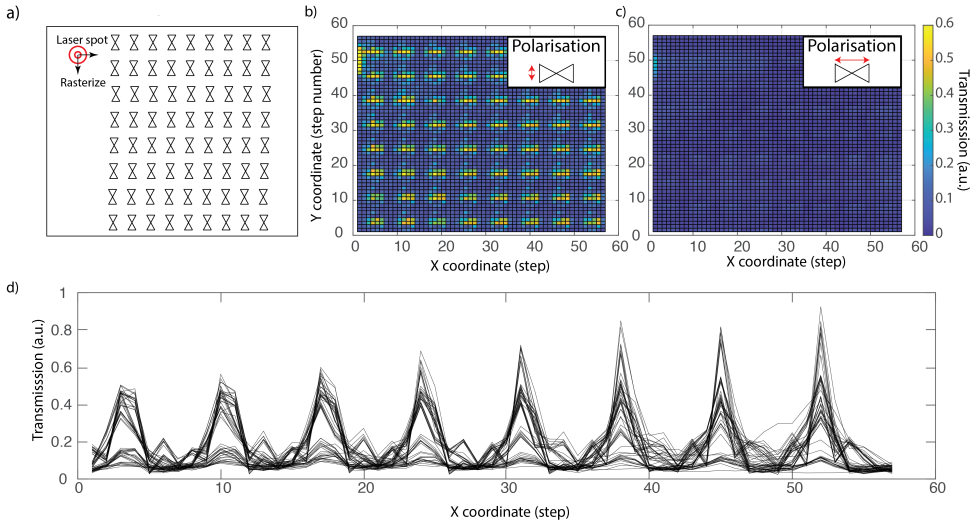
Figure 7.2: **Characterization of optical transmission of inverted bowtie nanoantennas.** a) Schematic of an array of inverted bowties. A laser can be rastered across the array in steps of 500 nm with 5 steps being the mutual distance between bowties (2.5 micron), and the transmission of each bowtie antenna can be measured. Two orthogonal polarizations are used. b) Heat map of the optical transmission when the laser polarization was in the longitudinal polarisation (across the gap). The measured transmission increased greatly when the laser was located at an aperture. c) Similar heat map of the optical transmission when the polarization was orthogonal (across the length of the bowtie). The optical transmission remained low. The sample was divided into a grid with each row consisting of an area of 500nm by 30 μm. d) Line profile of the measured optical transmission across the sample. Each row of the measured optical transmission in b) was converted into a line profile and plotted in pane d. We see that the line profile increased to a maximum value of 0.5-0.8 each time that the laser was positioned on top of a bowtie. In the areas in between the bowties and in the rows where the laser did not cross a bowtie, the optical transmission remained low (<0.1). For the row of bowties on the right side of the membrane, there was a small increase in the measured transmission because the large free-standing SiN membrane was not flat leading to slightly different alignments.

7.2.2. OPTICAL CHARACTERIZATION SHOWS THAT THE PLASMONIC NANOAPERTURES ARE HIGHLY UNIFORM

We characterized the optical transmission of the bowtie apertures in the arrays. FDTD simulations showed that the structures are expected to have a maximum transmission peak in the near infra-red region, just below the wavelength of the laser (~1064nm) (see SI7.7) [42]. The sample was mounted in the laser setup (1064nm, 20mW) and an avalanche photodiode (APD) collected the transmitted light. The laser was raster scanned across the array and the transmitted light was recorded for each bowtie by the APD and plotted in a 2D heat map (Fig. 7.2a). We acquired such a 2D map in two different polarization (transverse – along the length of the bowtie; and longitudinal – across the gap of the bowtie). Figure 7.2b-c shows the 2D maps in the two different polarizations. For the longitudinal polarization, the transmission value increased drastically when the laser scanned across the nanoapertures. In the areas between bowties, a negligible amount of light was collected demonstrating that the thickness of the gold (100nm) act as a sufficient stop to the incident light. When the polarization was rotated by 90 degrees, how-
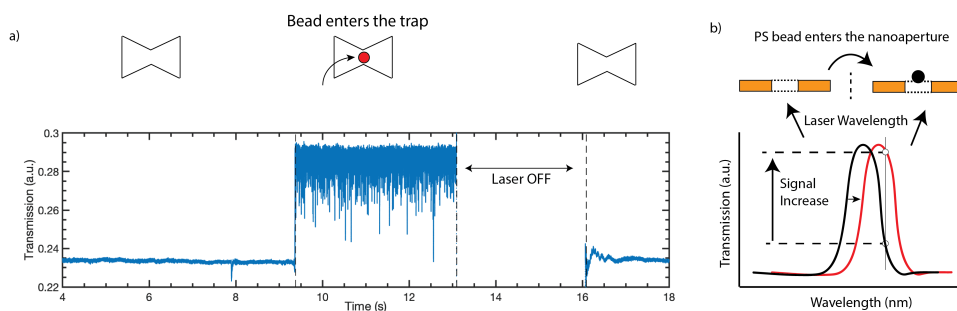
Figure 7.3: **Optical Trapping of 20 nm Polystyrene beads.** a) Transmission level signal versus time. The signal abruptly increases indicating that a single PS has entered the trap. When the laser is temporary shut off and switched back on, the transmission level returns to the previous baseline indicating that the object has been released. b) Schematic representation of the red shifting of the nanoaperture in the presence of a bead. The peak of the resonance redshifts towards the wavelength of the laser which leads to an increased in transmission of the nanoaperture.

ever, the transmission value dropped to the baseline, i.e., no extraordinary transmission of light occurred, as expected. Figure 7.2d shows a line plot of the measured transmission for each row of the 2D map. The bowties yielded very similar optical intensities with the intensities rising to roughly the same value for bowties in the same row. Furthermore, to show that the transmission of the inverted bowtie apertures was sensitive to the fabrication geometry, we also milled samples with a larger gap size of the bowties in the last 2 columns and, as expected, this yielded a larger transmission (See SI-2).

To demonstrate the optical-trapping abilities of these plasmonic structures, we first performed control experiments with 20nm PS beads. We added PS beads (0.05% w/v) to the gold side of the sample. The laser was kept on a single inverted bowtie and the transmission level was recorded. After waiting for some time, a sudden increase of the optical transmission was recorded for the bowtie (N=46). Figure 7.3a shows an example. The transmission level was initially stable at an intensity of about 0.23 (a.u.). At some point, the transmission level suddenly increased to a value of 0.29. This increased transmission was recorded for a few seconds, after which the laser was shut off. When the bowtie was probed again with the laser 3 seconds later, the transmission level had returned to the original level of 0.23. We interpret the increase in the signal as the optical trapping of a PS bead into the bowtie, which subsequently escaped the trap by diffusion when the laser was shut off. Upon entry of the PS bead into the trap, the optical resonance of the nanoaperture red-shifted towards the 1024 nm wavelength of the laser, leading to the increase in the transmission level of the nanoaperture, as illustrated in Figure 7.3 b. No such traces were seen when no PS bead was suspended in the buffer.

7.2.3. TRAPPING OF SINGLE PROTEINS

We explored the application of our nano-tweezers for trapping and studying individual proteins of two types, Beta-amylase, and HSP90. We started with Beta-amylase, a globular tetrameric protein consisting of 4 monomer subunits with a combined molecular weight of 200 kDa that is commonly used as a molecular standard. At pH 6-8, it is sta-
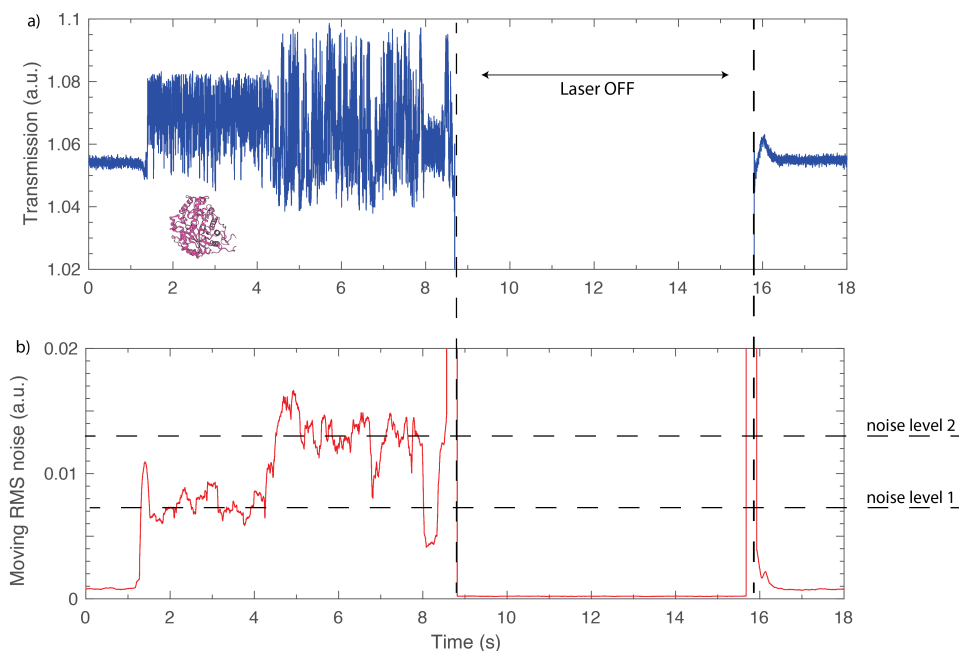
Figure 7.4: **Optical trapping of Beta-amylase protein** a) Transmission signal over time of a trapped Beta-amylase protein. Similar to the PS bead In Fig.3, an increase in transmission is observed when the protein enters the trap. The transmission level returned to the baseline when the laser was turned back on after ~5 seconds. Inset shows the Beta-amylase protein. b) RMS noise of the trapping signal over time. We observe 3 levels of fluctuations: (i) low fluctuations for the empty trap, (ii) an increased level of fluctuations upon trapping (noise level 1), and (iii) an even higher level of fluctuations appearing at t = 4 s (noise level 2). The level decreases back to level ii at t = 8 s. There is a short increase back to noise level 2, just before the laser was turned off.

ble up to 60 degrees which furthermore makes it an excellent protein to characterize our traps. We introduced Beta-amylase in our traps (0.1% w/v) and recorded trapping events (N=112). A -250mV bias voltage was applied in order to drive the protein into the trap. Figure7.4a shows an example of a trapping event. Similar to the experiment for the PS bead, the transmission through the nanoaperture initially remained at the value as the measured baseline. After a few seconds, the transmission through the aperture suddenly increased from an average value of 1.055 to 1.07 (a.u.). We interpret this signal as an indication of a single protein getting trapped into a nanoaperture. Control experiments in nanoapertures that had gap sizes too small to fit the protein did not yield stable trapping signals.

During the trapping, the signal of Beta-amylase showed distinct stages in its fluctuation amplitude, which we characterised by the RMS noise 7.4b. A moving standard deviation was calculated and plotted in Figure 7.4b. The empty trap showed low fluctuations (RMS 0.001 a.u.). Upon trapping, the level of fluctuations increased drastically to an RMS of 0.007 a.u.. An even higher level of fluctuations appeared at t = 4 s where the RMS increased to a value of 0.013 a.u. At t = 8 s, the level decreases back to the first level,
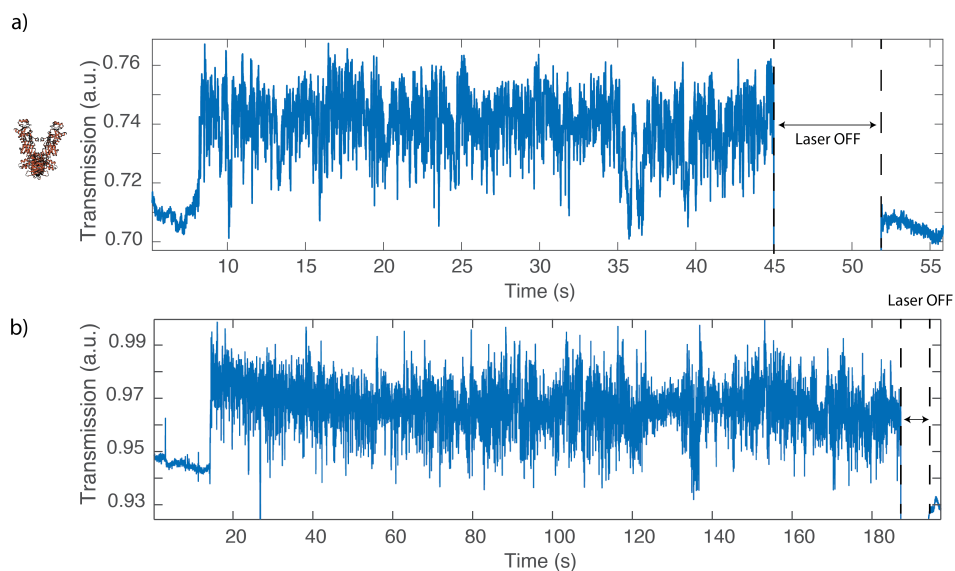
Figure 7.5: **Optical trapping of HSP90 protein** a) Transmission level versus time for HSP90. The transmission level increased when HSP90 was optically trapped in the bowtie structure.When the laser was switched off for ~7 seconds, the protein had been released. Left inset shows the HSP90 protein. b) Long trapping trace of HSP90. We successfully tweezed the protein for 3 minutes. After that, the laser was switched for 10 seconds and turned back on. The baseline then had returned to the initial transmission level, indicating that the protein had been released.

7

just before the laser was turned off, possibly indicating that two states that are reversible, and less well compatible with protein denaturation in the trap. To ensure that these observations and the trapping signal was not simply unspecific sticking of the proteins to our traps, we shut off the laser to show that we can release the trapped molecule and return the trap to its initial empty state. Out of 112 dataset, only 1 such event did not respond in this way to the interruption of the laser.

Next, we studied HSP90 proteins (N=12). HSP90 is a dimeric protein complex (total mass 180 kDa) that belongs the family of chaperone proteins that are important for proper folding and maintenance of other proteins within the cell [43]. They have been reported to undergo conformational changes between an open and a closed state that involve 5-8 nm change. FRET studies, which requires site-specific labelling of the protein, indicate that these transitions occur on the 0.1-0.5 Hz scales [44–46]. Upon addition of 50 nM of HSP90 proteins to the system, we observed the same type of trapping events, with a sudden increase in the transmission signal, indicating that a protein was being tweezed, see Figure7.5a for an example. The transmission of the bowtie increased and fluctuated between an intensity level of 0.72-0.76 with some sharp downward spikes. Very long trapping times could be realized, i.e., many minutes, as can be seen in the examples of Fig.7.5b where the event lasted for almost 3 minutes. In practice, the trapping events were terminated by shutting down the laser to ensure that the proteins were not simply sticking to the trap after about a minute.

The trapped proteins showed pronounced low-frequency fluctuations. To show this, we applied a low pass filter of 10Hz to the traces and build up a histogram of the measured transmitted signal, see Figure7.6. In the case of the PS beads, most of the fluctuations were filtered out, indicating that the major fluctuations had higher characteristic frequencies. For the protein traces, however, low-frequency fluctuations prevailed in the signals. At this stage, it is unclear what causes these fluctuations. Slow conformational changes are an attractive option, but further research is needed to unambiguously ascertain this.

Interestingly, we found that the devices were very robust in these protein trapping experiments. We tried their reuse in multiple experiments. Between each experimental run, the sample was rinsed in H20 and ethanol, followed by an oxygen plasma to remove contamination. Structures were imaged under a TEM (See SI-3) before and after a series of 3 experiments on the same bowtie. Aside from a slight increase of about 1nm in the gap size, there was no observable change to the nanoaperture such as protein residues. In general, the same antenna could be used multiple times for hours.

7.3. CONCLUSION AND SUGGESTIONS FOR FOLLOW UP EXPERIMENTS

In conclusion, we have demonstrated a direct milling FIB method to fabricate nanoapertures for optical sensing and tweezing. We explored the application of our nano-tweezers for use in the study of protein dynamics. This label-free technique allows for the interrogation of a variety of proteins. We were able to tweeze and trap proteins for extended periods of time (minutes) paving the way to study slow conformational changes in protein. The proteins showed distinct low-frequency fluctuations in their transmission level, possibly associated with protein conformational changes. Our nanotweezers with a throughhole allow for future integration with electrical readout methods or for the analyte to be driven electrophoretically in a user-defined direction instead of relying on pure diffusion.

In future work, we plan experiments focused on resolving the dynamics of HSP90, which undergoes conformational changes in a chemo-mechanical ATP-hydrolysis cycle [47, 48]. For example, the transition from the open to the closed state has been shown to be slowed down in the presence of Adenylyl-imidodiphosphate (AMP-PNP). By introducing this into the buffer, we may be able to probe if the observed fluctuations in the signal are indeed linked to the protein conformational shape or derive from other sources. Monitoring such kinetics of single proteins may open up new exciting avenues in the study of protein dynamics which can be probed by varying the ATP concentration or mutations.
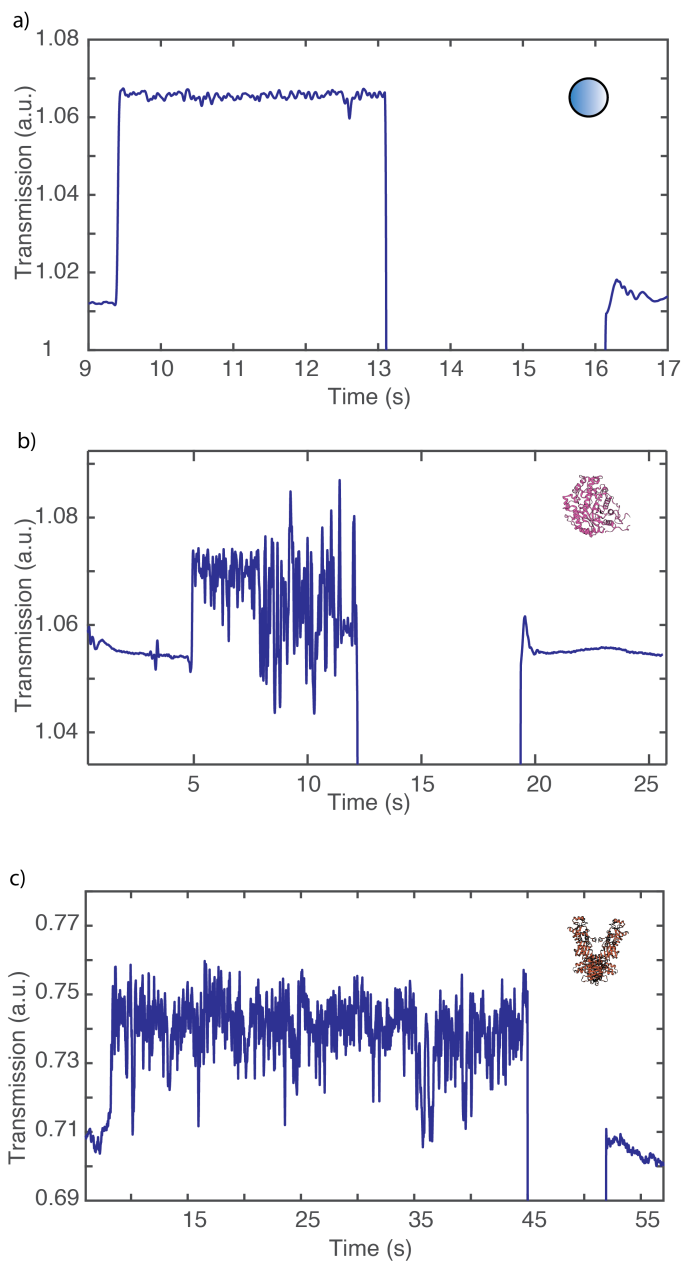
Figure 7.6: **Effect of low-pass filtering on data traces** a) 10Hz low-pass-filtered traces for PS bead. Fluctuations in the transmitted signal for the PS bead reduced to a single homogenous level when the signal was low-pass filtered. b) 10Hz low-pass-filtered traces for Beta Amylase. c) 10Hz low-pass-filtered traces for HSP90. The low frequency modulations are still present in the trapping signal for the protein traces unlike the PS bead trace, indicating significant low-frequency fluctuations.

7.4. Methods

7.4.1. Fabrication of nanoapertures
The nanoapertures were fabricated on 20nm free-standing SiN membrane that were fabricated according to the protocol listed by Janssen et al. 1-3 nm Ti was sputtered on the substrate as an adhesion layer, after which 100nm of Au was deposited using an electron-beam evaporator (Temescal). The nanoapertures were then milled with a Ga beam in a FEI Helios G4 CX (30KeV, 2pA beam).

7.4.2. Experimental setup
The sample was first rinsed in ethanol and H2O and cleaned in an O2 plasma at 50W for 1 minute. The sample is mounted in a custom-made PEEK flowcell that allows for the laser to optically excite the nanoapertures and for the transmission light to be collected. The flow cell was either filled with H2O or 1x phosphate buffered saline (PBS). There was no noticeable change in the optical transmission of the nanoapertures between the two different buffers as they have very similar refractive indexes. A 1064nm laser was focused onto the nanoapertures (M9-A64-0200 laser diode, Thorlabs) with a 60x objective. The laser light was collected using a 10x 0.3NA objective (Nikon) and projected onto an Avalanche Photo Diode (APD410C/M Thorlabs). A 2D map was taken by rasterizing across the array of nanoapertures using a piezoelectric stage (MadCity Labs Inc). The transmission was acquired at a sampling rate of 200 kHz and low-pass filtered down to the indicated values during the analysis.

7.4.3. Analytes
We studied the following analytes for the experiments: 20nm polystyrene beads (Thermo-Fisher)- 0.05% w/v; Beta-amylase (Sigma) -0.05% w/v; Heat Shock Protein 90(HSP90) (Obtained from the Hugel Lab)- 50nMol. All analytes were diluted in 1X PBS that was additionally buffered with 5nM of MgCL in the case of the HSP90.

7.4.4. Analysis of events
Event detection and analysis was performed using Tranzalyser, a custom-made MATLAB-based software package [49]. All traces shown in the plot were low-pass filtered at 10 kHz unless indicated otherwise.

7.5. SUPPORTING INFORMATION
7.5.1. FDTD SIMULATED TRANSMISSION
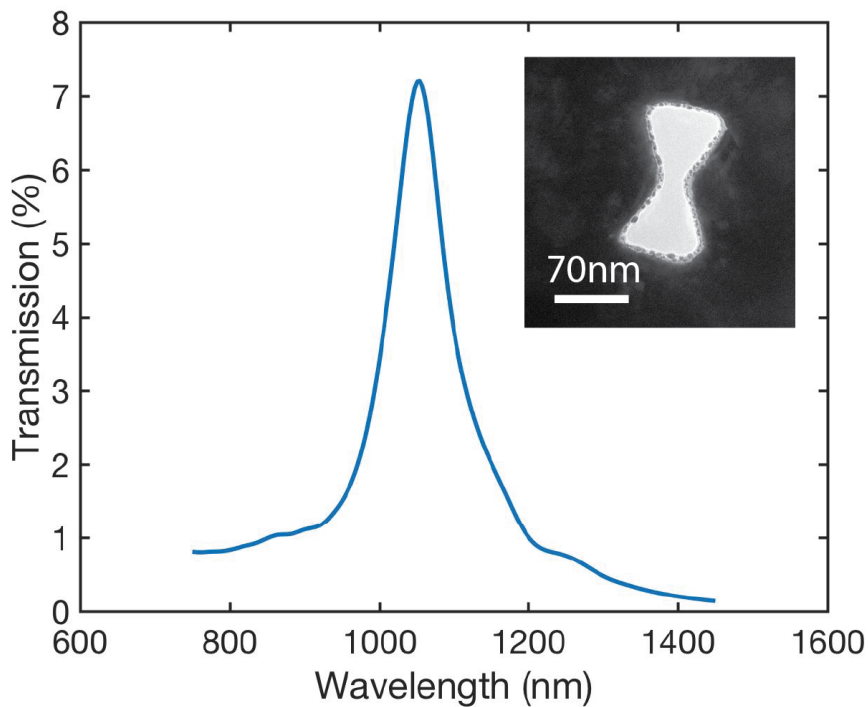
Figure 7.7: **FDTD Simulated transmission vs. wavelength of inverted bowtie structure.** The insert shows the TEM image used to build the model in FDTD by defining the black areas of the TEM as 100nm of Au and defining the white areas as water.

7.5.2. 2D HEAT MAP OF OPTICAL TRANSMISSION OF BOWTIE ARRAY IN 2 OR-THOGONAL POLARISATION
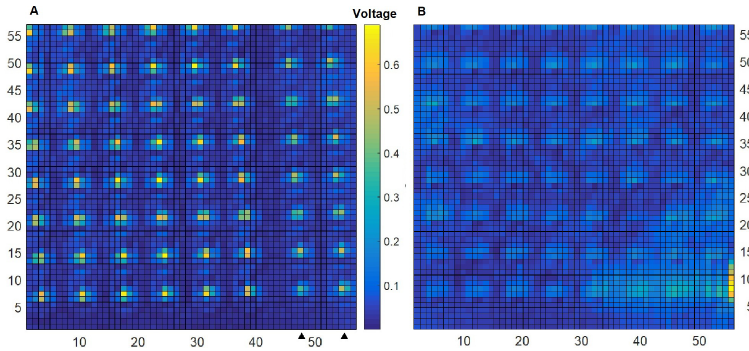
Figure 7.8: **2D heat map of optical transmission of bowtie array in 2 orthogonal polarizations.** The optical transmission of the array rose to the same optical transmission value except for the last 2 columns that were slightly dimmer. Notably the bowties in the last 2 columns were milled to have smaller gap sizes (2nm smaller).

7.5.3. TEM IMAGE OF BOWTIE STRUCTURES BEFORE AND AFTER LIQUID EXPERIMENTS.
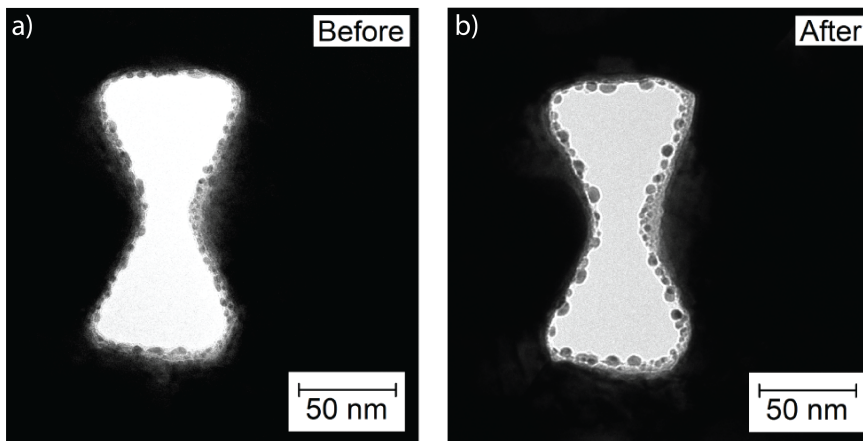
Figure 7.9: **TEM image of bowtie structures before and after liquid experiments.** a) TEM image of the bowtie after FIB milling b) TEM image of the same bowtie after 3 rounds of liquid experiments with 2 plasma-cleaning steps in between these. We see that the structure remains intact except for a slight erosion of the gold edges allowing the same structures to be reused for several rounds of experiments.

REFERENCES

[1] T. Ha, *Single-molecule methods leap ahead,* Nature Methods **11**, 1015 (2014).

[2] W. E. Moerner, *New directions in single-molecule imaging and analysis,* (2007).

[3] F. Kaplan, D. Y. Sung, and C. L. Guy, *Roles of beta-amylase and starch breakdown during temperatures stress,* Physiologia Plantarum **126**, 120 (2006).

[4] R. H. Hopkins, B. Jelinek, and L. E. Harrison, *The action of beta-amylase on potato amylose.* The Biochemical journal **43**, 32 (1948).

[5] D. Whitley, S. P. Goldberg, and W. D. Jordan, *Heat shock proteins: A review of the molecular chaperones,* Journal of Vascular Surgery **29**, 748 (1999).

[6] S. Cusack, H. Belrhali, A. Bram, M. Burghammer, A. Perrakis, and C. Riekel, *Small is beautiful: Protein micro-crystallography, Nature Structural Biology,* **5**, 634 (1998).

[7] E. Abola, P. Kuhn, T. Earnest, and R. C. Stevens, *Automation of X-ray crystallography, Nature Structural Biology,* **7**, 973 (2000).

[8] R. Fernandez-Leiro and S. H. Scheres, *Unravelling biological macromolecules with cryo-electron microscopy, Nature,* **537**, 339 (2016).

[9] Y. Cheng, *Single-particle cryo-EM-How did it get here and where will it go,* (2018).

[10] S. Jonic and C. Vénien-Bryan, *Protein structure determination by electron cryo-microscopy,* (2009).

[11] T. Ha, A. G. Kozlov, and T. M. Lohman, *Single-Molecule Views of Protein Movement on Single-Stranded DNA,* Annual Review of Biophysics **41**, 295 (2012).

[12] C. Joo, H. Balci, Y. Ishitsuka, C. Buranachai, and T. Ha, *Advances in Single-Molecule Fluorescence Methods for Molecular Biology,* Annual Review of Biochemistry **77**, 51 (2008).

[13] W. E. Moerner, *A dozen years of single-molecule spectroscopy in physics, chemistry, and biophysics, Journal of Physical Chemistry B,* **106**, 910 (2002).

[14] C. Bustamante, C. Bustamante, L. Alexander, K. MacIuba, and C. M. Kaiser, *Single-Molecule Studies of Protein Folding with Optical Tweezers, Annual Review of Biochemistry,* **89**, 443 (2020).

[15] A. N. KC Neuman, *Single-molecule force spectroscopy: optical tweezers, magnetic tweezers and atomic force microscopy,* Nature Methods **5**, 491 (2008).

[16] O. M. Maragò, P. H. Jones, P. G. Gucciardi, G. Volpe, and A. C. Ferrari, *Optical trapping and manipulation of nanostructures,* (2013).

[17] Y. F. Chen, X. Serey, R. Sarkar, P. Chen, and D. Erickson, *Controlled photonic manipulation of proteins and other nanomaterials,* Nano Letters **12**, 1633 (2012).

7

[18] E. C. Yusko, B. R. Bruhn, O. M. Eggenberger, J. Houghtaling, R. C. Rollings, N. C. Walsh, S. Nandivada, M. Pindrus, A. R. Hall, D. Sept, J. Li, D. S. Kalonia, and M. Mayer, *Real-time shape approximation and fingerprinting of single proteins using a nanopore,* Nature Nanotechnology **12**, 360 (2017).

[19] L. Movileanu, *Interrogating single proteins through nanopores: challenges and opportunities,* (2009).

[20] E. C. Yusko, J. M. Johnson, S. Majd, P. Prangkio, R. C. Rollings, J. Li, J. Yang, and M. Mayer, *Controlling protein translocation through nanopores with bio-inspired fluid walls,* Nature Nanotechnology **6**, 253 (2011).

[21] K. Willems, D. Ruić, A. Biesemans, N. S. Galenkamp, P. Van Dorpe, and G. Maglia, *Engineering and Modeling the Electrophoretic Trapping of a Single Protein Inside a Nanopore,* ACS Nano **13**, 9980 (2019).

[22] C. Plesa, S. W. Kowalczyk, R. Zinsmeester, A. Y. Grosberg, Y. Rabin, and C. Dekker, *Fast translocation of proteins through solid state nanopores,* Nano Letters **13**, 658 (2013).

[23] A. E. Cohen and W. E. Moerner, *Suppressing Brownian motion of individual biomolecules in solution,* Proceedings of the National Academy of Sciences of the United States of America **103**, 4362 (2006).

[24] A. E. Cohen and W. E. Moemer, *Method for trapping and manipulating nanoscale objects in solution,* Applied Physics Letters **86**, 1 (2005).

[25] A. P. Fields and A. E. Cohen, *Electrokinetic trapping at the one nanometer limit,* Proceedings of the National Academy of Sciences of the United States of America **108**, 8937 (2011).

[26] J. R. Mejía-Salazar and O. N. Oliveira, *Plasmonic Biosensing,* (2018).

[27] S. A. Maier, *Plasmonics: fundamentals and applications* (Springer Science & Business Media, 2007).

[28] R. Gordon, D. Sinton, K. L. Kavanagh, and A. G. Brolo, *A new generation of sensors based on extraordinary optical transmission,* Accounts of Chemical Research **41**, 1049 (2008).

[29] D. Garoli, H. Yamazaki, N. MacCaferri, and M. Wanunu, *Plasmonic Nanopores for Single-Molecule Detection and Manipulation: Toward Sequencing Applications,* (2019).

[30] A. B. Dahlin, *Sensing applications based on plasmonic nanopores: The hole story,* (2015).

[31] B. J. Roxworthy, K. D. Ko, A. Kumar, K. H. Fung, E. K. Chow, G. L. Liu, N. X. Fang, and K. C. Toussaint, *Application of plasmonic bowtie nanoantenna arrays for optical trapping, stacking, and sorting,* Nano Letters **12**, 796 (2012).

7

[32] R. Gordon, D. Sinton, K. L. Kavanagh, and A. G. Brolo, *A new generation of sensors based on extraordinary optical transmission,* Accounts of Chemical Research **41**, 1049 (2008).

[33] A. Kotnala and R. Gordon, *Quantification of high-efficiency trapping of nanoparticles in a double nanohole optical tweezer,* Nano Letters **14**, 853 (2014).

[34] Y. Pang and R. Gordon, *Optical trapping of 12 nm dielectric spheres using double-nanoholes in a gold film,* Nano Letters **11**, 3763 (2011).

[35] A. Zehtabi-Oskuie, H. Jiang, B. R. Cyr, D. W. Rennehan, A. A. Al-Balushi, and R. Gordon, *Double nanohole optical trapping: Dynamics and protein-antibody co-trapping,* Lab on a Chip **13**, 2563 (2013).

[36] D. V. Verschueren, S. Pud, X. Shi, L. De Angelis, L. Kuipers, and C. Dekker, *Label-Free Optical Detection of DNA Translocations through Plasmonic Nanopores,* ACS Nano **13**, 61 (2019).

[37] D. Verschueren, X. Shi, and C. Dekker, *Nano-Optical Tweezing of Single Proteins in Plasmonic Nanopores,* Small Methods **3**, 1800465 (2019).

[38] X. Shi, D. V. Verschueren, and C. Dekker, *Active Delivery of Single DNA Molecules into a Plasmonic Nanopore for Label-Free Optical Sensing,* Nano Letters **18**, 8003 (2018).

[39] L. A. Giannuzzi *et al.*, *Introduction to focused ion beams: instrumentation, theory, techniques and practice* (Springer Science & Business Media, 2004).

[40] J. Henzie, J. Lee, M. H. Lee, W. Hasan, and T. W. Odom, *Nanofabrication of Plasmonic Structures,* Annual Review of Physical Chemistry **60**, 147 (2009).

[41] X. Chen, N. C. Lindquist, D. J. Klemme, P. Nagpal, D. J. Norris, and S. H. Oh, *Split-Wedge Antennas with Sub-5 nm Gaps for Plasmonic Nanofocusing,* Nano Letters **16**, 7849 (2016).

[42] D. M. Sullivan, *Electromagnetic simulation using the FDTD method* (John Wiley & Sons, 2013).

[43] S. E. Jackson, *Hsp90: Structure and Function,* in *Top Curr Chem*, Vol. 328 (Springer, Berlin, Heidelberg, 2012) pp. 155–240.

[44] M. Hessling, K. Richter, and J. Buchner, *Dissection of the ATP-induced conformational cycle of the molecular chaperone Hsp90,* Nature Structural and Molecular Biology **16**, 287 (2009).

[45] M. Mickler, M. Hessling, C. Ratzke, J. Buchner, and T. Hugel, *The large conformational changes of Hsp90 are only weakly coupled to ATP hydrolysis,* Nature Structural and Molecular Biology **16**, 281 (2009).

[46] K. Richter and J. Buchner, *hsp90: Twist and Fold,* (2006).

7

[47] M. Götz, P. Wortmann, S. Schmid, and T. Hugel, *A Multicolor Single-Molecule FRET Approach to Study Protein Dynamics and Interactions Simultaneously,* in *Methods in Enzymology*, Vol. 581 (Academic Press Inc., 2016) pp. 487–516.

[48] S. Schmid, M. Götz, and T. Hugel, *Effects of Inhibitors on Hsp90s Conformational Dynamics, Cochaperone and Client Interactions,* ChemPhysChem **19**, 1716 (2018).

[49] C. Plesa and C. Dekker, *Data analysis methods for solid-state nanopores,* Nanotechnology **26**, 084003 (2015).

7

SUMMARY

We start this thesis by exploring the question whether there is more to be done with solid-state nanopores, given the success of nanopores for DNA sequencing applications. In **Chapter 1** we motivate the importance of single-molecule tools for sensing of biomolecules such as DNA and proteins in order to understand the fundamental biological processes going on within our cells. Many biological processes are mediated by the action of a single enzyme or molecule. The presence of mutations, even a single point mutation, in the sequence of DNA can lead to diseases. Similarly, small misfolds in the peptide chain that forms proteins can lead to severely compromised function of the protein. Nanopores and nanoapertures are a promising single-molecule tool that has shown great potential for sensing such small mutations.

In **Chapter 2**, we cover the basic concepts of sensing in nanopores and nanoapertures that are needed to understand the rest of the thesis. Here, we introduce two methods of sensing with nanoapertures: first, ionic conductance sensing through monitoring of the flow of ions through the nanopore, and second, optical readout methods that monitor the extraordinary transmission of the nanoapertures from a shift in the local refractive index. The use of plasmonics nanoapertures also allows for nanotweezing of objects through tightly focused optical gradients that are generated by plasmons. Plasmonic nanoapertures even have the ability to sense protein shapes and conformations. Key features and examples of these readout methods are highlighted, as well as recent attempts to combine the two sensors in so-called opto-nanopores or zero-mode-waveguide nanopores. This review demonstrate the ever-growing scientific interest in developing further sensing techniques for the study of biomolecules.

A key challenge in the field of solid state nanopore is to reliably fabricate them. In **Chapter 3**, we demonstrate a novel fabrication method using single-shot e-beam lithography and etching. We produce both arrays and single nanopores on free-standing silicon nitride (SiN) membranes as well as on graphene, a membrane with a thickness of a single layer of carbon atoms. By tuning the dose of the electron beam used, circular shaped nanopores down to 15 nm in size could be produced. The method is both scalable and simple, only requiring standard nanofabrication tools. We demonstrate the sensing capabilities of these nanopores with DNA translocation experiments and found them on par with nanopores produced through TEM milling in their signal-to-noise (SNR) characteristics.

With a convenient way to produce nanopores, we turn to sensing applications of nanopores beyond direct DNA sequencing, since solid state nanopores are too large for sensing of DNA on the single-nucleotide level. We harness the newly discovered CRISPR/Cas9 protein that garnered a lot of interest for its programmable gene-editing purposes. Cas9 can be mutated to remove its endonuclease activity (i.e., cleaving activity) while keeping its programmable dsDNA-binding activity intact. In **Chapter 4**, we demonstrate a novel way of leveraging its single-base-pair recognition accuracy for

a direct DNA-typing/fingerprinting approach with solid state nanopores. Remarkably, dCas9 is found to remain stably bound in the high 1M LiCl nanopore salt solution and showed up as clear spikes in the ionic current trace, allowing for clear detection. Mutations introduced in the gRNA lead to drastically lower binding rates even when the mutations are on the 1-2 base pair level. The ease of programmability and the large signature of the dCas9 in solid-state-nanopore signal opens new avenues for nanopore sensing of DNA targets for diagnostics. We envision the use of such nanopore sensing with CRISPR-dCas9 for the fast detection and identification of DNA motifs of medically relevant DNA targets.

Beyond applied research, we demonstrate that nanopores can also be used to answer fundamental questions in biology, e.g. on DNA organization in **Chapter 5**. Nanopores are particularly suited for these studies as they allow for high statistics to be gathered in liquid and at the single-molecule level. At the heart of this work, we ask if the order of the genes matter in determining the macro-organization of DNA. Two plasmids that contain the same genes but differ in their arrangements (HT and HH) were incubated with nucleoid-associated proteins HNS and FIS that bound these genes. They were subsequently introduced in a nanopore in order to sense how much compaction was induced by the proteins as a function of the gene arrangement. Consistent with extensive AFM studies, we observe a significantly increased compaction in the HT arrangement compared to the HH arrangement. Our observations highlight the importance of the arrangement of genes to the chromosome organization in the cell. Overall, these two chapters show the important role solid state nanopores can play beyond DNA-sequencing applications in both applied and fundamental research.

The need for novel single-molecule sensing tools cannot be overstated. In **Chapter 6**, we employ the use of innovative 2D nanoslits and ionic sensing measurements from the nanopore field to probe polymer transport. These 2D nanoslits are fabricated from exfoliated flakes of graphene and hexagonal boron nitride (hBN) that are stacked to form a very thin slit. The ultrasmooth basal plane of the 2D materials form the floor and ceiling of the slit, which allow DNA to smoothly translocate through the slit in a 'frictionless' manner. The small height of these slits (down to the true nm scale) and the associated confinement of the molecule can be precisely controlled to the thickness of even single-atom layers. We observe the sliding of structures in the DNA such as knots and folds in ionic current trace, and we employed Molecular Dynamics simulations in order to better understand their behavior. We observed that the transport of the DNA polymers was dominated by entrance and exit effects and that interactions with the nanoslit were only transient and weak. 2D nanoslits are thus found to be an excellent platform to study polymer physics transport, absent from surface interactions, in a tunable and amenable way.

As introduced earlier, plasmonics nanoapertures are a promising tool to tweeze and interrogate proteins. However, there are challenges in their fabrication as small variations in the geometry produce vastly different optical properties. In **Chapter 7**, we demonstrate a direct fabrication method with focused ion beam (FIB) to produce arrays of up to 64 inverted bowties. These bowties are extremely consistent in their physical geometry and optical properties. We demonstrate label-free optical detection and nano-tweezing of even single proteins with our nanoapertures. The presence of nanoobjects

in the vicinity of the bowtie apertures locally perturbs the refractive index and leads to a change in the transmission of the nanoaperture. We tweeze 20 nm polystyrene bead and a variety of proteins including beta-amylase and Hsp90. We are able to tweeze Hsp90 for up to 120 seconds, paving the way for the observation and study of the comformation states of Hsp90 in a label-free manner. We propose future experiments where we modulate the kinetics of Hsp90 with AMP-PNP.

Overall, we expect that solid state nanoapertures and nanopores will play an increasing role in single-molecule sensing in the coming years. In particular, we foresee their expansion for use in protein-sequencing and sensing applications. Additionally, recent advancements in the understanding and fabrication of plasmonic nanostructures allow for a new optical readout method to probe biomolecules within these tiny nanovolumes with parallel-sensing opportunities. This unshackles the requirements of non-physiological salt buffers that are used in traditional ionic-sensing methods and bring about exciting new opportunities to sense biomolecules in more native physiological conditions. There is still plenty of potential for nanoapertures and nanopores, and we close this thesis paraphrasing Feynman by saying that there is still "plenty of room at the bottom" in single-molecule sensing with nanoapertures and nanopores.

SAMENVATTING

Dit proefschrift start met de vraag of er meer gehaald kan worden uit solid-state nanopores, in het licht van het succes in de toepassing van nanopores voor DNA-sequencen. In **Chapter 1** schets ik het belang van gereedschap dat werkt op het niveau van individuele moleculen, zoals DNA en eiwitten, om zodoende de fundamentele biologische processen van onze cellen te kunnen doorgronden. Vele biologische processen worden gestuurd door middel van de acties van één enzym of molecuul. De aanwezigheid van mutaties in de DNA-sequentie, zelfs wanneer het slechts één enkele puntmutatie betreft, kan leiden tot een ingrijpend ziektebeeld. Ook kan een kleine misvouwing in de peptideketen die eiwitten hun vorm geeft leiden tot een sterk gecomprimeerde eiwit functie. Nanopores en nanoapertures zijn veelbelovende gereedschappen op het niveau van individuele moleculen en hebben een groot potentieel om zulke kleine maar cruciale mutaties te kunnen detecteren.

In **Chapter 2** zet ik de basisconcepten uiteen van detectie met nanopores en nanoapertures, die nodig zijn voor het begrijpen van de hierop volgende hoofdstukken. We introduceren hier twee manieren van detecteren die mogelijk zijn met nanoapertures: ten eerste, detectie via ionische geleiding waarbij de stroom van ionen door de nanopore word gemeten, en ten tweede, optische uitleesmethoden die de uitzonderlijke transmissie van nanoapertures ten gevolge van een verschuiving in de lokale brekingsindex meten. Het gebruik van plasmonische nanoapertures geeft daarnaast de mogelijkheid tot het nanotweezen van objecten door middel van de sterk gefocuste optische gradiënten die gegenereerd worden door de plasmonen. Plasmonische nanoapertures geven zelfs de mogelijkheid om de vorm en conformaties van eiwitten te detecteren. De belangrijkste kenmerken en voorbeelden van deze uitleesmethoden zullen worden besproken, evenals recente pogingen tot het combineren van de twee sensoren in de zogenoemde opto-nanopores of zero-mode-waveguide nanopores. Dit overzicht demonstreert de nog altijd groeiende wetenschappelijke interesse in het ontwikkelen van nieuwe detectiemethoden voor het bestuderen van biomoleculen.

Een cruciale uitdaging met betrekking tot solid-state nanopores is reproduceerbare productie van de nanostructuren. In **Chapter 3** tonen wij de potentie van een nieuwe fabricatiemethode aan waarbij gebruik word gemaakt van single-shot e-beam lithografie en etsen. Hiermee produceren wij zowel geordende arrays als opzichzelfstaande nanopores op een vrijstaand membraan van siliciumnitride (SiN) als ook op grafeen, een membraan gevormd uit één enkele laag koolstof atomen. Door de dosis van de electronenstraal af te stemmen konden cirkelvormige nanopores met een grootte van 15 nm worden geproduceerd. Deze methode is rechtdoorzee en gemakkelijk opschaalbaar omdat er enkel gebruik word gemaakt van standaard nanofabricatieapparatuur. Wij tonen de functionaliteit van deze nanopores aan door middel van DNA-translocatieexperimenten waarbij de resultaten vergelijkbaar bleken met nanopores geproduceerd door TEM-milling wat betreft hun signaal-ruis kenmerken.

Vervolgens richten wij ons op detectieapplicaties voor nanopores die niet te maken hebben met DNA-sequencen aangezien solid-state nanopores te groot zijn voor het detecteren van individuele DNA nucleotiden. In plaats daarvan gebruiken wij het recent ontdekte CRISPR/Cas9 eiwit, wat enorme wetenschappelijke interesse genereerde door zijn programmeerbare gen-bewerkingsmogelijkheden. Cas9 kan namelijk op zo'n manier gemuteerd worden dat het zijn endonuclease activiteit (d.w.z. zijn knip-activiteit) verliest maar zijn programmeerbare dsDNA-bindingsactiviteit behoud. In **Chapter 4** laten wij een nieuwe methode zien die gebruik maakt van de basispaar-accurate herkenning van het eiwit voor een directe DNA-typing/fingerprinting methode met solid-state nanopores. Het is opmerkelijk dat dCas9 stabiel gebonden blijft ondanks hoge concentraties van 1M LiCl nanopore zoutoplossingen en dat het herkenbare pieken in het detectiesignaal laat zien. Mutaties geïntroduceerd in het gRNA leiden tot drastisch lagere bindingstabiliteit, zelfs wanneer de mutaties slechts 1 á 2 basisparen zijn. Het gemak waarmee het eiwit programmeerbaar is en het duidelijke karakteristieke signaal van dCas9 in solid-state nanopores, opent een scala aan nieuwe mogelijkheden voor het detecteren van DNA targets voor diagnostische doeleinden. Wij voorzien gebruik van deze nanopore detectiemethode met CRISPR-dCas9 voor snelle detectie en identificatie van DNA-motieven in medisch relevante DNA targets.

Naast toegepast onderzoek voor praktische doeleinden, tonen wij in **Chapter 5** aan dat nanopores ook gebruikt kunnen worden voor het beantwoorden van fundamentele vragen in de biologie, bijvoorbeeld de organisatie van DNA. Nanopores zijn uitermate geschikt voor deze studies omdat zij het verzamelen van grote hoeveelheden statistische gegevens toestaan op het niveau van individuele moleculen in vloeistof. De kern van deze studie draait om de fundamentele vraag of de rangschikking van genen belangrijk is voor de macro-organisatie van DNA. Twee plasmiden met dezelfde genen, maar in verschillende onderlinge rangschikking (HT en HH), werden geïncubeerd met de nucleiod-geassocieerde eiwitten HNS en FIS die aan deze genen binden. Vervolgens werden ze gedetecteerd met een nanopore om te zien in welke mate verdichting werd geïntroduceerd door de verschillen in de rangschikking van hun genen. In overeenstemming met uitgebreide AFM studies, zagen wij een significant sterkere verdichting bij de HT-rangschikking in vergelijking met de HH-rangschikking. Onze observaties onderstrepen het belang van de rangschikking van genen voor de chromosomale organisatie in de cel. Samen genomen tonen deze twee hoofdstukken het belang aan van de rol die solid-state nanopores in zowel praktisch als fundamenteel onderzoek.

De behoefte aan nieuwe detectiemethoden op het niveau van individuele moleculen kan niet genoeg worden benadrukt. In **Chapter 6**, gebruiken wij innovatieve 2D-nanoslits om polymeer transport te onderzoeken. Deze 2D-nanoslits zijn geproduceerd uit geëxfolieerde grafeenschilfers of hexagonaal boornitride (hBN) welke op elkaar zijn gelegd en zodoende een zeer dunne spleetvormige opening vormen. Het extreem gladde vlak van het 2D-materiaal vormt de bodem en plafond van de spleet, waardoor DNA zich soepel door de spleet kan verplaatsen zonder dat wrijving plaats vindt. De geringe hoogte van de nanoslits (in het nm bereik) en de hiermee geassocieerde bewegingsbegrenzing van het molecuul kan heel precies worden beheerst tot op een dikte van zelfs één enkele laag atomen. In het ionenstroomsignaal nemen we de beweging waar van structuren in het DNA, zoals knopen en vouwen, en we gebruiken Molecular Dynamics

simulaties om dit gedrag beter te begrijpen. Transport van het DNA-polymeer bleek gedomineerd te worden door ingangs- en uitgangseffecten terwijl de interacties met de nanoslit louter kortstondig en zwak waren. Hiermee zijn 2D-nanoslits een uitstekend platform voor het bestuderen van de fysische eigenschappen van polymeertransport, zonder oppervlakinteracties

Hoewel plasmonische nanoapertures een veelbelovende methode zijn voor het heel precies vastgrijpen en bestuderen van eiwitten, zijn er uitdagingen in hun fabricatie omdat kleine variaties in de geometrie leiden tot grote verschillen in hun optische eigenschappen. In **Chapter 7** demonstreren wij een directe fabricatiemethode die gebruik maakt van een Focussed Ion Beam (FIB) voor het produceren van arrays van 64 nanoapertures in de vorm van omgekeerde vlinderdassen. Deze nanoapertures zijn hoogst consistent in hun fysische geometrie en hun optische eigenschappen. We tonen aan dat optische detectie mogelijk is zonder gebruik te maken van labelling, en dat wij individuele eiwitten weten vast te grijpen met onze nanoapertures. De aanwezigheid van nanoobjecten in de omgeving van de nanoapertures veroorzaakt een lokale verandering in de refractieindex wat een verandering veroorzaakt in de transmissie door de nanoapertures. We hebben 20 nm polystyreen deeltjes weten vast te grijpen, als ook een verscheidenheid aan individuele eiwitten zoals betaamylase en Hsp90. We konden Hsp90 voor 120 seconden vasthouden, waarmee we de weg vrij maken voor het observeren en bestuderen van de eiwit conformaties van Hsp90 op een manier die geen labellingsmethode gebruikt.

Samengevat verwachten wij dat solid-state nanoapertures en nanopores in de komende jaren een belangrijke rol zullen gaan spelen in detectie op het niveau van individuele moleculen. Meer specifiek voorzien wij een uitbreiding van hun gebruik bij het sequencen en detecteren van eiwitten. Recente ontwikkelingen in onze kennis en fabricatie van plasmonische nanostructuren maken een nieuwe optische detectiemethode mogelijk voor het onderzoeken van biomoleculen in deze extreem kleine nanovolumes. Dit verlost ons van de voorheen vereiste niet-fysiologische zoutbuffers die gebruikt worden in traditionele ionenstroom detectiemethoden en het is daarmee een voorbode voor spannende nieuwe mogelijkheden voor het detecteren van biomoleculen in natuurlijke fysiologische condities. Er is enorm veel potentie voor het gebruik van deze nanoapertures en nanopores, en we besluiten dit proefschrift daarom door Feynman te parafraseren met de notie dat er nog altijd "plenty of room at the bottom" is voor detectie van individuele moleculen met nanoapertures en nanopores.

ACKNOWLEDGEMENTS

The PhD has been an amazing adventure, far more vibrant and dynamic than I ever imagined at the start of it some 4-5 years ago. The work condensed in this thesis is a culmination of a lot of excellent scientific crossovers. I count myself lucky to have been able to experience firsthand many excellent scientists both in Delft and outside. I am glad to count many of you as friends.

First and foremost, I would like to thank my supervisor and promotor, **Cees Dekker** for his guidance and supervision throughout this journey. You have assembled a great group of driven, talented young scientists and built up a vibrant and dynamic environment for me to play in. The scientific resource, lab trips and cohesion activities allowed many ideas and conversations to be planted. A testament to that is the wide breadth of the projects covered in this thesis - made only possible by the diverse team of experts and techniques you have assembled 'under one roof'. Over the last 5 years, I took down many notes and reflections on the lessons learnt through your direct guidance. I will just list one key lesson that I learnt from you. You have always challenged me to ask 'why are we doing this?'. I used to think that good scientists just ask a lot of questions but now through this, I learnt that they also ask the RIGHT questions. The push to justify every secret project, though frustrating during the time, led me to be a more mature, focused scientist. In a more informal setting, you were very sporting to take a good joke/jab in one of the 'Ask Cees anything' sessions that we did in the lab retreat. (Also, thanks for not firing me despite my countless "office hours" at the coffee corner).

I would like to thank my exam committee : **Prof. Aleksandra Radenovic**, **Dr. Slaven Garaj**, **Prof. Boya, Radha**, **Prof. Peter Steeneken**, **Dr. Chirlmin Joo** and **Dr. Sabina Caneva** for taking out the time from your busy schedule to examine my thesis - I hope the reading of the thesis was enjoyable!

Below, I start by acknowledging the people in the various projects listed in the thesis. On the chapter on Lithography Fabrication of Nanopores - **@DanielV**: It was a a great pleasure to be shown the ropes in the CD lab by you. You set a lot of the tone, enthusiasm and attitude to science that I tried to emulate in the lab. It is only fitting that my first tangible scientific output in the lab be listed with you.

On the chapter on the Nanopore detection of CRISPR/dCas9 - the affectionately known **Team Cas9 @Laura, Michel, Stephanie, Anthony and Jaco**. This was my first time coordinating such a big team. Seeing everyone running around folding Cas9, running gels and nanopore experiments one late evening when everyone else has gone home is one of the highlights of my PhD. I am extremely proud of the way we came together and delivered a beautiful paper.

On the chapter of using nanopores to detect DNA sequence cooperativity of proteins in nanopores - **@Sandro**. I have always great admired your abilities as a scientist, so imagine the joy when I got the opportunity to see the skills firsthand with a project with you. Call me if you ever need to put other things through a nanopore!

On the chapter on DNA translocations through nanoslit: Working and coordinating an international team of scientist spread across 3 different countries has been very challenging and fun. I could always get a prompt response to the whatsapp messages and emails that I sent out at ungodly times. **@Adnan and Aleksei**, thanks for the beautiful simulations and accommodating the many particular request on how thick DNA should be rendered with. The story would not have been complete without you. **@Radha and Ashok** and the rest of the team at Manchester, thanks for putting the painstaking work of fabricating the devices, constant discussions and edits. I have a fond memory of us crouching on the floor of the massive convention hall in Boston trying to lay out the figure plans. How many PIs can say they have done the 'ground' work :P? I am very excited about your respective groups and will continue to follow your research.

It is no secret that the masters and undergraduate students are behind many of the long hours and did a lot of the heavy lifting. Through these years, I have had the fortune to mentor a handful of talented young scientist in the making. Their energy and enthusiasm reminded me why I enjoyed doing science in the first place and it has been a blast learning with them. Thanks **@Thomas** who bravely trusted me with supervising his BEP only 2 months into my PhD. **@Jing Kun** - we made a lot of holes and broke a lot of membranes but luckily that was exactly what the grant wanted us to do. **@Quentin** for kickstarting the double nanopore project and not giving up even after mounting a ridiculous amounts of pipettes. In the protein trapping project, I have had 2 very talented students: **@Christian** who taught me a lot about math and rigour, also proving that one can be BOTH a good theorist and experimentalist. **@Madeleine** who reminded me that good scientists are not bound by traditional disciplines. As long as one has the interest and drive, one can explore different areas and quickly catch up. You will go far no matter which field you pursue. Also thanks for the Dutch translation of my summary!

A lot of the scientific work also drew on the larger support staff both in BN and the entire Kavli Delft family. At the TEM imaging facility, I would like to thank **@Wiel Evers** for never losing patience whenever the TEM went down and always springing to prompt action to fix it. Also in the department **@Sacha Khaiboulov** for his alliance in fighting the building's ventilation system. Also **@Jan** for ensuring that I did not get locked out of the lab and **@Anke** for the larger support in keeping the lab well stocked. I would also like to thank the members of the Kavli-Nanolab (aka Cleanroom), especially **@Hozanna Miro** and **@Dustin Laur** who supported me greatly on the FIB. I would like to also thank the administrative staff in BN - especially **@Amanda** and **@Marije Boonstra** for making paperwork less painful.

Turning to the lab, I would like to thank the Scientific Influencers - **Ash, Allard, Eli, Jaco and Jacob**. I mentioned once during the lab trip that you guys are the backbone of the lab and a vein of continuity that surpasses the lifetime of PhDs and Postdocs. The term "technicians" do no justice and instead I coin the term "Scientific Influencers" for you guys. The wisdom shared on both on practical science and life influences our trajectories and I will recall many of them in the time beyond. **@Ash** - Thanks for all the skittles and chocolates - they kept me fuelled through this thesis. You add a very cheerful vibe to the group. **@Allard**, I learnt a lot of interesting facts and perspective on many fields over the lunch conversations. Also thanks for the beautiful keyboard that I hammered this thesis on. **@Eli** - For the mature conversations and dinner at your place after the

started the journey in Delft together and through the years, for the many random advices you shouted/threw at me in random moments.**@Anthony** - the first memory I have of us is having a convo for 45 mins before realising we are in the same lab. And my amazement at meeting another Hannibal fan. I hope there is still time to have you over for dinner. **@Eugene** - or Dr Kim, you will have a blast as a PI and I envy your incoming lab members who will learn so much from you! **@Bis** - we have climbed many boulders and walked many steps. I have always appreciated your warm approach to asking questions- where you seek answers without the pressure of judgement. Thanks for all the shared wisdom, I am sure our conversations will not end here! **@Sandro** - I have enjoyed all our conversations on science and beyond. You always have helpful advice on both the practical and non-work stuff. Also it has been quite a Christmas tradition to go for a dinner at your place and have conversations on the most wild stuff. Shout out to **@Nutsa**! **@Alberto** - always up for a good meme or joke. On countless occasions I have stopped in the middle of what I was doing and burst out laughing at your text. Also, for the tons of snacks and chats by your table whenever I am procrastinating. You have brought me much joy. Life has countless ways of frustrating us but you reminded me to laugh once in a while. May you stay cheerful and press on as you round up the PhD!

The next Gen - you guys are like the shiny new iphone that make us old folks look like bricks. The lab is very strong. **@Martin**, don't forget the quotes though I think your inner drive is more inspiring. **@ Roman**, top notch self-depreciating humour. Keep the same attitude and you will make it through the PhD. **@Sabrina**, I have not met such a dedicated scientist in the face of relentless experimental difficulties. You took the office humour like a champ. Take ownership and try and enjoy the process. (or I hope Stockholm syndrome kicks in soon for you!) Shoutout to **@Julian**! **@Tisma**, thanks for all the cashews, dinners and convos. It is extremely humbling to learn so much from someone so young. Hopefully, someday we will collaborate. I need no organisation or certification to convince me, you are already 3 sigma in my eyes.

Outside the lab, there are a few more people that I would like to thank that have broaden my life experience here in Delft. First, shoutout to friends who might be thousands of kms away but random texts and meet ups whenever I am in town bring you guys close to my heart- **@Changyang @Ziwei @Kenneth @DanielFoo**.

The Singapore Aunties Gang at the Hague - **@Grace, @LeQin, @Agnes, @Doreen, @Angie, @Mickey** and **@Evelyn** - Thank you guys for making a home away from home. It was nice to slip back into Singlish over some amazingly good food at @Grace's place. The govt spends millions a year trying to connect us but maybe they should talk to **Grace**. **@Le Qin**, my fellow Singaporean PhD student to rant to about PhD life. I have enjoyed all the hunt for food, conversations, cute cat pics when science isn't quite going our way. You are one of the most wholesome person I know. Jiayou for the rest of your PhD!

@SingaFun- Wow, what a blast, we took Singapore and Malaysia by storm. **@Sabina** - thanks for all the walks, talks and bouncing GENIUS ideas. I am sure our paths will cross again. Keep dancing like you are 22 in the Caneva lab! **@Sara** For all the baked goodies and packed food! You will run an amazing chain of cafes and shops one day. Martin is a really lucky man. **@Martin**, We have come a long way from Canada and McGill. I am sure our collaboration and friendship will not end here. Your texts, reassurance and commitment to science has inspired me on countless occasion. The things I am grateful

for are too long to list here so how about we do it over some gin, whisky and hearty meal?

The Great Danes, **@Oskar and @Gro** - for opening up your homes to countless dinners and g&t sessions. **@Oskar**, for starting the casual terrors and being always up for anything from shooting virtually to clay pigeons! You are seriously the most good natured guy I know. Team ÆRødgrødMæFlød'Å will live on (that was quite painful to LaTex...)! **@Gro** for patiently tolerating all the noise during band practices and the amazing baked goodies in an attempt to make us stop playing early. I look forward to visiting and meeting the newest addition to the family! My time in Delft may end but I am sure I will see you guys beyond!

To the Bengtson family **@Michel and Madi**. **@Madi**, you might be too young to remember this but I hope you know that you have brought great joy to all the PhD uncles and Aunties in Delft. We might have doctorates and respectable impact factors but we are still drawing horses and rainbows on your command or racing through playgrounds with you. I will always remain "Uncle Wayne". It is my great pleasure to have watched you grow and see the sacrifices and love that your mom has dedicated to you. You are truly blessed. **@Michel**, wow look at how far we have come since that fateful day when I got off my bike to walk with you. The memories and adventures are too numerous to name so let's save it for a steak or a sad sausage day. We made it! As promised, to the end and beyond.

Massa McGill - **@Siva, @Constance, @MingHwei** and company. My PhD has been punctuated with these hiking/eating adventures. It's nice to see that we are still flying half way across the world, literally climbing mountains and eating our way to new experiences. 4 time zones to coordinate plans for skype is no easy feat. **@MingHwei** for checking up on me and making sure that I don't end up in therapy. **@Siva**, bro, the adventures we shared after McGill have brought me immense joy, whether we are doing an overnight hike up Kinabalu or trying to figure out our duties in a wedding. I can always count on your support and to keep me focused on the right objectives/priorities in life. To even greater heights! **@Constance**, I have so much to be grateful for, where do I even start? Here is just one thing - Thanks for all the texts I go to bed and wake up to. You have been my constant all these years.

Parents and Family - To my dear parents, **Mummy** and **Papa**, when I reflect on my PhD, I reflect on the costs not just borne by me but you guys. All parents worry about their children but even more so when they are far away. I don't know how you guys keep track of the 4 of us - we are literally scattered across the world, up to 4 different continents at one point! You two have never explicitly determined a path for us but just quietly supported whatever that we choose to pursue. It is only with this patient support that I am on this path. To my dear siblings **@Ryan @Ian and @ Joan** - its been a while since we lived under the same roof so the times that we have done so has been messy/chaotic but very fun. 6 people drunk in an overnight carriage travelling through Germany or frantically looking for our missing parents who wandered off looking for Chinese food before a train departure. These are just some of the many stories I keep in my heart. We don't always agree and often clash like all siblings do. However, know that I am extremely proud of you guys. You will always have my support. To my dear parents, I dedicate my achievements to you!

CURRICULUM VITÆ

Wayne Wen Wei YANG

12-05-1990   Born in Singapore

TIMELINE

2003–2006   Secondary School
                   Victoria School, Singapore

2006-2007   High School
                   Columbia International College, Ontario, Canada

2007–2009   National Service
                   Singapore Armed Forces

2009–2013   B.Sc (Major: Physics, Minor: Psychology)
                   McGill University, Montreal, Canada
                   Dean Multidisciplinary Research List (Physics and Psychology)
                   Thesis: Graphene devices for electronics and C12-C13 graphene isotopes
                   Thesis: Facebook and positive social feedback

2013–2015   M.Sc (Physics)
                   Department of Physics, McGill University, Montreal, Canada
                   Thesis: Graphene wet cell for scanning electron microscopy imaging
                   Advisor: Prof Michael Hilke and Prof Walter Reisner

2016–2020   Ph.D. Bionanoscience
                   Technische Universiteit Delft, Delft, The Netherlands
                   Thesis: Single-molecule sensing with nanopores and nanoslits
                   Promoter: Prof. dr. C. Dekker

LIST OF PUBLICATIONS

10. **W. Yang**, B.Radha, A. Choudhary, G. Mettela, A.K. Geim, A. Aksimentiev, A. Keerthi, C. Dekker. *Translocation of DNA through ultrathin 2D-nanoslits*, (In print, Advanced Materials).

9. A. Japaridze, **W. Yang**, C. Dekker, W. Nasser, G. Muskhelishvili. *DNA sequence-directed cooperation between nucleoid-associated proteins*, (Under review, iScience).

8. **W. Yang**, C. Dekker. *Single-molecule ionic and optical sensing with nanoapertures*, (Submitted as book chapter for Single Molecule Nanosensors and Nanosystems, Springer Nature).

7. Y. Zhang, Y. Miyahara, N. Derriche, **W. Yang**, K. Yazda, X. Capaldi, Z. Liu, P. Grutter, W. Reisner. *Nanopore Formation via Tip-Controlled Local Breakdown Using an Atomic Force Microscope*, Small Methods, 1900147 (2019).

6. **W. Yang**, L. Restrepo-Pérez, M. Bengtson, S.J. Heerema, A. Birnie, J. van der Torre, C. Dekker. *Detection of CRISPR-dCas9 on DNA with solid-state nanopores*, Nano letters, 18(10) 6469-6474 (2018).

5. P. Cadinu, G. Campolo, S. Pud, **W. Yang**, J.B. Edel, C. Dekker, A.P. Ivanov. *Double barrel nanopores as a new tool for controlling single-molecule transport*, Nano letters, 18(4) 2738-2745 (2018).

4. D.V. Verschueren[†], **W. Yang**[†], C. Dekker, *Lithography-based fabrication of nanopore arrays in freestanding SiN and graphene membranes*, Nanotechnology, 29(14) 145302 (2018).

3. E. Whiteway, **W. Yang**, V. Yu, M. Hilke. *Time Evolution of the Growth of Single Graphene Crystals and High Resolution Isotope Labeling*, Carbon, 111, 173-181 (2017).

2. **W. Yang**[†], Y. Zhang[†], M. Hilke, W. Reisner *Dynamic imaging of Au-nanoparticles via Scanning Electron Microscopy in a Graphene Wet Cell*, Nanotechnology, 26, 315703 (2016).

1. H. Razavipour, H.A. Hafez, I. Al-Naib, **W. Yang**, P. Lévesque, A. Guermoune, F. Blanchard, X. Chai, D. Feracho, R. Martel, M. Hilke, M.M. Dignam, T. Ozaki, D.G. Cooke. *High field response of gated graphene at THz frequencies*, Physical Review B, 92, 24, 245421(2015).

† These authors contributed equally.